

THE USE OF NANOPARTICLES TO ASSESS
SUBSURFACE FLOW HETEROGENEITY

A Dissertation

Presented to the Faculty of the Graduate School
of Cornell University

In Partial Fulfillment of the Requirements for the Degree of
Doctor of Philosophy

by

Yushi Zhao

Jan 2015

© 2014 Yushi Zhao

THE USE OF NANOPARTICLES TO ASSESS SUBSURFACE FLOW HETEROGENEITY

Yushi Zhao, Ph. D.

Cornell University 2015

Abstract

Understanding subsurface flow condition is difficult, but very important. Tracer tests have been done as a diagnostic tool to assess the subsurface fluid flow conditions. However conventional ionic tracers are very diffusive, thus during a prolonged field test, the resolution of the breakthrough curve are usually tempered by their rapid rate of diffusion. Inert nanoparticle tracers are much larger than ionic tracers, and not very diffusive. Laboratory scaled dual nanoparticle and chemical tracer experiments in both aqueous and CO₂ based systems are demonstrated in this dissertation, as well as a field test in a “single crack” sub-horizontal bedrock fracture system. These tests demonstrated the CDot nanoparticles behave inertly both in the laboratory and in the natural groundwater conditions. Differential arrival patterns between inert nanoparticle tracers and ionic tracers suggest that the particle tracers give higher resolution breakthroughs. Moreover, in the field test, channelized flow is hinted by the erratic arrival of inert particle tracer, which is further confirmed by the largely retarded arrival of surface area dependent sorbing ionic trace injected simultaneously.

BIOGRAPHICAL SKETCH

Yushi Zhao was born in Guizhou China and lived in many cities in China before coming to the United States for university studies. He graduated from Goshen College Indiana in 2005 with a Bachelor's degree in Computer Science with a triple minor in Mathematics, Business Information Systems, and Multimedia Communication. After working for five years in industry and entrepreneurship, he came to Cornell in the fall of 2010 to pursue a Master degree in Geological Sciences, performing experiments on the gaseous inter-diffusion of methane and carbon dioxide. At the end of his master's program, an opportunity arose to research the feasibility of using nanoparticles to assess the viability of sequestering carbon dioxide in shale, which proved to be only the first third of his thesis research. An internship with Chevron Energy Technology Company, in Houston Texas led to his decision to join Chevron and take up the global energy challenge of powering the world.

Dedicated to my mom and dad.

ACKNOWLEDGMENTS

I am very grateful to many people and organizations for support and assistance during my time at Cornell. First of all I would like to thank the chair of both my M.S. and Ph.D. advisory committees, Dr. Lawrence Cathles. Secondly I would like to thank my minor master's committee advisor Dr. James Engstrom, and my minor Ph.D. committee members Dr. Louis Derry and Dr. Tammo Steenhuis. Third I would like to thank all, the professors from whom I gained insight at Cornell, namely Dr. Terry Jordan, Rick Allmendinger, Larry Brown, Sue Kay, Bill White, Jeff Tester, Dave Hysell, Rowena Lohman, Lynden Archer, Aksel Hiorth (Norway), Norman Scott, Andrew Hunter, and Al Center. I would also like to say thanks to the people who helped me during my time at Cornell, namely, Savannah Williams, Amy Colvin, Teri Carey, Hilary Cullen, Polly Marion, Celia Szczepura, Brenda Fisher, Lorie Walker, Dave Jung, Caryl Mansing, Steve Gallow, Judy Starr, Shivaun Archer, Gregg McElwee, Stephan Kramer, Norma Ortega, Dominic Fontana, and to those I forgot to mention.

In addition, I would like to thank my funding sources, organizations, and research facilities for the support provided on my doctoral project. In no particular order: The National Science Foundation Graduate Research Fellowship Grant No. (0966045), award KUS-C1-018-02, made by King Abdullah University of Science and Technology (KAUST), DOE Project No. DE-FE0004633 managed by Advanced Resources International, Inc (ARI), Cornell University Center for Energy and Sustainability, Cornell Energy Institute, USEPA, NYSDEC, NYSERDA,

Cornell CNF, Cornell Machine Shop, Cornell Department of Biomedical Engineering, and the William H. Miner Agricultural Research Institute.

TABLE OF CONTENTS

TABLE OF CONTENTS	viii
LIST OF FIGURES	xiii
LIST OF TABLES	xvii
CHAPTER ONE: GENERAL INTRODUCTION	1
References	6
CHAPTER TWO: USING CO₂-PHILIC NANOPARTICLES TO ASSESS CARBON SEQUESTRATION IN SHALE	9
Abstract	9
Introduction	11
Laboratory Experiments and Their Application	14
Conceptual Description of the Dual Tracer Method	14
Experiments Demonstrating Dual Tracer Methods for Supercritical CO ₂	21
Particle requirements and synthesis	21
Experimental chemistry	23
Experimental design	24
Construction of apparatus	28
Experimental procedures	29
Experimental results and interpretation	31
Translation to the Field	37
Discussion, Summary and Conclusions	41
Discussion	41
Summary and Conclusions	44

Acknowledgements	46
Supplementary Materials	48
Apparatus Fabrication	48
Calibration Curves and Concentration Measurement	52
Diffusion Coefficients	56
Chemical Tracer – Trifluorotoluene (TFT)	59
Nanoparticle Tracers	61
Estimation of Interdiffusion Coefficient of scCO ₂ and Methane	66
References	70

**CHAPTER THREE: NANOPARTICLE METHODS FOR MEASURING
REMEDIATION OF FLOW HETEROGENEITY IN LABORATORY**

COLUMNS	79
Abstract	79
Introduction	80
Material and Methods	86
Column Packing and Design	86
Solid Materials and Methods	91
Tracer Materials and Methods	93
Experimental Results	94
Permeability Ratio Experiments	96
Core Radius Experiments	99
Optimal Column Design	103
Optimizing Flow Rate	106

Evaluating Flow Remediation	110
Conclusion	113
Acknowledgements	114
Supplementary Material	115
Testing measurement interference for combined KBr and CDot tracers	115
Measuring CDot Retention	117
Predicting Diffusion from the Core into the Annulus	117
Simple Piston Flow Model	120
References	122
CHAPTER FOUR: QUANTITATIVE EVALUATION ON ENHANCED SWEEPING OF MICRO-SIZED POLYACRYLAMIDE ELASTIC MICROSFERES (MPEMS) IN HETEROGENEOUS POROUS MEDIA USING DUAL-TRACER METHOD 128	
Abstract	128
Introduction	129
Material and Methods	131
Dual-Permeability Column Model	131
Materials and Reagents	133
Apparatus and Process	136
Methods and Procedures	138
Results and Discussion	142
Breakthrough Curves of KBr and CDot Before and After Injection of MPEMs	142

Enhanced Sweeping of MPEMs in Heterogeneous Porous Media	147
Effect of permeability ratio (k_c/k_a) on ΔE_v	149
Effect of core pore volume proportion (V_c/V_t) on ΔE_v	151
Summary and Conclusion	153
Acknowledgement	153
References	154
CHAPTER FIVE: AIR-FREE PACKING OF SATURATED LABORATORY SAND COLUMNS	
Abstract	158
Introduction	159
Air in the Column	161
The Air-Free Packing Protocol	164
The Column Design and Construction	164
Homogeneous Column Packing	166
Heterogeneous Column Packing	170
Results and Discussions	170
Conclusions	174
Acknowledgements	174
References	175
CHAPTER SIX: ASSESSING FLOW HETEROGENEITY IN A SINGLE NATURAL FRACTURE USING AN INERT NANOPARTICLE TRACER	
Abstract	178
Introduction	179

Materials and Methods	183
Results and Discussions	186
Conclusion	207
Acknowledgements	207
Supplementary Materials	208
Photobleaching	208
Tracer Modeling	214
References	216

LIST OF FIGURES

2.1	Illustration of dual tracer flow behavior in shales.	16
2.2	Illustration of sequestration for inert substances injected into a fracture which diffuse to different degrees into the adjacent matrix.	18
2.3	Schematic of glass Hele-Shaw experiment apparatus.	25
2.4	Schematic and image of experimental setup.	30
2.5	Effluent concentration as a function of time for experiments carried out in HFE.	34
2.6	Streamline between two wells.	39
2.7	Illustration of possible test in a depleted gas shale.	42
2.S1	Image of finished product of apparatus 1 and 2 from SGP.	49
2.S2	Image of PDMS treatment procedures.	50
2.S3	Calibration curves for the tracers used.	55
2.S4	Illustration of trifluorotoluene molecule.	59
2.S5	Size distribution of SiO ₂ nanoparticles.	61
2.S6	Size distribution of Fe ₃ O ₄ nanoparticles.	63
2.S7	Carbon dioxide phase diagram.	67
3.1	Illustration of dual tracer flow behavior in a heterogeneous column.	82
3.2	Graphical illustration of how the pattern of tracer arrival will change as the permeability of the core is reduced relative the annulus.	85
3.3	Graphically illustration of heterogeneous column.	88

3.4	Schematic and picture of experimental apparatus setup during operation.	90
3.5	Illustration of core-annulus permeability ratio column experiments.	97
3.6	Breakthrough curves and fraction plot for permeability ratio column experiments.	98
3.7	Graphical illustration of the flow experiments where core diameter is systematically varied.	101
3.8	Breakthrough curves and fraction plots for core diameter varying column experiments.	102
3.9	Optimization column condition fraction plots.	105
3.10	Tracer breakthrough curves for flow rate optimization column experiments.	107
3.11	Breakthrough curves comparisons based on different flow rates.	109
3.12	Breakthrough curves and fraction plots for MPEMs showcase.	112
3.S1	Tracer stability column test.	116
4.1	Diagram of dual-permeability column model.	132
4.2	Inverse microscope image of MPEMs after swelling in NaCl solution.	135
4.3	Flow diagram for dual-tracer experiments.	137
4.4	Illustration of column 1 – 5.	140
4.5	Breakthrough curves of KBr and CDot before and after injection of MPEMs in heterogeneous column.	143
4.6	Integral fraction curves of KBr and CDot before and after injection of MPEMs in heterogeneous column.	144

4.7	Graphical illustration of heterogeneous column flow.	146
4.8	Breakthrough curves of CDot before and after injection of MPEMs in dual-permeability models varying core-annulus permeability ratio.	150
4.9	Breakthrough curves of CDot before and after injection of MPEMs in dual-permeability models varying core-total pore volume ratio.	152
5.1	Illustration of air trapping mechanisms.	162
5.2	Image of air bubbles in the column.	163
5.3	Diagram of the Plexiglass column components.	165
5.4	Graphical illustration of column vacuum de-gassing.	168
5.5	Diagram of homogeneous and heterogeneous column packing workflow.	169
5.6	CDot breakthrough curves of repeated homogeneous and heterogeneous column test following air-free packing protocol.	172
5.7	CDot breakthrough curves of repeated heterogeneous column test do not follow air-free packing protocol.	173
6.1	Illustrated map of experimental field site.	181
6.2	Combination tracer arrival curve.	187
6.3	Streamline model for injection well pair case 204-104.	196
6.4	Comparison of observed and simulated tracer concentration for 204-104.	197
6.5	Model prediction of all 6 well pairs.	199
6.6	Model fits for well pair 404-304 step test.	203
6.S1	CDot photobleaching profile under direct sunlight and residue plot after single	

exponential fit.

209

6.S2 CDot photobleaching profile under room light and residue plot after single

exponential fit.

212

LIST OF TABLES

2.1	Cell design parameters.	27
2.2	Diffusion constants for the particles and chemical TFT tracer in HFE.	36
2.3	Diffusion constants for particles, TFT, and methane in scCO ₂ .	38
2.S1	Summary of calculated diffusion constants.	57
2.S2	Diffusion constants in scCO ₂ for spherical particles of different diameter.	65
3.1	Parameters for four sand types.	92
3.2	Summary of basic parameters of heterogeneous column models.	95
3.S1	Detailed parameters and calculated N _{iPe} for the flow rate varying heterogeneous column flow experiments.	119
4.1	Key Parameters of Dual-Permeability Models.	139
4.2	Enhanced Sweeping of MPEMs in Dual-Permeability Models.	148
6.1	New depths of five-spot wells.	184
6.2	Tabulated mass balance for all well pairs dual tracer tests.	201
6.S1	Correcting factors for different well pairs.	213

CHAPTER 1

GENERAL INTRODUCTION

Understanding how fluids move through the subsurface and engineering the flow so that it becomes more uniform is important in applications ranging from oil and geothermal energy recovery to CO₂ sequestration and radioactive waste containment. Determining how fluids move in the subsurface is difficult. Bromide and iodide tracers that are easily detected, inert, and inexpensive diffuse so quickly into the rocks or sediments adjacent to fractures that their fracture-controlled flow is masked. In principle nanoparticle tracers would travel with the fluids and show the true fracture pathways, but poor tracer stability and the tendency of particles to stick in fractures and pores has until now limited their utility. Recently, inert nanoparticle tracers have been successfully synthesized for dispersion in aqueous and supercritical CO₂ systems. The purpose of this dissertation is to describe how these inert nanoparticles can be used both to detect fracture flow in the subsurface and to evaluate the uniformity of the flow.

Chapter 2 addresses how super-critical CO₂-philic nanoparticles might be used to assess the viability of sequestering CO₂ in shale. Geological sequestration of CO₂ could mitigate greenhouse warming but subsurface storage capacity, security, and costs are challenges that must be addressed. Sequestration in shale could be one way to meet these challenges. Shale is the most abundant rock type in the crust¹⁵ and can have high matrix porosity¹⁴, especially in shale with high TOC^{4,6,11}. The low permeability of shale reduces the risk of escape of buoyant CO₂. CO₂ injection

increases hydrocarbon recovery^{3,10} and thus sequestration in shale gas operations using existing wells could greatly reduce the costs while increasing gas recovery. An important remaining question, however, is how uniformly CO₂ introduced through fractures will fill the shale matrix pore space. Chapter 2 shows how matrix sequestration can be assessed by comparing the transit of a chemical, which diffuse into the matrix, with particles which diffuse much less. A mathematical relation capturing this contrast is used first to design laboratory experiments that demonstrate the method, and then to design a field test that can determine the potential of a specific shale to sequester supercritical CO₂. The key to the method is nanoparticles that do not stick and are not retained in other ways in passing through the shale. We demonstrate that the particles synthesized for this project are not retained in the analogue laboratory matrix, and they should not be retained in shale either,

In Chapters 3, 4, and 5 we described how nanoparticles can be used in a properly designed laboratory column to assess how much additives increase the uniformity of fluid flow. Flow uniformity is desirable in many applications. When water flooding an oil reservoir, for example, oil can only be produced from the permeable zones where the flooding occurs. Heat extraction from geothermal reservoirs is degraded if re-injected water short circuits to production wells. Flow remediation agents such as foams, gels, and polymers have been developed to make flow more uniform by preferentially clogging permeable channels. But it is difficult to realistically and quantitatively assess the performance of flow alteration agents in the field, and there is not a method for realistically doing this in the laboratory. Usually, changes in flow in parallel tubes filled with material of different permeability

are taken as a measure of remediation. However, this method does not account cross flow between permeable and less permeable zones. Clogging a permeable column faster does not necessarily indicate that flow will become more uniform in a heterogeneous column where flow into less permeable zones might be impaired as much or more. Chapter 3 shows how changes in the fraction of the low permeability annulus of a heterogeneous column that is swept by flow can be assessed by measuring the volume of nanoparticle tracer stored in the column. The nanoparticles are critical because their low diffusion constant reduces the false storage that results from tracer diffusion into un-swept areas where there is little or no flow. Experiments are first carried out to optimize column design and operation (Chapter 3), and then (Chapter 4) the flow remediation achieved by injecting elastically deformable microspheres (MPEMs) is quantitatively determined from changes in nanoparticle storage.

In developing these methods it proved vital to eliminate even small heterogeneities in column packing. Even with strict adherence to well-established wet packing protocols^{12,13} repeatability between experiments was poor. After extensive investigation, we found that the poor column performance was related to a previously largely un-recognized impact of very small amounts of air trapped at grain boundaries and adsorbed on grain defects. We found that air can exsolve from DI water in the column after it is filled with sand, and can adhere to sand as it is prepared for wet packing before it is placed into the column. Chapter 5 describes a packing protocol that uses evacuation at all stages of material preparation and column packing to eliminate flow heterogeneities associated with air and produce very repeatable column

flow performance. The new protocol should be of interest in applications where precision in column testing is desired, and it was critical to the results reported in Chapters 3 and 4.

Chapter 6 describes a field experiment in which we deploy a CDot nanoparticle tracer together with a conventional CsI chemical tracer to investigate the pattern of flow in a single, natural, sub-horizontal fracture in Altona Flat Rock in north-eastern New York. The uniformity of flow in fractures is critically important in enhanced geothermal systems because channeling of flow in the fractures can reduce and delay heat extraction⁷. The Altona site provides a natural laboratory for studying flow in a single crack, and many experiments have been previously run there^{1,2,5,8,9,16,17}. Our interest was to test whether our nanoparticles were inert (non-sticking) in a natural environment, and, in addition, to determine if their low diffusion could provide information on flow heterogeneity in a crack that was not provided by standard chemical tracers. The CDot and CsI tracers were injected and produced simultaneously in 6 different well pairs where the wells were 5 to 7 meters apart. The CDot tracer proved to be as inert as the iodide tracer, but its concentration in the recovered fluids was more variable in 3 of the 6 tests. In these 3 tests the Cs⁺ tracer was also adsorbed more. Our preliminary interpretation is that the extra variability of the particle tracer reflects different flow channels through the fracture, and that the iodide tracer is less variable because it diffuses more and is thus more damped. To our knowledge is the first time a certifiably inert nanoparticle tracer has been deployed together with a chemical tracer to investigate flow in a natural system.

In summary, this dissertation shows how inert nanoparticle tracers might be used to quickly assess the viability of supercritical CO₂ sequestration in shale, can be used to quantitatively assess flow remediation in heterogeneous laboratory columns, and can be used to measure the uniformity of flow in natural settings. The applications we discuss are just a start. The newly available inert nanoparticles we describe could find many other applications, and in addition could provide an important baseline against which interactive particles could be assessed, providing still more information about subsurface flow.

References

1. Becker, M. W., Remmen, K., Reimus, P. W., & Tsolfias, G. P. (2013). Investigating well connectivity using ionic tracers. In *Proceedings, Thirty-Eighth Workshop on Geothermal Reservoir Engineering, Stanford: Stanford University*.
2. Becker, M. W., & Tsolfias, G. P. (2010). Comparing flux-averaged and resident concentration in a fractured bedrock using ground penetrating radar. *Water Resources Research, 46*(9).
3. Van der Burgt, M. J., Cantle, J., & Boutkan, V. K. (1992). Carbon dioxide disposal from coal-based IGCC's in depleted gas fields. *Energy Conversion and Management, 33*(5), 603-610.
4. Busch, A., Alles, S., Gensterblum, Y., Prinz, D., Dewhurst, D. N., Raven, M. D., ... & Krooss, B. M. (2008). Carbon dioxide storage potential of shales. *International Journal of Greenhouse Gas Control, 2*(3), 297-308.
5. Castagna, M., Becker, M. W., & Bellin, A. (2011). Joint estimation of transmissivity and storativity in a bedrock fracture. *Water Resources Research, 47*(9).
6. Engelder, T., Cathles, L. M., & Bryndzia, L. T. (2014). The fate of residual treatment water in gas shale. *Journal of Unconventional Oil and Gas Resources*.

7. Gringarten, A. C., Witherspoon, P. A., & Ohnishi, Y. (1975). Theory of heat extraction from fractured hot dry rock. *Journal of Geophysical Research*, 80(8), 1120-1124.
8. Guiltinan, E. J., & Becker, M. (2010, May). Using harmonic hydraulic tests to estimate fractured bedrock properties and predict local heterogeneity. In *Abstracts with Programs-Geological Society of America* (Vol. 42, No. 4, p. 110).
9. Hawkins, A. J., & Becker, M. W. (2012). Measurement of the Spatial Distribution of Heat Exchange in a Geothermal Analog Bedrock Site Using Fiber Optic Distributed Temperature Sensing. In *Proceedings Thirty-Seventh Workshop on Geothermal Reservoir Engineering, Stanford, California, January*.
10. Koide, H., Tazaki, Y., Noguchi, Y., Nakayama, S., Iijima, M., Ito, K., & Shindo, Y. (1992). Subterranean containment and long-term storage of carbon dioxide in unused aquifers and in depleted natural gas reservoirs. *Energy Conversion and Management*, 33(5), 619-626.
11. Lash, G. G., & Engelder, T. (2005). An analysis of horizontal microcracking during catagenesis: Example from the Catskill delta complex. *AAPG bulletin*, 89(11), 1433-1449.
12. Nimmo, J. R., & Akstin, K. C. (1988). Hydraulic conductivity of a sandy soil at low water content after compaction by various methods. *Soil Science Society of America Journal*, 52(2), 303-310.

13. Oliviera, I. B., Demond, A. H., & Salehzadeh, A. (1996). Packing of sands for the production of homogeneous porous media. *Soil Science Society of America Journal*, 60(1), 49-53.
14. Sclater, J. G., & Christie, P. (1980). Continental stretching: An explanation of the post-Mid-Cretaceous subsidence of the central North Sea Basin. *Journal of Geophysical Research: Solid Earth (1978–2012)*, 85(B7), 3711-3739.
15. Stow, D. A. (1981). Fine-grained sediments: terminology. *Quarterly Journal of Engineering Geology and Hydrogeology*, 14(4), 243-244.
16. Talley, J., Baker, G. S., Becker, M. W., & Beyrle, N. (2005). Four dimensional mapping of tracer channelization in subhorizontal bedrock fractures using surface ground penetrating radar. *Geophysical research letters*, 32(4).
17. Tsolfias, G. P., & Becker, M. W. (2008). Ground-penetrating-radar response to fracture-fluid salinity: Why lower frequencies are favorable for resolving salinity changes. *Geophysics*, 73(5), J25-J30.

CHAPTER 2

USING CO₂-PHILIC NANOPARTICLES TO ASSESS CARBON SEQUESTRATION IN SHALE

Abstract

Fossil fuel combustion is likely to continue for some time. Sequestration of supercritical carbon dioxide in the subsurface is considered a way to reduce the greenhouse risk of CO₂ emissions, but sequestration in permeable aquifers risks escape. The low permeability of shale could greatly reduce this risk, and shale is the most abundant rock type. Of necessity injection would be through induced fractures but the storage space is the porosity of the unfractured adjacent matrix. The feasibility of CO₂ sequestration in shale thus depends on the ability of the CO₂ to diffuse from fractures into the matrix. Here we show how this can be assessed by combining inert particle and chemical components in a tracer, demonstrate the methods by carrying out laboratory experiments, and use the methods to design a field test. Sequestration potential is assessed by comparing the arrival of the particles, which diffuse less into the matrix, and the chemical, which diffuses more. A mathematical criterion is used to design the laboratory experiments. The experiments show the validity of the criterion and prove the method. The criterion (that the diffusion matrix filling time be similar to the transit time of

the chemical tracer if it fully fills the matrix) is then used to design a field test that can quickly determine the potential of specific shale to sequester supercritical CO₂. Additional matters that need to be addressed prior to a field test are outlined.

Introduction

Around 90% percent of the anthropogenic CO₂ released to the atmosphere each year comes from the burning of fossil fuels³⁰ and fossil fuel use is increasing atmospheric CO₂ concentrations to levels that are of climate concern. Yet the world economy is heavily dependent on fossil fuel resources, the global demand for energy is growing rapidly, and fossil fuel resources will remain one of the world's major energy sources for the foreseeable future. Capture and sequestration of fossil fuel CO₂ is considered an important way to mitigate the climate impact of continued fossil fuel use.

CO₂ can be trapped by dissolving in pore waters, as discrete immiscible droplets of a non-wetting phase in individual sediment pores, as a buoyant column in connected pores confined by top and lateral seals, or as new carbonate minerals^{7,8,9}. Captured CO₂ can be sequestered in oil and gas fields, deep saline aquifers, deep coal seams, and caverns and mines^{3,4,24,27,28}. Presently the most economical sequestration is in oil and gas reservoirs because hydrocarbon recovery can be increased at the same time CO₂ is stored^{10,33}. However, the estimated CO₂ storage capacity in on- and off-shore oil and gas field is only 207,340 million metric tons³⁹. Considering the uncertainties in storage efficiencies, reservoir qualities, and enhanced recovery revenues, this capacity is optimistically only enough to sequester a few decades at the 2012 U.S. emission rate of 3,100 million metric tons of CO₂ per year.

Saline aquifers in porous sandstones or carbonates have the porosity to store one to two orders of magnitude more CO₂ (2,296,680 and 20,092,180 million

metric ton) and hold 1000's of years of U.S. 2012 emissions³⁹, but not all these aquifers are deep enough to store supercritical CO₂, and aquifer storage could be hazardous. Supercritical CO₂ has over 3 times the density of compressed methane, reaching 660kg/m³ at depths of around 800~1000 meters. Supercritical conditions allow more CO₂ to be sequestered in the same pore volume and also reduce the risk of escape by reducing buoyancy. The density of supercritical CO₂ is nevertheless less than water, and its buoyancy poses a risk for long term high volume storage in permeable formations. Sequestration in shale pore space or by precipitating CO₂ as carbonate are two ways to greatly reduce this risk^{3,25,29,31}.

Between 50 and 70% of sedimentary rock type on Earth are shales⁴⁸, and their CO₂ sequestration capacity is potentially far greater than that of saline sandstone or carbonate aquifers³⁹. Shale porosities are typically 10 to 20% at the depths required for CO₂ to have supercritical density⁴⁵. For example, an Australian shale sample from a depth of 1454 meters below seafloor, composed dominantly of illite-smectite, kaolinite and quartz, had a porosity of 20%¹¹. In organic-rich shales the porosity of the organic fraction (which can be 50 vol% TOC) can be very high (~50%)^{20,35}. Furthermore, in thermally matured shales, the kerogen is oil- and gas-wet, not water-wet and CO₂ is easily adsorbed onto the kerogen surface. For example, CO₂ is preferentially adsorbed onto Kentucky black Devonian gas shales where it displaces adsorbed methane from the clay and kerogen surface. When CO₂ is injected into coal, methane is liberated⁴¹. A recent study showed that New Albany black shales with high

total organic content have a high CO₂ storage potential, suggesting CO₂ adsorption is important^{39,41}. The Muderong Shale can sorb 1mmol CO₂ per gram of shale under reservoir conditions⁴¹, and injection of CO₂ could dissolve silicate and precipitate carbonate minerals, sequestering additional CO₂ while enhancing porosity and permeability.

CO₂ sequestration would be far safer in shale than in sandstone or carbonate aquifers because the low permeability of shale greatly reduces the risk of leakage. Thousands of feet of massive shale over a zone where CO₂ is trapped in shale in a non-buoyant distributed fashion is a safe confinement compared to a gas reservoir trapped below a seal that can breach, or CO₂ dissolved in water that can migrate^{1,11,14,26}. Capillary barriers will also promote confinement⁴⁶.

Horizontal drilling and hydrofracturing has recently enabled substantial production of gas and oil from shale. The miscibility of the CO₂ and hydrocarbons means there are no capillary entry barriers for CO₂ injection into the hydrocarbon filled pore space, and it has been found that injecting CO₂ can greatly enhance methane recovery⁵³. Using CO₂ to enhance recovery in unconventional shale reservoirs is a current topic of investigation^{15,39,42}. Sequestering CO₂ in depleted gas shales could be a natural end use of these production assets. Existing wells and pipelines would substantially reduce the costs of sequestration, and experience would be gained for eventual sequestration in shales in general.

Whether CO₂ can be sequestered effectively in shale depends on whether the CO₂ can be injected into the shale uniformly enough. If the CO₂ enters the

shale through a few widely-spaced fractures, the storage will be small, but if CO₂ can be introduced through fractures that are closely spaced enough that the CO₂ can diffuse into the matrix pore space, the storage per unit volume of shale could be high enough for sequestration to be feasible.

In previous work we have showed how dual tracer methods (a combination of inert chemical and nanoparticle tracers) can measure the uniformity of flow in fractured aqueous systems, demonstrated the methods in the laboratory, and described how they can be translated to field tests⁴⁹. The purpose of this paper is to show that these same methods can be used to assess how uniformly supercritical CO₂ can be stored in fractured shale. We report laboratory experiments that demonstrate how supercritical CO₂ storage can be assessed, and describe how field tests based on these methods can evaluate the feasibility of CO₂ sequestration in a particular shale. The experiments and methods require particles that are stable in supercritical CO₂, inert (non-sticky) to the shale matrix, and quantitatively detectable at low concentrations. New particles were synthesized by us to meet these requirements. Their synthesis and characterization are described in a companion paper⁵⁶.

Laboratory Experiments and Their Application

Conceptual Description of the Dual Tracer Method

Figures 2.1 and 2.2 illustrate how dual tracer methods can be used to assess the uniformity of flow in fractured rock systems and assess the feasibility of sequestering CO₂ in shale. Figure 2.1 depicts a fractured rock with a matrix of

low enough permeability that flow is only through the fractures. If inert particles and a chemical are injected, the particles, with their low diffusion constant will move mainly through the fractures, but the chemical with its much higher diffusion constant will diffuse into the matrix. Figure 2.2 illustrates the different fashions in which the particles and chemical will move through fractured rock.

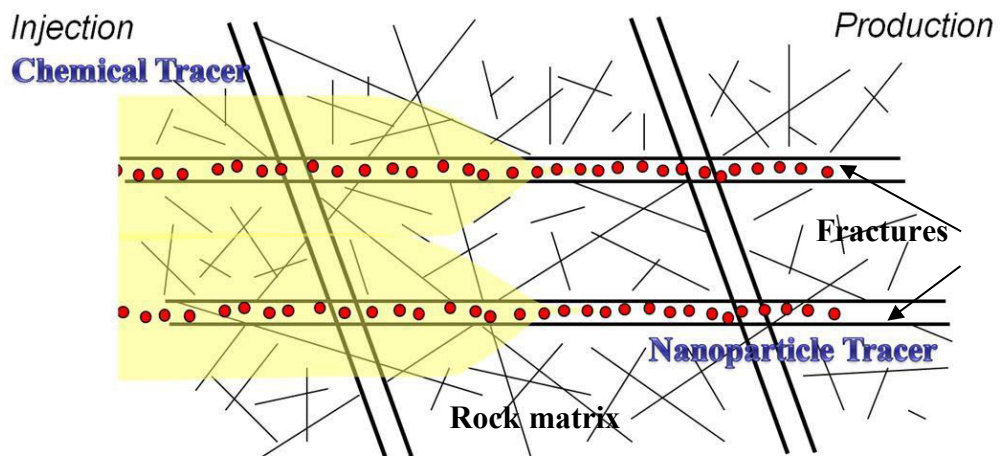


Figure 2.1: Illustration of dual tracer flow behavior in shales. Red spheres represent nanoparticles and yellow shading represents the diffusive chemical tracer. The particles travel much faster through the fractured rock because they diffuse much less into the matrix surrounding the fractures.

Consider injecting both a particle and chemical tracer in a block of fractured rock from one side and recovering the tracers on the other side. Keeping track what went in and what came out, the amount of tracers retained in the block can be calculated with the following formula:

$$f = \frac{\int_0^t Q \left(1 - \frac{C(t)}{C_0}\right) dt}{V_{\text{total}}} , \quad (2.1)$$

where f is the fraction of the total pore volume of the block that is filled one of the tracers, C_0 is the mass fraction (kg tracer per kg solvent) of tracer injected into the block, $C(t)$ is the mass fraction of tracer leaving the block, Q is the flux of tracer through the block ($\text{m}^3 \text{ s}^{-1}$), $\left(1 - \frac{C(t)}{C_0}\right)$ is the volume fraction of injected tracer retained in the block, t is the time since the start of tracer injection, and V_{total} is the total pore volume (fractures plus matrix porosity) of the block.

Figure 2.2 uses equation (2.1) to illustrate sequestration. It plots the fraction of the total pore volume of the block that is filled with tracer against the number of total pore volumes injected. If there is no diffusion from the fractures into the matrix, the tracer fill only the fracture porosity, and the sequestration will consist of filling only the fractures as illustrated by line (A). If diffusion into the matrix is very rapid, the total porosity will be filled with tracer before the injected tracer passes through the block, as illustrated by line (D). Curves (B) and (C) illustrate sequestration in cases where the tracer diffuses into portions of the matrix but not all of it.

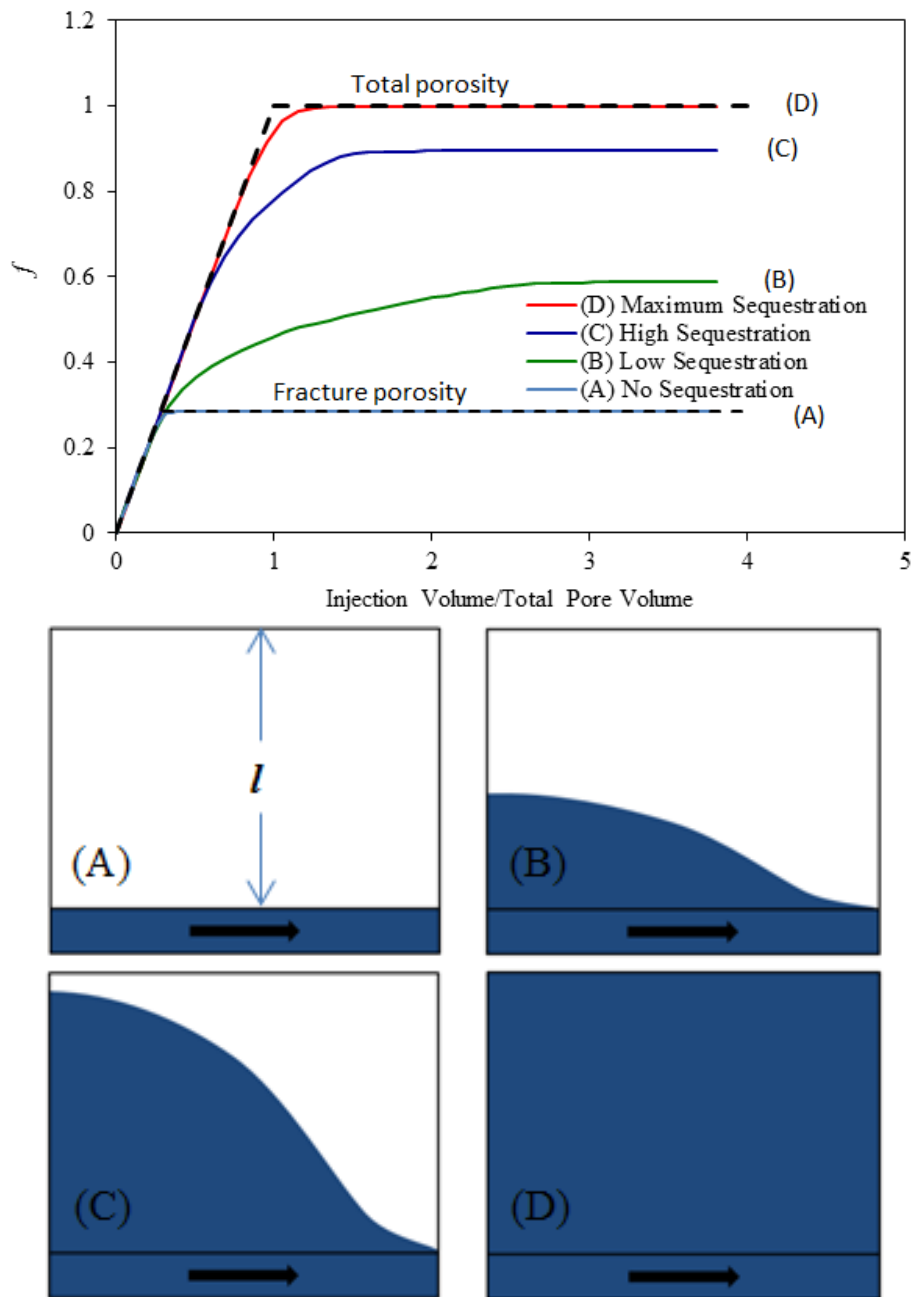


Figure 2.2: Illustration of sequestration for inert substances injected into a fracture which diffuse to different degrees into the adjacent matrix. The top figure shows the fraction of pore space filled. The bottom figure shows flow-parallel profiles of the fill. Labels A-D tie the curves to profiles.

Because the matrix porosity will typically be much greater than the fracture porosity, successful sequestration will depend on the ability of the injected material to diffuse into the matrix from the fractures. Previous work⁴⁹ has demonstrated that the inverse Peclet number is a useful measure of this. The inverse Peclet Number, N_{iPe} , of the nanoparticle and chemical tracers is defined as the ratio of the transit time of the fluid through the total porosity (e.g., the time to inject one total pore volume of solvent) to the time required for diffusion to fill the matrix.

$$N_{iPe} = \frac{\text{time to fill total porosity}}{\text{Matrix diffusion time constant}} = \frac{t_{\text{fill}}}{\tau_{\text{diff}}} \quad (2.2a)$$

The significance of equation (2.2a) is that from previous experiments⁴⁹ we know that if N_{iPe} is much less than 1, the tracer will pass through the block without substantially filling the matrix and follow line (A) in Figure 2.2. If, however, N_{iPe} is close to or greater than 1, the tracer will substantially diffuse into the matrix and follow lines (B), (C) or even (D). We can thus use equation (2.2a) first to design the laboratory experiments that demonstrate our tracer particles and methods, and then use equation (2.2a) again to design field experiments that can assess the sequestration potential of a shale formation. $N_{iPe} \sim 1$ assures that the chemical tracer will diffuse substantially into the matrix. Since τ_{diff} for the particle tracer is much longer than for the chemical tracer, this criterion also assures that the particle tracer will diffuse much less into the matrix and that the separation of the particle and chemical tracer curves will be large enough to provide a strong signal for modelling interpretation.

Consider a single fracture and its associated adjacent matrix, as illustrated in Figure 2.2b. The transit time of fluid through the total porosity of the system is the transit time through the fracture, t_f , times the total porosity (matrix plus fracture) divided by the pore volume of the fracture, $\frac{V_t}{V_f}$. The transit time through the fracture is of course either the pore volume of the fracture divided by the injection rate into the fracture or the length of the fracture L divided by the true average velocity of the fluid in the fracture, v_f . The time to diffusively fill the matrix is the square of the spacing between fractures, l^2 , divided by 4 times the effective diffusion constant of the tracer or chemical being sequestered, D_{em} . Note that l is the portion of the matrix associated with each fracture. The other half of the matrix is associated with the adjacent fracture, so the spacing between fractures is $2l$.

$$t_{fill} = t_f \frac{V_t}{V_f}, \quad \tau_{diff} = \frac{l^2}{4D_{em}} \quad (2.2b)$$

The effective diffusion constants in the fracture and matrix, D_{em} and D_{ef} respectively, are:

$$\left\{ \begin{array}{l} D_{ef} \\ D_{em} \end{array} \right\} = D_o \left\{ \begin{array}{l} \Phi_f / \tau_f \\ \Phi_m / \tau_m \end{array} \right\} + \left\{ \begin{array}{l} a_L \Phi_f v_f \\ 0 \end{array} \right\} \quad (2.2c)$$

where D_o is the diffusion constant of the tracer in its solvent; τ_f and τ_m are the tortuosity of the fracture and matrix pore space; Φ_f and Φ_m are the porosities in the fracture and matrix; a_L is the longitudinal (parallel to flow direction) dispersion coefficient in the channel; and v_f is the true average velocity of the fluid in the fracture. We assume that only longitudinal dispersion is significant in the fracture and that there is no flow in the matrix. In the laboratory

experiments we describe below the porosity and tortuosity are unity and $\Phi_f/\tau_f=\Phi_m/\tau_m=1$.

Experiments Demonstrating Dual Tracer Methods for Supercritical CO₂

Particle requirements and synthesis. Shale is a lithified, fissile, fine-grained argillaceous mix of clay and quartz with organic matter sometimes abundant and a grain size <63 μm^{23,48,54}. Shale permeability is typically well below a millidarcy and compacted shale permeability is <1 microdarcy^{13,40}. Samples from the organic rich Devonian black shales of the Appalachian basin have a permeability of ~20 microdarcies⁴⁷. Total porosity can be appreciable (20% or more)^{13,40,45}.

For CO₂ to be injected into shale and sequestered, the shale will need to be hydrofractured as it is when gas is recovered from gas shales. There naturally existing joints are accessed by horizontal drilling and hydraulic fracturing in a way that maximizes hydrocarbon recovery²¹. The tracer particles need to be small enough to move through the induced and natural fractures. At the same time the particles need to be large enough that they have a diffusion constant 1.5 to 2 orders of magnitude smaller than a typical chemical tracer molecule. Both these criteria are met if the particles are ~50 nm in diameter.

The particles should not stick to any of the minerals in the shale that they might encounter (i.e., be chemically inert). In aqueous solution the interaction between particles and rock minerals that could cause sticking is electrostatic³⁸. Supercritical CO₂ exhibits both non-polar (low dielectric constant), and polar

properties (Lewis acidity and strong quadrupole moment)⁶, retaining both gas-like and liquid-like qualities. Electrostatic interactions with minerals or chemicals or particles dispersed in supercritical CO₂, although possible, it is likely to be much less of an issue as it is in aqueous solutions.

The particles need to be detectable at ppm concentrations to be useful in tracer tests (otherwise the quantity of particle tracer needed will be excessive), and if the detection method is fluorescence as it is here, fluorescence as well as the other particle properties should be stable for at least several months at temperatures of ~60°C, the typical temperature encountered at 2 km depth where supercritical sequestration will occur.

The synthesis of nanoparticles that are stably dispersible in supercritical CO₂ (scCO₂) and easily detectable at low concentrations is challenging. As described in a companion paper, our basic strategy was to graft a scCO₂-phylic polymer to the particle core and add fluorophore molecules to make the polymer corona fluorescent. Initial attempts were disappointing. The scCO₂-philic, UV scattering, SiO₂-cored, polymer-decorated particles that we initially synthesized were poly-dispersed, only moderately stable, detectible only with UV absorption/scattering, and too large (~300 nm in diameter) for tracer tests in shale. The methods that we ultimately developed produce polymerized mono-dispersed batches of SiO₂ and Fe₃O₄ cored nanoparticles of uniform ~40 nm diameter (including the polymer coronae) which show little tendency to agglomerate, and have good thermal stability. The key to successful particle synthesis proved to be paying great attention to the polymer grafting process

and keeping the particles dispersed throughout all steps of the synthesis. Details are given in the companion paper⁵⁶.

Experimental chemistry. Performing the dual tracer laboratory experiment with scCO₂ would require operating under high pressure. To avoid this complication we chose to use a scCO₂ analogue that is liquid at room temperature and atmospheric pressure. The scCO₂ analogue is hydrofluoroether 7200 or HFE 7200, a chemically benign³⁷ solvent that is available from 3M⁵¹. Fluoropolymers that suspend nanoparticles in HFE should also suspend them in scCO₂.

The reference chemical tracer we use is Trifluorotoluene or TFT. The structure of TFT molecule is very similar to that of the toluene molecule. It consists of a benzene ring in which fluorine takes the place of hydrogen. Trifluorotoluene is an inert, small molecule which is easily detected with UV absorption spectroscopy, and it is superbly soluble in HFE. It is a dumbbell-shaped molecule with principle axis diameters of 200 and 500 pm. The viscosity of HFE at room temperature and pressure is 600 Pa s. The diffusion constants of TFT in HFE calculated from the Stokes Einstein equation for the two axis dimensions are 1.22 and 3 cm²/day. Our experiments (see discussion below) suggest the effective diffusion constant for TFT in HFE is ~2.2 cm²/day.

At room temperature, the diffusion constant of the 39 nm diameter SiO₂-cored nanoparticles particle in HFE is 0.0157 cm²/day, and the diffusion constant of the 43 nm Fe₃O₄-cored nanoparticles in HFE is and 0.0142 cm²/day.

The injected concentrations for the SiO₂-cored nanoparticle and conservative chemical tracer TFT are 1930 ppm and 436 ppm for experiment 1, and that of the Fe₃O₄-cored nanoparticle tracer and TFT are 334 ppm and 515 ppm for experiment 2. The particle and TFT concentrations are measured with a Molecular Devices SpectraMax M2e spectrometer to $\pm 1\%$ accuracy.

Elaboration of the diffusion constant calculations from the Stokes Einstein equation is provided in the supplemental material.

Experimental design. The basic design of the laboratory apparatus we used in the work reported here consists of a channel with attached slit as shown in Figure 2.3. Initially the apparatus is filled with pure HFE 7200. HFE with dispersed particles and TFT (the two tracers) is then passed through the channel. Both tracers diffuse into the slit from the channel, but the chemical TFT tracer diffuses much more because of its higher diffusion constant. The difference in effluent tracer concentrations measures their different degrees of diffusion into the slit, and the successful modelling of the effluent curves constitutes the test that the particles and methodology are operating as expected.

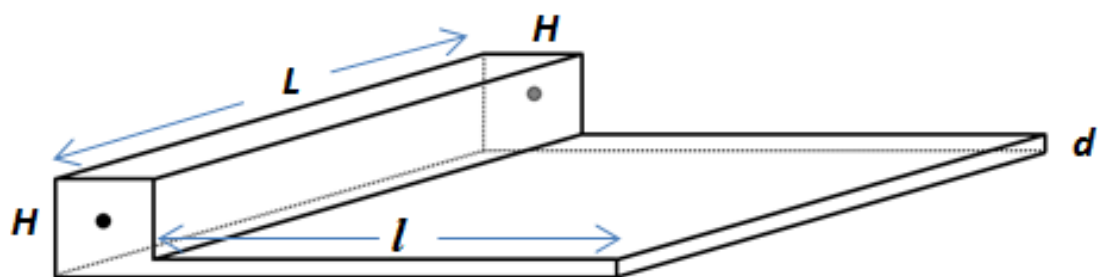


Figure 2.3: Schematic of glass Hele-Shaw experiment apparatus. Two cells were constructed with slightly different core channel dimensions, $H = 8$ mm and 12 mm. The core length and slit dimensions are the same for both cells: $L = 100$ mm, $l = 80$ mm, $d = 2$ mm. The volume of the channel (c) and slit (s) for the two cells are: $V_c = 6.4$ and 14.4 cm 3 , and $V_s = 16$ cm 3 .

The design criteria are that the diffusion slit have sufficient volume compared to the channel that substantial diffusion into it is easily measured. At the same time the slit should be thin enough that flow through it is small compared to the flow through the core. The core needs to be long enough that the chemical can diffuse into the slit in one core transit time. The core needs to have sufficient volume that 20% or less of its volume is sufficient for fluorescent concentration measurements.

Table 2.1 shows how the design and operation of the cell meet these criteria. The volumes of the channels are sufficient to supply 9 to 20 samples (0.7ml each) for analysis, which is sufficient to define the particle arrival in the effluent with adequate resolution even in the case that there is no diffusion into the slit. The 16 cm³ pore volume of the slit is more than the pore volume of the channel in either apparatus, so diffusion into the slit should be easily measured. The ratio of the fill time to the chemical matrix diffusion time, $N_{ipe} = t_{fill}/\tau_{TFT} = 2.1$ to 2.9, which means that there should be ample time during flow through the channel for the chemical tracer to diffuse into the slit. At the same time, since the diffusion constant for the particles is ~0.015 cm²/day, the inverse Peclet Number for the particle tracer is 0.016 to 0.018, and the particle tracer should diffuse much less into the slit, and arrive significantly faster than the chemical tracer in the effluent.

Table 2.1. Cell design parameters. Symbols are defined with values indicated in Figure 2.3 and the discussion above. The experimental injection rate $Q=1.44 \text{ cm}^3 \text{ day}^{-1}$. t_f is the transit time of the channel at this injection rate. τ_{TFT} is calculate for $D_o^{TFT} = 2.16 \text{ cm}^2 \text{ day}^{-1}$. Nipe is the inverse Peclet Number defined in equation (2.2a).

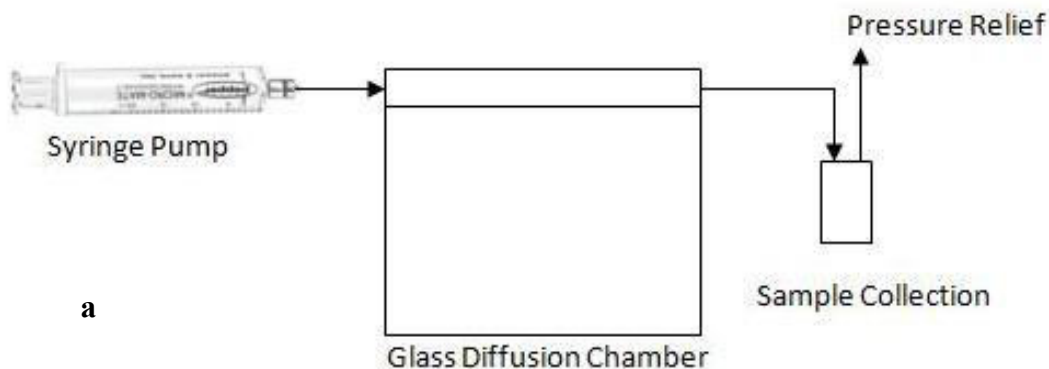
	V_{chan}	V_{tot}/V_{chan}	D_o^{TFT}	$\tau_{TFT} = \frac{\ell^2}{4D_o^{TFT}}$	$t_f = \frac{V_{chan}}{Q}$	$t_{fill} = t_f \frac{V_{tot}}{V_{chan}}$	N_{ipe}
	[cm ³]	[-]	[cm ² d ⁻¹]	[days]	[days]	[days]	[-]
Cell 1 (H=0.8 cm)	6.4	3.5	1.2-2.16-3	7.4	4.4	15.5	2.1
Cell 2 (H=1.2 cm)	14.4	2.1	1.2-2.16-3	7.4	10	21.1	2.9

For an injection rate of $1.44 \text{ cm}^3/\text{day}$ the Reynolds number for the two cells is 0.0048 and 0.00323, respectively. Since the Reynolds number is well below 1, the flow is laminar and the Stoke-Einstein equation provides a valid estimate of the solute diffusion coefficients. Details are given in the supplemental material.

Construction of apparatus. Because we are using a volatile organic solvent for our diffusion experiments, glass and stainless steel parts are required to avoid interactions between the solvent and apparatus. Two glass Hele-Shaw diffusion cells were fabricated with the dimensions described above by Specialty Glass Products Inc. The cells consist of a machined/etched glass plate covered with a second glass plate. Inlet and outlet holes were drilled before sealing the top cover glass. The glass was polished before shipping. The brittleness of the glass precluded the installation of glass nipples extending out of the apparatus, and it proved not to be trivial matter to attach stainless tubing to the small holes drilled in the glass. We used Polydimethylsiloxane (PDMS) with a 1:8 hardener/base ratio as an intermediate elastic material to hold our stainless steel tubing tight while it was anodically bonded to the glass to create a tight seal. We further secured the tubing with a thin layer of Corning silicon glass sealant to minimize damage during movement and use. Finally we enclosed the entire apparatus in PDMS to create a pressure-tight, rigid system, and eliminate any potential evaporation of our carrier solvent HFE 7200. Vacuum grease is applied to the connections to prevent evaporation. PDMS is very inert, is not soluble in HFE 7200 or water, and HFE 7200 is highly evaporative. Diagrams

detailing these steps are provided in the supplemental material. One of the PDMS encased cells is shown in Figure 2.4.

Experimental procedures. The chemical Trifluorotoluene (TFT) tracer and the SiO_2 and Fe_3O_4 cored nanoparticles are premixed at a known concentration in the Hydrofluoroether (HFE) solvent. The solvent is held in a 50ml glass syringe mounted on a high precision syringe pump, as illustrated in Figure 2.4. The injection rate was controlled at 1.44 cc/day for both experiments in both cells. Each experiment lasted about a month. At the common injection rate of 1.44 cc/day, 1 core pore volume was injected in ~4.4 days in the Cell 1 apparatus hosting the SiO_2 nanoparticle experiment, and 1 core pore volume was injected in 10 days in the Cell 2 Fe_3O_4 nanoparticle apparatus. One total pore volume (matrix plus core) was injected into the first apparatus in 15.5 days and into the second apparatus in 21.1 days, as shown in Table 2.1.



a

Glass Diffusion Chamber

Sample Collection



b

Figure 2.4: a) Schematic of experimental setup. b) Image of experimental setup showing class cell encased in PDMS as described in the text.

Samples were collected in ~0.7 ml aliquots. To minimize the evaporation during the measurements, the fluid sample is withdrawn from the sample collection vial with a glass syringe and quickly injected to a clean glass cuvette with its top sealed. Glass cuvettes and glass syringes are cleaned thoroughly, dried completely, and reused for the next sample measurement.

The effluent concentration of nanoparticle tracers is determined using a calibration curve and the effluent fluid's fluorescence as measured with a SpectraMax spectrophotometer built by Molecular Devices Company and Proview software. The TFT concentration is measured by UV absorption using the same spectrometer. Once the concentration of the particles in the solution has been determined from their fluorescence, the UV absorption of the particles is subtracted from the UV absorption spectra of the solution, and the concentration of TFT determined from the residual UV absorption. The calibration curves and the measurement procedures are described in the supplemental material.

Experimental results and interpretation. Figure 2.5 plots the concentrations of the tracers in the effluents of the two ~1 month experiments as a function of time. After a month of injection the nanoparticle tracers reached more than 90% of their injected concentrations in both experiments. The TFT tracer achieves between 60% and 70% of its injected concentration. The results of the two experiments are similar even though they were carried out in apparatus of slightly different design and used nanoparticles of similar size but different core material. In both cases the nanoparticles arrived before the chemical tracer.

This reflects the fact that the chemical tracer diffused more into the slit adjacent to the core flow channel than did the nanoparticles.

Figure 2.5b compares models of the effluent tracer concentrations to the measured data in Figure 2.5a. The effluent history, the concentration of the tracers along the core channel, and diffusion into the slit are modelled using operator splitting methods. In this method, the core channel fluid is advanced in discrete time increments after which the diffusion into the matrix is calculated using finite element methods as described in a previous paper⁴⁹. The longitudinal dispersion is calculated by multiplying the longitudinal coefficient a_L by the longitudinal (channel parallel) velocity in the slit v_c as indicated in equation (2.2a). The models shown in Figure 2.5b assume there is no flow in the slit. The model curves use the diffusion constants calculated from the Stokes Einstein equation that are listed in Table 2.2. a_L is the only free parameter in the fitting. The best fit is attained for a_L between 1 and 1.5 cm. The dispersion constant of a channel should be similar to the dimensions of the channel, which in our experiments is ~1 cm. A dispersion constant between 1 and 1.5 cm is thus reasonable.

The agreement between experimental observations and model predictions, although not perfect, is quite good. We believe the discrepancy is related to imperfections in the model. Taking into account flow in the slit (which we do not present here) improves the agreement only marginally. The dispersion in the first part of the channel where the connector tube enters and the flow then expands to the full core channel is complicated and not simulated by the model.

These complications will increase dispersion in the initial tracer arrivals and affect particularly the initial particle arrival. These model imperfections are not important for the later portion of the particle arrival curve or to our conclusion that both the chemical and nanoparticle tracers behave as expected for inert tracers our experiments. The modelling success demonstrates that the separation of chemical and nanoparticle tracers can quantitatively measure matrix (slit) diffusion.

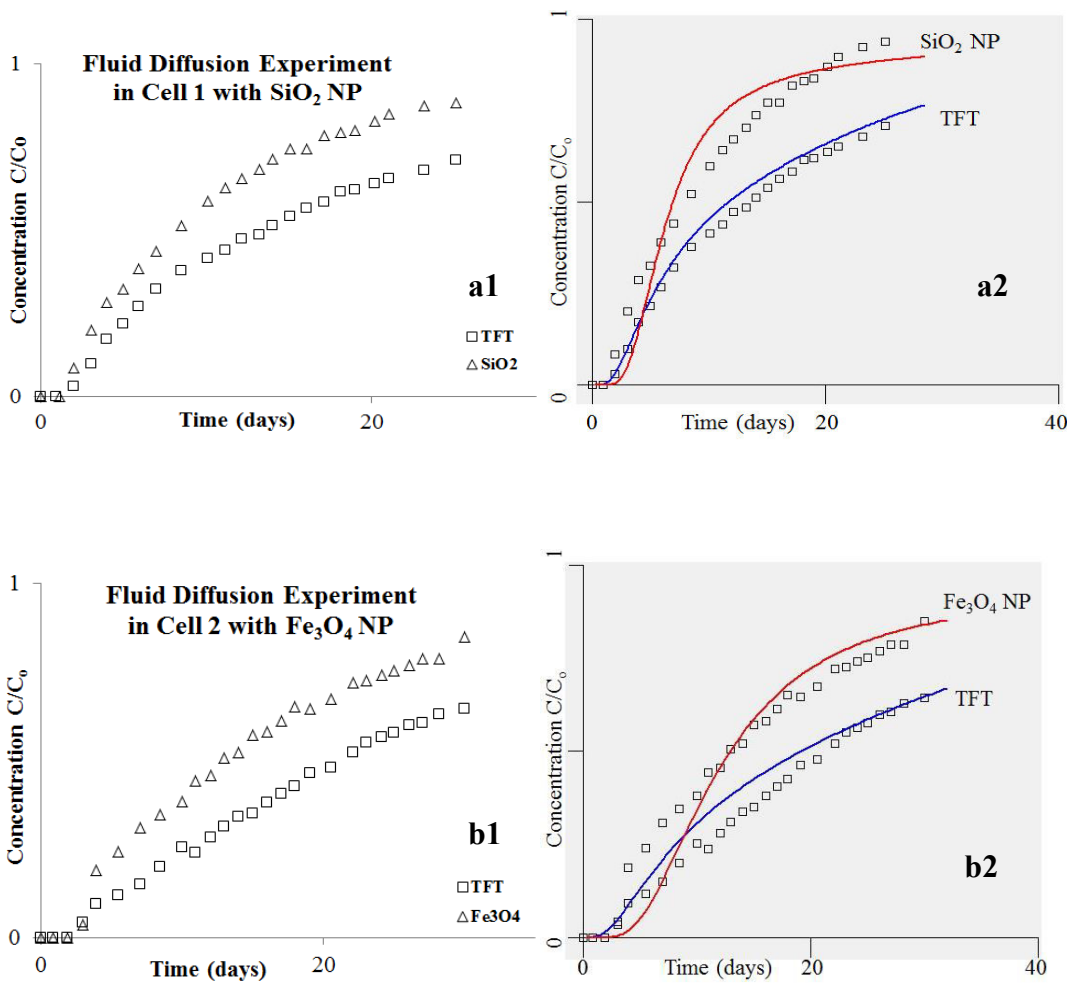


Figure 2.5. (a1, a2) Effluent concentration as a function of time for experiments carried out in HFE (a proxy solvent for supercritical CO_2). (b1 and b2) Comparison of calculated effluent tracer concentrations to data in (a1 and a2)

In the next section we show how these same methods can be used to design field tests which can quickly determine the potential for scCO₂ sequestration.

Table 2.2. Diffusion constants for the particles and chemical TFT tracer in HFE, estimated from the Stokes-Einstein equation (see supplemental material). The range in D_o for TFT reflects the maximum and minimum dimensions of the molecule. The middle bold value provides the best fit the experiments in Figure 2.5.

	$D_o[\text{cm}^2/\text{s}] \times 10^5$	$D_o[\text{cm}^2/\text{day}]$	$x[1 \text{ day}] =$
TFT	1.4 - 2.5 - 3.55	2.16	$2\sqrt{D_o t}$
SiO_2 NPs	0.0182	0.016	0.25
Fe_3O_4 NPs	0.0165	0.014	0.24

Translation to the Field

The methods described provide a basis for designing field tracer experiments that can give an early indication of the viability of sequestering carbon dioxide in shale. Consider, for example, a two well test in which supercritical CO₂ containing nanoparticles and TFT tracers are injected into a methane-filled and fractured shale. The diffusion constants for the nanoparticles, TFT, and the inter-diffusion of methane and CO₂ are calculated in the supplemental material and shown in Table 2.3.

Table 2.3. Diffusion constants for 40 nm diameter particles, TFT, and methane in supercritical CO₂, estimated as described in the supplemental material. The distance these species will diffuse in 1 day through a porous media with pore tortuosity $\tau_m=3$, and the diffusional relaxation time of a matrix with half-width $l=5$ or 50 centimetres are also shown.

	D _o [cm ² /day]	x[1 day] = 2 $\sqrt{D_o t / \tau_m}$	$\tau = \tau_m \ell^2 / 4D_o$	$\ell = 5\text{cm}$	$\ell = 50\text{cm}$
40nm diameter np	0.48	0.8	39 days	11 years	
TFT	38.5	7.2	0.5 days	48 days	
Inter-diffusion CO ₂ and CH ₄	88.7	10.9	0.2 days	21 days	

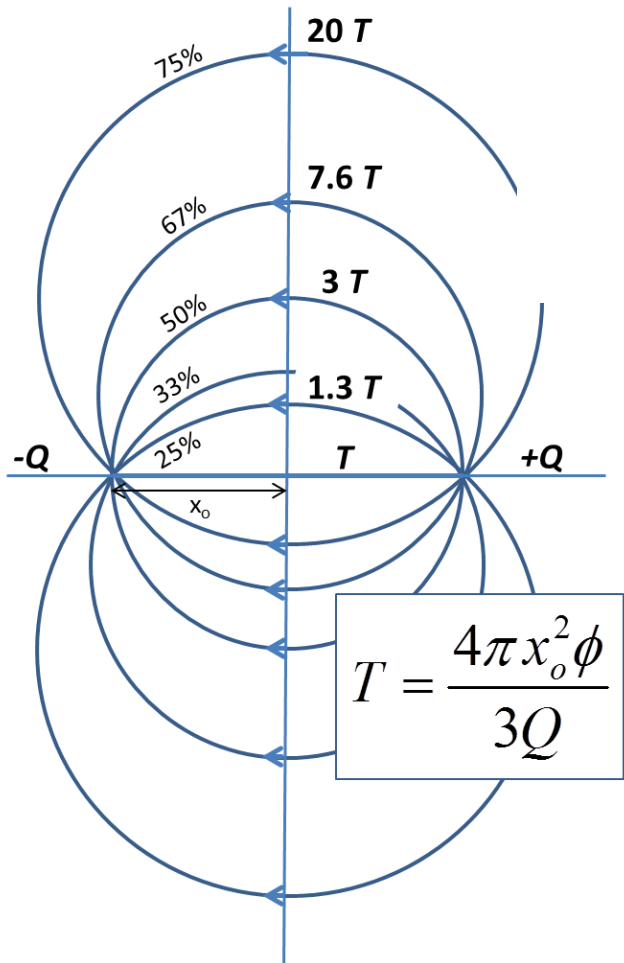


Figure 2.6. Streamlines showing the flow between an injection well and a production well separated by a distance $2x_0$ through a porous media of uniform permeability and total (matrix plus fracture) porosity, ϕ . The injection and production rate flux equal $\pm Q$. The bold labels show the times required for flow along various streamlines to reach the recovery well as multiples of the shortest transit time, T . The percent labels indicate the percentage of tracer from the injection well that is captured by the production well when the tracer from that streamline arrives.

For a total porosity of $\phi = 10\%$, a well separation of $2x_0 = 5\text{m}$, and injection and production rates of $Q = 20 \text{ m}^3 \text{ m}^{-1} \text{ d}^{-1}$, the transit time $T = 0.5 \text{ days}$. Since this travel time is the same as the diffusional matrix relaxation time for the chemical tracer TFT (Table 2.3, column 4), this well separation and injection rate meets the design criterion for a successful dual tracer test.

The field test design criteria is that the total transit time for fluid fully filling the total porosity be about equal to the diffusional relaxation time of the matrix shown for two fracture spacing in the last two columns of Table 2.3. The shortest transit time for flow between two wells in which the injection and production are equal is shown in Figure 2.6. For an injection (and production) rate of $20 \text{ m}^3 \text{ m}^{-1} \text{ d}^{-1}$ and a well separation of 5 m, the transit time is ~ 0.5 days, which is about the same as the matrix relaxation time for TFT if the fractures are 10 cm apart. An injection rate of $20 \text{ m}^3 \text{ m}^{-1} \text{ d}^{-1}$ is a typical injection rate during hydrofracturing and about the maximum rate one could imagine injecting. Table 2.3 shows that for wells separated by 5 m and this injection rate there will be good separation of the chemical and particle arrival curves in the production well if the fracture spacing is ~ 10 cm, but if the fractures are ~ 1 m apart, there will be very little separation because neither the chemical nor the particle tracer will diffuse significantly into the matrix. Thus, a particle-chemical dual tracer test of this design could diagnose the spacing of flow fractures and assess the viability of scCO₂ sequestration in shale, or any other fractured rock. A simple test could distinguish a favourable ~ 10 cm fracture separation from an unfavourable ~ 1 m separation.

Discussion, Summary and Conclusions

Discussion

The first test of the kind described above is likely to be carried out in a depleted gas shale because the injected CO₂ would have the added benefit of enhancing gas recovery and the well infrastructure would already be mostly in place and paid for. In shale gas recovery, typically about 8 wells are drilled from a pad extracting gas from a square mile of subsurface shale, as shown in Figure 2.7. Each well taps ~80 acres and lies about 200m from its neighbours. A dual tracer test might be carried out by drilling a short lateral well 5 m distant from neighbour well and packing off a ~50m interval in both wells as shown in Figure 2.7a.

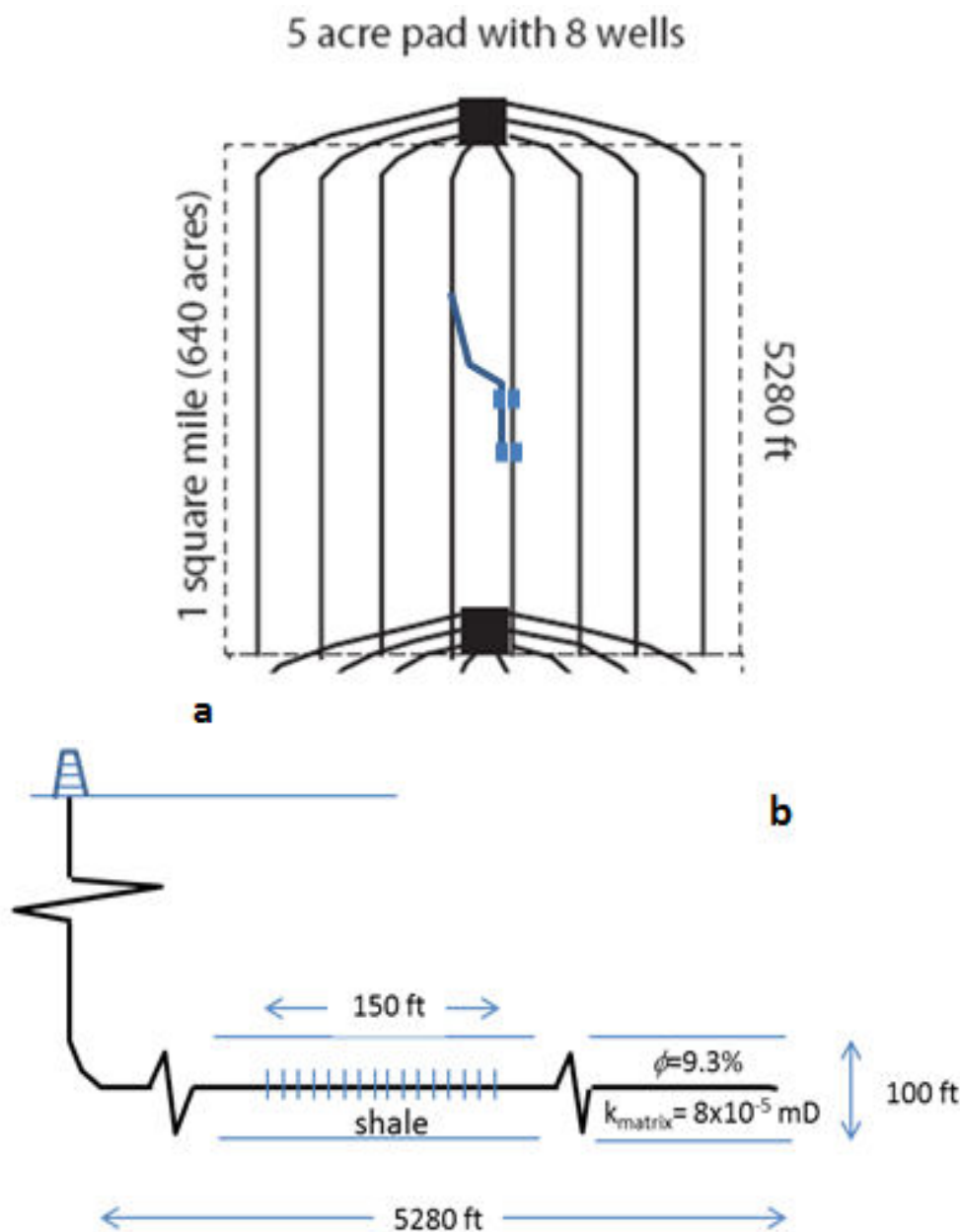


Figure 2.7. Illustration of possible test in a depleted gas shale. The Union Springs gas shale in Pennsylvania is taken as a specific example. It is about 100 ft thick and has a total porosity of 9.3% and a matrix permeability of $\sim 8 \times 10^{-5}$ mD. (a) Plan view of 8 wells drilled from a pad extracting gas from a square mile area. A lateral drilled from one well to parallel another at ~ 5 m distance and packed off over a 50 m interval is shown. (b) A cross section showing the packed off 50 m interval in one of the wells.

Assuming that 50-mesh sand is carried into the fractures in a hydrofracturing operation, the fracture aperture is ~0.5 mm. If the fractures were 10 cm apart, the propped fractures could increase the base porosity by 3% so that the total porosity is increased from 9 to ~12%. If the fracture spacing was 1 meter, the porosity would be increased by an insignificant 0.3%, however. For small fracture separations a correction for the increase in shale porosity related to fracturing could be important.

We have demonstrated that the particle we have synthesized do not clump or stick to the glass walls of the apparatus, but this does not mean they will not stick to the shale matrix. Experiments need to be carried out to rule out this possibility before a field test is carried out. Also, there is a substantial possibility that particles may be trapped at water-solid-gas interfaces if water is present in the shale (as it will be), even if they do not stick to shale when water is not present. This style of trapping has been observed in colloid transport in under-saturated porous media^{16,17,59}. We do not think this will be an issue if so little water is present that the water interfaces are not mobile, but under test conditions they could be mobile. This issue will need to be kept in mind as a field test is designed and interpreted.

More detailed modelling should be carried out. The model should include the sequential arrival of streamlines in the recovery well (see Figure 2.6). For example, after injection for a time equal to $3T$, 50% of the tracer steadily injected in the injection well will have been captured by the production well and the tracer concentration could rise to 50%. The sequential arrival of tracer-

carrying streamlines from the injection well will need to be taken into account in interpretation.

The uniform fracture spacing is certainly an idealization. There will almost certainly be a distribution of fracture apertures and transmission lengths, and this will eventually need to be included in interpretive models

If supercritical CO₂ is diluted by methane from the gas shale, the density and properties of the supercritical CO₂ will change, and it is possible that this could cause the particles to come out of suspension. This potential issue should be addressed in the laboratory before a field test is carried out. Tracer stability test in different composition of CH₄-CO₂ mixtures can assess this issue.

The laboratory experiments are subject to deficiencies that will not be present in field tests. For example, dispersion will not be a factor in the field because the fracture aperture is much smaller and the distances much longer than in the laboratory experiments

Toxicity of the nanoparticles we describe here will need to be addressed. Carbon-cored nanoparticles with similar polymer coronae have very low toxicity^{5,12,44,50,57,58}, and we expect this will be the case for our scCO₂-phyllitic particles as well. But it may be important to demonstrate this is the case.

Summary and Conclusions

We have grafted polymer coronae containing fluorophore molecules to SiO₂- and Fe₃O₄-cores to produce ~40 nm in diameter particles that are stably dispersible in supercritical CO₂ (scCO₂) and detectable to ppm concentrations by their fluorescence. These newly developed particles are significant because,

as we show here, they can be deployed together with more diffusive chemical tracers in field experiments and their accelerated arrival at a production well relative to the chemical tracer measures how much of the shale pore space can be filled with supercritical CO₂. Assessment of the sequestration potential of a shale by other means could take many years.

The method of using inert particles and chemical tracers to measure sequestration potential is illustrated by laboratory experiments using hydrofluoroether as a proxy for scCO₂. This polar solvent remains liquid at room temperature and pressure and is known to be a good chemical proxy for supercritical CO₂. A simple criterion is used to design the laboratory apparatus that simulates fractured shale. The apparatus consists of a 10 cm long core channel of ~1 cm² cross section connected to a thin slit. The core channel represents the fracture, and the slit the shale matrix adjacent to it. Two one month long experiments in two diffusion cells of slightly different design, one using iron and the other silica cored particles are reported. In both experiments, the particles arrive sooner than the chemical tracer trifluorotoluene (TFT) in the effluent. The differential arrivals are successfully simulated using diffusion constants calculated from the Stokes Einstein equation and a reasonable dispersion constant for flow in the channel.

The laboratory-tested and demonstrated design criterion is then applied to designing a field experiment in which supercritical carbon dioxide is injected into a previously-hydrofractured gas shale. The optimal well spacing for a dual tracer determination of sequestration potential is shown to be ~5 m, which is

much smaller than the ~200 m operational well separation typical in shale gas recovery. If a lateral were drilled 5 m from an adjacent well, tracer tests between the two wells could easily distinguish whether the fracture spacing is ~10 cm (and scCO₂ sequestration is quite feasible) or ~100 cm (a scCO₂ sequestration is problematic).

Settling of suspended particles could occur as methane mixes with injected scCO₂, and particles suspended in scCO₂ could interact with minerals in the shale. These and other issues should be investigated as part of the preparation for any future field test. What we demonstrate in this paper is that dual (particle-chemical) tracer tests could quickly determine the feasibility of sequestering scCO₂ in shale. In addition we show how a simple rule-of-thumb can be used to design laboratory and field experiments.

Acknowledgements

The work reported here was carried out under DOE Project No. DE-FE0004633 as part of a larger grant entitled “Assessment of factors influencing effective CO₂ storage capacity and injectivity in eastern gas shales” that was administered for DOE by Advanced Resources International, Inc (ARI). Mike Goodec of ARI provided valuable project advice and guidance. The experiments reported were carried out in space provided by KAUST-CU and equipment in this Cornell Center was also used. We are grateful to DOE for funding and to these other organizations for support. We thank Shivaun D. Archer of Department of Biomedical Engineering for assistance on apparatus fabrication. The idea for

the project was stimulated by discussions with John P. Martin when he was with
NYSERDA.

Supplementary Materials

Apparatus Fabrication

The cell consists of a machined/etched glass plate covered with a second glass plate, as shown in Figure 2.S1a, 2.S1b. The inlets and outlets were drilled before sealing the top cover glass. The glass was polished to ultra-fine grit before shipping to us. The brittleness of the glass precluded the installation of glass nipples extending out of the apparatus, and it proved not to be trivial to attach stainless tubing to a small hole in the glass. We used Polydimethylsiloxane (PDMS) of 1:8 hardener to base ratio as the intermediate elastic material to hold our stainless steel tubing tight while it is bonded anodically after an oxygen plasma treatment to the glass to create a tight seal¹⁸. We further secured it with a thin layer of glass sealant, and finally we immersed the entire apparatus in a closed container filled with PDMS and with blunt end syringe needle embedded within to create a pressure tight, rigid system and eliminate any potential evaporation of our carrier solvent HFE 7200 (Figure 2.S2a and 2.S2b). PDMS in all processes are cured at 60 degrees Celsius overnight each after degassing with vacuum pump. Vacuum grease is applied to the connections to prevent any potential evaporation as well. PDMS is chemically inert to many materials. It is not soluble in HFE 7200 and water. HFE 7200 is highly evaporative.

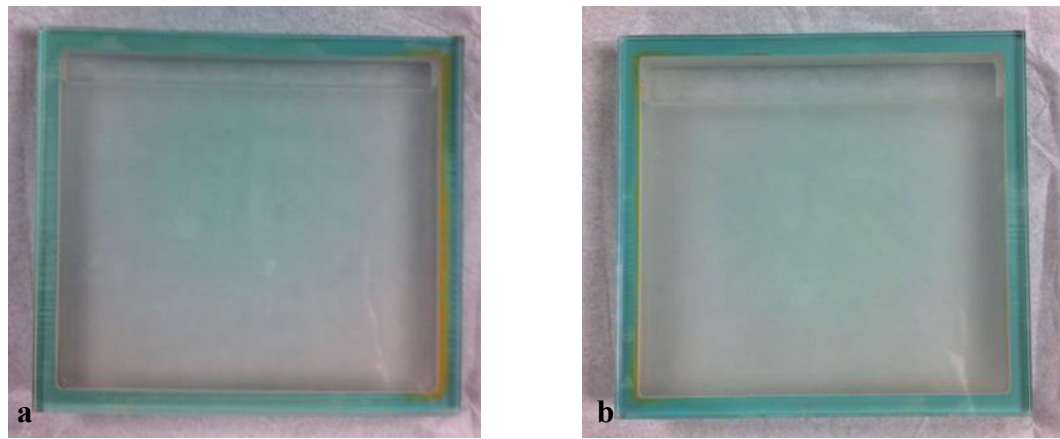


Figure 2.S1: a), b) Finished product of apparatus 1 and 2 from SGP.

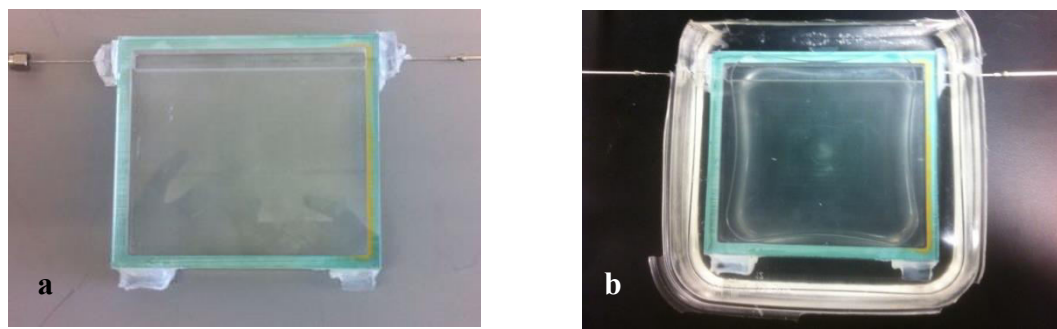


Figure 2.S2: a) PDMS securing stainless steel blunt end syringe needles in place; b) Entire apparatus is enclosed in PDMS, there is no contact between the cells and air.

Glass syringe with sufficient volume for 30-day duration with 1.44cc/day flow rate was mounted on a syringe pump for each experiment. Glass apparatus is leveled to the same altitude with the syringe pump and collection vial to eliminate the pressure difference. A schematic of the experimental setup is shown as Figure 2.4a, and 2.4b is an image of experimental setup at work. All connectors, fittings, tubing are stainless steel. Another stainless-steel tubing is attached to the lid of the collection vial for pressure relief.

Calibration Curves and Concentration Measurement

Ultraviolet absorption spectroscopy is used to measure the concentration of the Trifluorotoluene (TFT) chemical tracer. TFT has a benzene ring corresponding to a UV absorption peak at 255 nm wavelength. The concentration of the SiO_2 and Fe_3O_4 cored nanoparticle tracers are measured by fluorescence spectroscopy of the particle coatings. Both of these particles have the same excitation and emission peaks with higher peak intensity for the Fe_3O_4 cored nanoparticles.

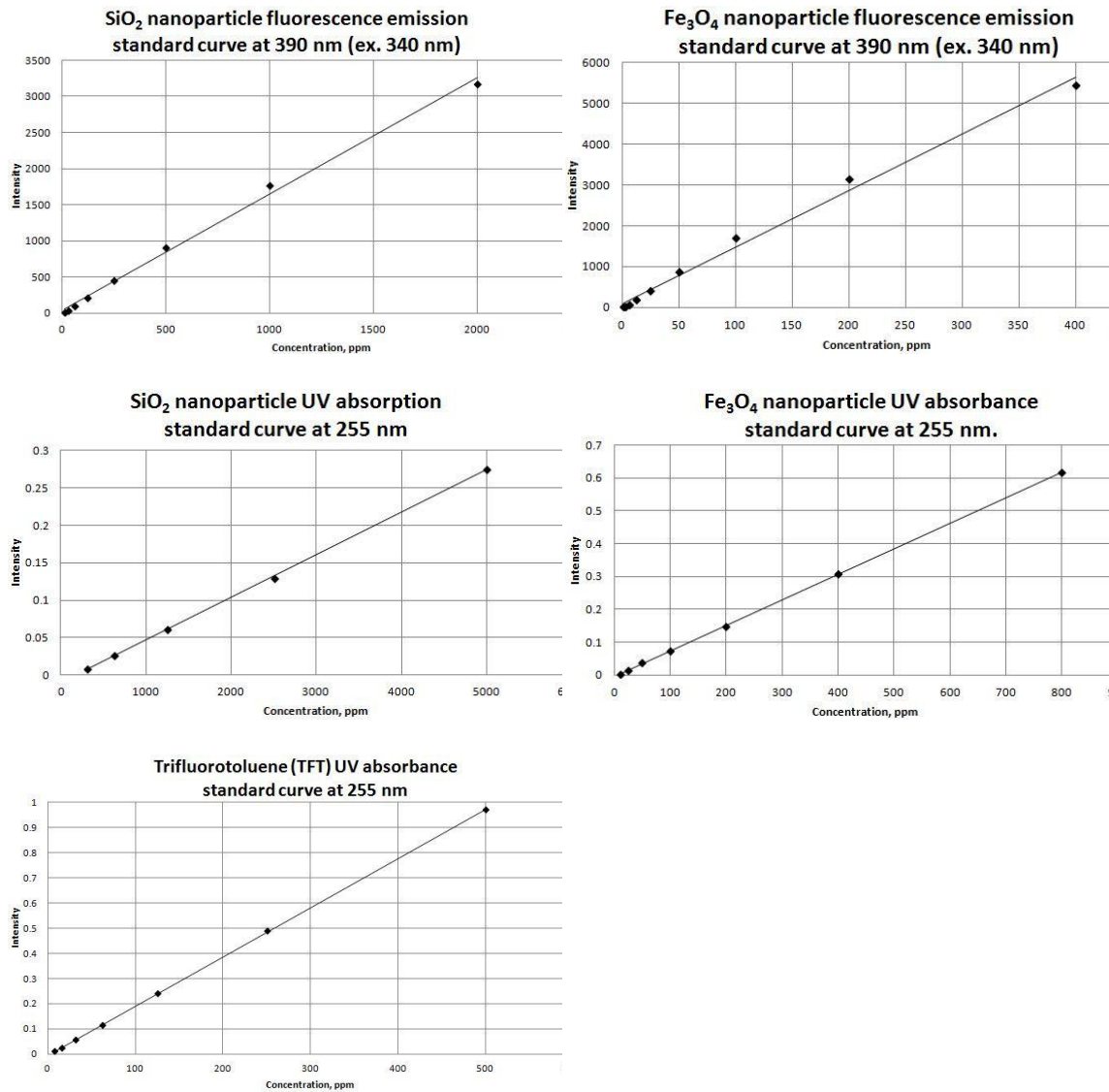
The ultraviolet absorption and fluorescent profile from our carrier solvent HFE is treated as background and subtracted from every tracer measurement. Measurement data of 5 premixed solvents with known concentration of chemical tracer TFT and nanoparticle tracers after 10 seconds of sonication mixing and 24 hours are being compared to their calibration curves in HFE to ensure no interaction between all the components involved under ambient conditions. Ultraviolet absorption calibration curves were calculated for chemical tracer TFT, and both ultraviolet absorption and fluorescent calibration curves were calculated for our nanoparticle tracers because TFT is not fluorescent, and our fluorescent nanoparticle tracers also have small ultraviolet absorption/scattering profile. The detection limit of TFT is around 1.5 ppm, and 20 ppm for Fe_3O_4 and SiO_2 cored nanoparticle tracer. Ultraviolet absorption/scattering profile of our nanoparticle tracers after 300 nm wavelength can be used to determine the concentration, but the detection limit is much higher comparing to measuring their fluorescence.

Data are collected at time intervals that yield the minimal sample size required for analysis. To minimize the evaporation during the measurements, the fluid sample is

withdrawn from the sample collection vial with a glass syringe and quickly injected to a clean glass cuvette with its top sealed. The software program Proview is used to interpret the output of our SpectraMax spectrophotometer from Molecular Devices Company. Glass cuvettes and glass syringes are cleaned thoroughly, dried completely, and reused for the next sample measurement.

The UV absorption intensity of the SiO₂ nanoparticle is calculated using their concentration as determined from their fluorescence using the calibration curve. The UV absorption of the TFT is then the total sample UV absorption minus this UV absorption of the SiO₂ nanoparticles. The concentration of the TFT is then determined from the UV absorption calibration curve. Same method is used to determine concentration of Fe₃O₄ cored nanoparticle tracers. The calibration curve for Fe₃O₄ nanoparticles is linear under 400 ppm, and that of SiO₂ nanoparticles is linear under 5000 ppm. Intensity level below 1% of the injection level is considered insignificant. To achieve an accurate result, the injection concentration for the SiO₂ cored nanoparticle tracer and conservative chemical tracer TFT are 1930 ppm and 436 ppm for experiment 1, and that of the Fe₃O₄ cored nanoparticle tracer and TFT are 334 ppm and 515 ppm for experiment 2. The fluorescence emission calibration curves of the Fe₃O₄ and SiO₂ nanoparticle tracers are shown as figure 2.S3a, 2.S3b; The UV absorption calibration curves of the Fe₃O₄ and SiO₂ nanoparticle tracers are shown as Figure 2.S3c, 2.S3d; The UV absorption calibration curve of the conservative chemical tracer TFT is shown as figure 2.S3e.

Figure 2.S3: a) is SiO_2 nanoparticle fluorescence emission standard curve, the excitation wavelength is 340 nm and the peak emission wavelength is at 390 nm; b) is that of the Fe_3O_4 nanoparticles, the excitation and emission wavelength is the same; c) is SiO_2 nanoparticle UV absorption standard curve at wavelength of 255 nm; d) is that of the Fe_3O_4 nanoparticles; e) is the UV absorption standard curve for conservative chemical tracer trifluorotoluene (TFT) at wavelength 255 nm.



Diffusion Coefficients

Diffusion constants for the solvents, solutes and particles discussed in the body of the ARI report are calculated here using the Stokes Einstein equation. The calculations are summarized in Table 2.S1.

Table 2.S1. Summary of calculated diffusion constants

Solvent	Viscosity	Solute	Radius	$D_o[\text{cm}^2/\text{s}] \times 10^5$
HFE	600 PaS (3M, 2009)	TFT	0.25 nm maximum	1.42
			0.1 nm minimum	3.55
		nanoparticles	40 nm	0.017
scCO ₂	20 μPaS	TFT	0.3 nm maximum	36.4
		nanoparticles	40 nm	0.545
Methane-supercritical CO₂ interdiffusion⁵⁵				88.7

The Stokes-Einstein's Equation

Assumptions: Diffusing entities dispersed or dissolved in a liquid, the entities are spherical, and the Reynolds number is low (no turbulence). Under these circumstances, the diffusion constant of the entities (molecules or particles) can be estimated from equation 2.S1⁴³.

$$D = \frac{KT}{6\pi\mu r} \quad (\text{Eq. 2.S1})$$

where,

K = Boltzmann's Constant (1.38065×10^{-23} J/K)

T = Absolute Temperature in K (297 K)

μ = kinematic viscosity 0.43 cSt

r = radius of the particle

Chemical Tracer - Trifluorotoluene (TFT)

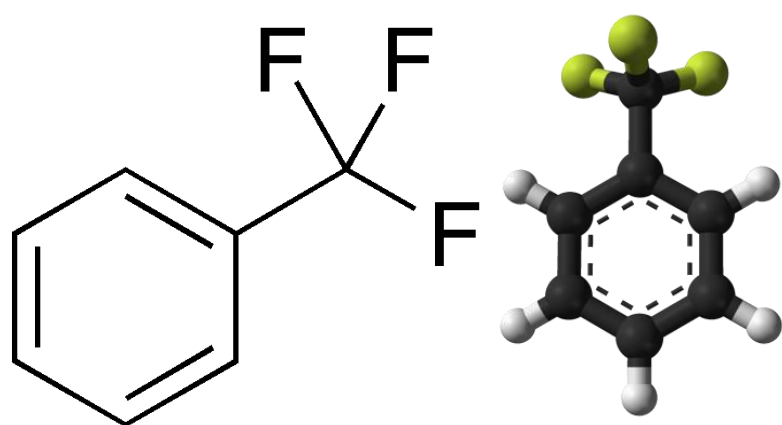


Figure 2.S4. Trifluorotoluene molecule.

The TFT molecule is elliptical. We can estimate the diameter of the major axis of this ellipse from the molecular bond lengths. Adding (1 x H-C bond length) + (3 x C-C bond length) + (1 x C-F bond length) we find a major axis diameter of between 480 and 560 picometers. A radius of 250 pm as gives us $1.42 \times 10^{-9} \text{ m}^2/\text{s}$ or $1.42 \times 10^{-5} \text{ cm}^2/\text{s}$ for TFT in Hydrofluoroether (HFE) in ambient conditions.

The same calculation with the minor molecular ellipse dimension gives a diameter of ~ 200 pm, and this suggests a diffusion constant of $3.55 \times 10^{-9} \text{ m}^2/\text{s}$ or $3.55 \times 10^{-5} \text{ cm}^2/\text{s}$. The best fit diffusion constant for our interpretation of the TFT tracer in HFE is $2.5 \times 10^{-9} \text{ m}^2/\text{s}$ or $2.5 \times 10^{-5} \text{ cm}^2/\text{s}$. Since this diffusion constant lies between these diffusion coefficient estimates for TFT , our best fit model diffusion constant is very reasonable.

To find a value for the viscosity of scCO₂, generally, people refer to 1/10 of that of the water at 20C, or 40% less than that of the liquid CO₂. But it is really a function of temperature pressure.

Using the dynamic viscosity of scCO₂ and assuming scCO₂ carries all fluid diffusional properties near the critical point (304K, 7mPa or 73 atm) of CO₂ 20 $\mu\text{Pa s}^{22}$, the diffusion coefficient based on Stokes-Einstein's equation for molecule with 300 pm radius is $3.64 \times 10^{-8} \text{ m}^2/\text{s}$ or $3.64 \times 10^{-4} \text{ cm}^2/\text{s}$. The viscosity further reduces with the increase in reservoir temperature, however it increases with pressure increase.

Nanoparticle Tracers

(SiO₂ nanoparticle by Yisheng)

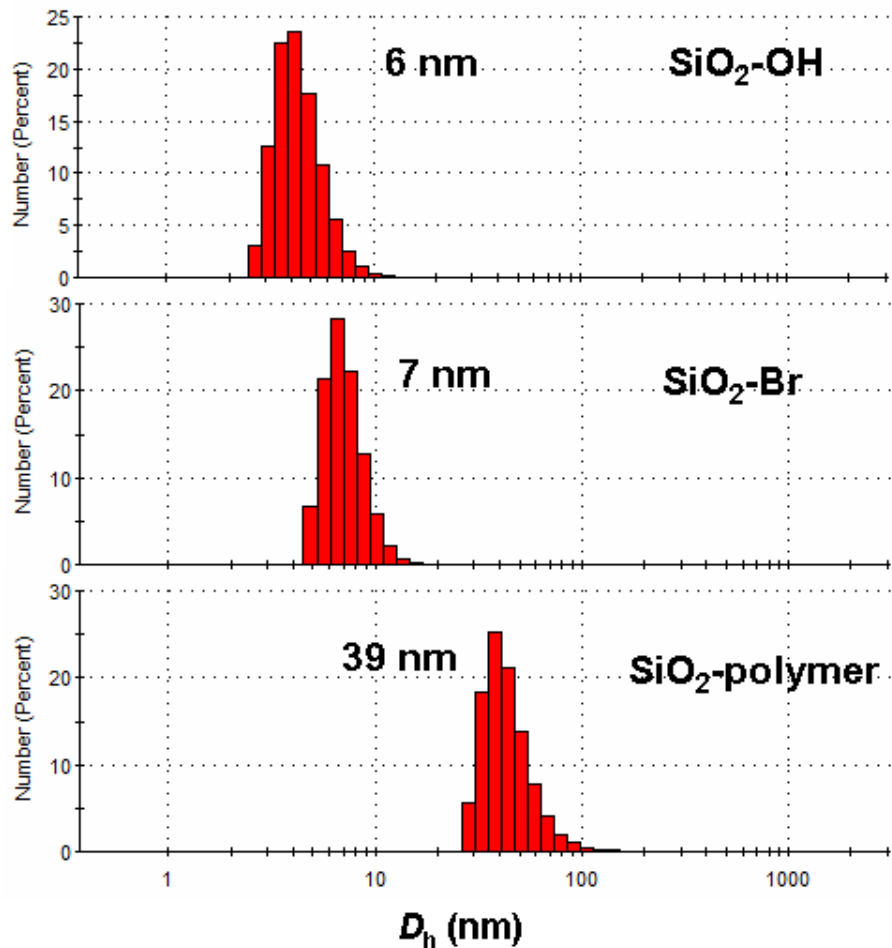


Figure 2.S5. Size distribution of SiO₂ nanoparticle before and after polymerization.

Calculated Diffusion Coefficient based on Stokes-Einstein's equation considering a solid elastic sphere with 19.5 nanometer as radius gives us $1.82 \times 10^{-11} \text{ m}^2/\text{s}$ or $1.82 \times 10^{-7} \text{ cm}^2/\text{s}$ for this kind of SiO₂ nanoparticle in Hydrofluoroether (HFE) in ambient conditions.

Using the dynamic viscosity of scCO₂ and assuming scCO₂ carries all fluid diffusional properties near the critical point (304K, 7mPa or 73 atm) of CO₂ ($20 \mu\text{Pa s} \sim 0.00002 \text{ P}$) and assuming uniformity in sizes, the diffusion coefficient based on Stokes-Einstein's equation for molecule with 19.5 nm radius is $5.6 \times 10^{-10} \text{ m}^2/\text{s}$ or $5.6 \times 10^{-6} \text{ cm}^2/\text{s}$.

(Fe_3O_4 nanoparticle by Yisheng)

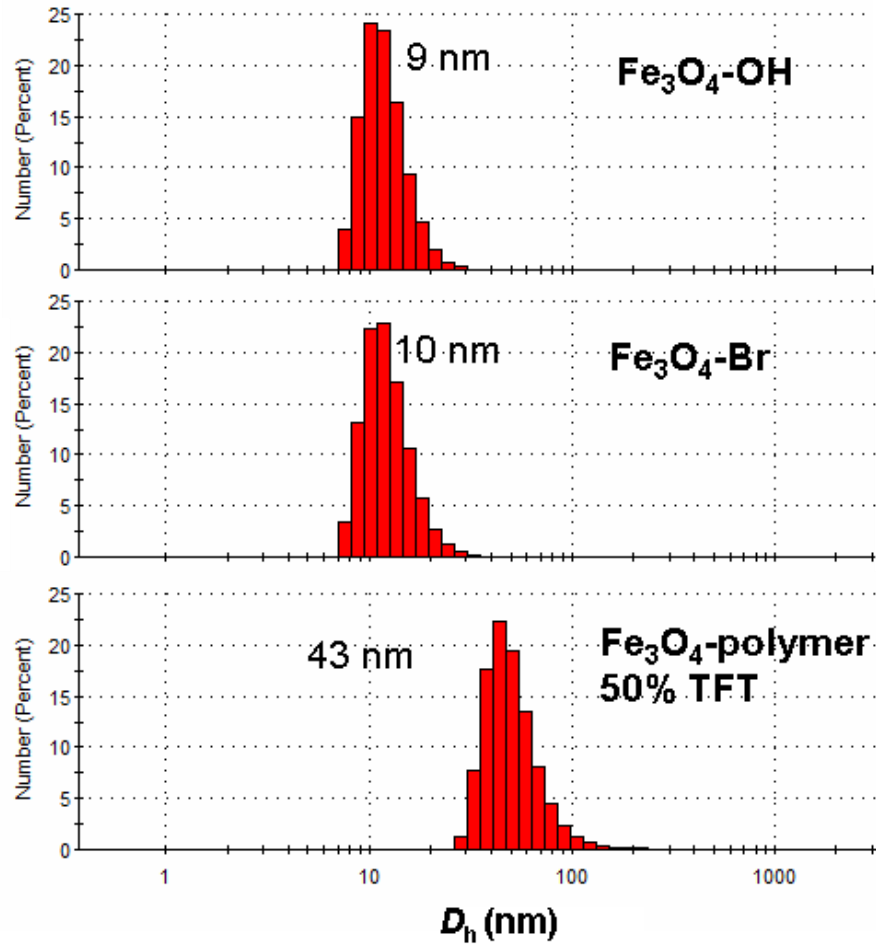


Figure 2.S6. Size distribution for the Fe_3O_4 nanoparticle before and after polymerization.

Calculated Diffusion Coefficient based on Stokes-Einstein's equation considering a solid elastic sphere with a radius of 21.5 nanometers gives $1.65 \times 10^{-11} \text{ m}^2/\text{s}$ or $1.65 \times 10^{-7} \text{ cm}^2/\text{s}$ for this kind of Fe_3O_4 nanoparticle in Hydrofluoroether (HFE) in ambient conditions.

Using the dynamic viscosity of scCO₂ and assuming scCO₂ carries all fluid diffusional properties near the critical point (304K, 7mPa or 73 atm) of CO₂ ($20 \mu\text{Pa s} \sim 0.00002 \text{ Pa s}$) and assuming uniformity in sizes, the diffusion coefficient based on Stokes-Einstein's equation for molecule with 21.5 nm radius is $5.08 \times 10^{-10} \text{ m}^2/\text{s}$ or $5.08 \times 10^{-6} \text{ cm}^2/\text{s}$.

Table 2.S2. Diffusion constants in scCO₂ for spherical particles of different diameter.

Diameter (nm)	Diffusion Coefficient (cm ² /s)
0.1	2.18E-03
1	2.18E-04
10	2.18E-05
20	1.09E-05
30	7.27E-06
40	5.45E-06
50	4.36E-06
100	2.18E-06
200	1.09E-06
300	7.27E-07
400	5.45E-07
500	4.36E-07
1000	2.18E-07

Estimation of Interdiffusion Coefficient of scCO₂ and Methane

CO₂ has a critical temperature of 304.25 K and critical pressure of 72.9 atm/7.39MPa.

At supercritical phase, it tries to expand to fill its container like a gas but with a density like that of a liquid.

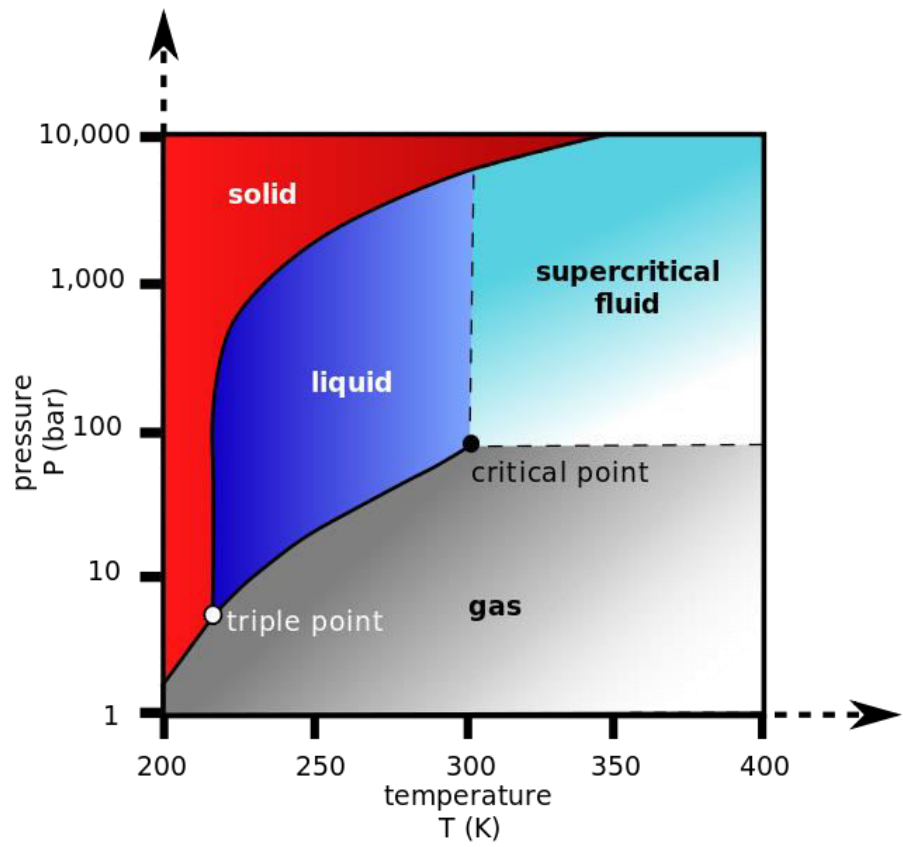


Figure 2.S7. Carbon dioxide pressure-temperature phase diagram (Carbon Dioxide).
http://commons.wikimedia.org/wiki/File:Carbon_dioxide_pressure-temperature_phase_diagram.svg

There are several ways to estimate the interdiffusion coefficient of scCO₂ and methane, namely Stokes-Einstein-based correlations, Dymond free-volume type expression, Catchpole-King correlation, and Tracer Liu-Silva-Macedo Equation. Here used Stokes-Einstein based correlations⁵⁵ estimation method because it is thought to be a better estimation of diffusion coefficients for scCO₂.

$$D_{12} = 7.4 * 10^{-8} \frac{(\phi M_1)^{1/2} T}{\eta_1 V_{2,eb}^{0.6}}$$

1: solvent (CO₂)

2: solute (CH₄)

ϕ : association factor for M₁, for unassociated CO₂ its 1

eb: normal boiling point

M: molecular weight

T: temperature in K

η : viscosity in cP

V: molar volume in cm³/mol

The estimation based on the above equation yields 8.87 x 10⁻⁴ cm²/s

Reynolds number

D_∞ is calculated based on Stoke-Einstein's equation under laminar flow conditions
(low Reynolds number)

$$D_\infty = \frac{k_B T}{3\pi\eta d}$$

Where k_B is Boltzmann's Constant, T is temperature in Kelvin, η is dynamic viscosity of the solvent, d is the particle diameter. The Reynolds number in our experiments indicates the flow is laminar.

$$Re = \frac{\rho v D_H}{\eta}, D_H = \frac{4A}{P} \text{ (For square pipe)}$$

Where ρ is density of solvent, v is the flow velocity, η is the dynamic viscosity of the solvent, D_H is the hydraulic diameter of the pipe, A is the cross section area, and P is the perimeter of the wetted channel walls. The Reynolds number for apparatus 1 is 0.0048, and 0.00323 for apparatus 2, which ensures us we are in the laminar flow regime, and using Stoke-Einstein equation to estimate diffusion coefficient is valid.

References

1. Al-Bazali, T. M., Zhang, J., Chenevert, M. E., & Sharma, M. M. (2005, January 1). Measurement of the Sealing Capacity of Shale Caprocks. Society of Petroleum Engineers. doi:10.2118/96100-MS
2. Anderson, J. R., Chiu, D. T., Wu, H., Schueller, O. J., & Whitesides, G. M. (2000). Fabrication of microfluidic systems in poly (dimethylsiloxane). *Electrophoresis*, 21, 27-40.
3. Bachu, S., Gunter, W. D., & Perkins, E. H. (1994). Aquifer disposal of CO₂: Hydrodynamic and mineral trapping. *Energy Conversion and Management*, 35(4), 269-279.
4. Bachu, S. (2000). Sequestration of CO₂ in geological media: criteria and approach for site selection in response to climate change. *Energy conversion and Management*, 41(9), 953-970.
5. Baker, S. N., & Baker, G. A. (2010). Luminescent carbon nanodots: emergent nanolights. *Angewandte Chemie International Edition*, 49(38), 6726-6744.
6. Beckman, E. J. (2004). Supercritical and near-critical CO₂ in green chemical synthesis and processing. *The Journal of Supercritical Fluids*, 28(2), 121-191.
7. Benson, S., Cook, P., Anderson, J., Bachu, S., Nimir, H. B., Basu, B., ... & Zhou, D. (2005). Underground geological storage. *IPCC Special Report on carbon dioxide capture and storage*, 195-276.

8. Bradshaw, J., Bachu, S., Bonijoly, D., Burruss, R., Holloway, S., Christensen, N. P., & Mathiassen, O. M. (2007). CO₂ storage capacity estimation: Issues and development of standards. *International Journal of Greenhouse Gas Control*, 1(1), 62-68.
9. Brennan S. T., Burruss, R. C., Merrill, M. D., Freeman, P. A., & Ruppert, L. F. (2010). *A probabilistic assessment methodology for the evaluation of geologic carbon dioxide storage*. US Department of the Interior, US Geological Survey.
10. Van der Burgt, M. J., Cantle, J., & Boutkan, V. K. (1992). Carbon dioxide disposal from coal-based IGCC's in depleted gas fields. *Energy Conversion and Management*, 33(5), 603-610.
11. Busch, A., Alles, S., Gensterblum, Y., Prinz, D., Dewhurst, D. N., Raven, M. D., ... & Krooss, B. M. (2008). Carbon dioxide storage potential of shales. *International Journal of Greenhouse Gas Control*, 2(3), 297-308.
12. Cao, L., Wang, X., Meziani, M. J., Lu, F., Wang, H., Luo, P. G., ... & Sun, Y. P. (2007). Carbon dots for multiphoton bioimaging. *Journal of the American Chemical Society*, 129(37), 11318-11319.
13. Cathles, L. M., & Adams, J. J. (2005). Fluid flow and petroleum and mineral resources in the upper (< 20 km) continental crust. *Economic Geology 100th Anniversary Volume*, 77-110.

14. Chiquet, P., Broseta, D. F., & Thibeau, S. (2005, January). Capillary alteration of shaly caprocks by carbon dioxide. In *SPE Europec/EAGE Annual Conference*. Society of Petroleum Engineers.
15. Clemens, T., & Wit, K. (2002, January 1). CO₂ Enhanced Gas Recovery Studied for an Example Gas Reservoir. Society of Petroleum Engineers. doi:10.2118/77348-MS
16. Crist, J. T., McCarthy, J. F., Zevi, Y., Baveye, P., Throop, J. A., & Steenhuis, T. S. (2004). Pore-scale visualization of colloid transport and retention in partly saturated porous media. *Vadose Zone Journal*, 3(2), 444-450.
17. Crist, J. T., Zevi, Y., McCarthy, J. F., Throop, J. A., & Steenhuis, T. S. (2005). Transport and retention mechanisms of colloids in partially saturated porous media. *Vadose Zone Journal*, 4(1), 184-195.
18. Duffy, D. C., McDonald, J. C., Schueller, O. J., & Whitesides, G. M. (1998). Rapid prototyping of microfluidic systems in poly (dimethylsiloxane). *Analytical chemistry*, 70(23), 4974-4984.
19. Engelder, T., Slingerland, R., Arthur, M., Lash, G., Kohl, D., & Gold, D. P. (2011). An introduction to structures and stratigraphy in the proximal portion of the Middle Devonian Marcellus and Burkett/Geneseo black shales in the Central Appalachian Valley and Ridge. *Field Guides*, 20, 17-44.
20. Engelder, T., Cathles, L. M., & Bryndzia, L. T. (2014). The fate of residual treatment water in gas shale. *Journal of Unconventional Oil and Gas Resources*.

21. Engelder, T., Lash, G. G., & Uzcátegui, R. S. (2009). Joint sets that enhance production from Middle and Upper Devonian gas shales of the Appalachian Basin. *AAPG bulletin*, 93(7), 857-889.
22. Fenghour, A., Wakeham, W. A., & Vesovic, V. (1998). The viscosity of carbon dioxide. *Journal of Physical and Chemical Reference Data*, 27(1), 31-44.
23. Freed, R. L. (1981). Shale mineralogy and burial diagenesis of Frio and Vicksburg Formations in two geopressured wells, McAllen Ranch area, Hidalgo County, Texas.
24. Freund, P., & Ormerod, W. G. (1997). Progress toward storage of carbon dioxide. *Energy Conversion and Management*, 38, S199-S204.
25. Gunter, W. D., Bachu, S., & Benson, S. (2004). The role of hydrogeological and geochemical trapping in sedimentary basins for secure geological storage of carbon dioxide. *Geological Society, London, Special Publications*, 233(1), 129-145.
26. Hildenbrand, A., Schlömer, S., Krooss, B. M., & Littke, R. (2004). Gas breakthrough experiments on pelitic rocks: comparative study with N₂, CO₂ and CH₄. *Geofluids*, 4(1), 61-80.
27. Hitchon, B., Gunter, W. D., Gentzis, T., & Bailey, R. T. (1999). Sedimentary basins and greenhouse gases: a serendipitous association. *Energy Conversion and Management*, 40(8), 825-843.

28. Holloway, S. (1997). An overview of the underground disposal of carbon dioxide. *Energy Conversion and Management*, 38, S193-S198.
29. Intergovernmental Panel on Climate Change. (2008). *IPCC Special Report on Carbon Dioxide Capture and Storage*. Retrieved from <http://www.ipcc-wg3.de/special-reports/.files-images/SRCCS-Chapter5.pdf>
30. Intergovernmental Panel on Climate Change. (2013). *IPCC Climate Change 2013: Technical Summary*. Retrieved from http://www.climatechange2013.org/images/report/WG1AR5_TS_FINAL.pdf
31. Kang, S. M., Fathi, E., Ambrose, R. J., Akkutlu, I. Y., & Sigal, R. F. (2011). Carbon dioxide storage capacity of organic-rich shales. *SPE Journal*, 16(04), 842-855.
32. Kohl, D. (2012). *Sequence Stratigraphy and Depositional Environments of the Shamokin (Union Springs) MBR., Marcellus FM. And Associated Strata in the Middle Appalachian Basin.* (Master Thesis). Retrieved from <https://etda.libraries.psu.edu/paper/14086/>
33. Koide, H., Tazaki, Y., Noguchi, Y., Nakayama, S., Iijima, M., Ito, K., & Shindo, Y. (1992). Subterranean containment and long-term storage of carbon dioxide in unused aquifers and in depleted natural gas reservoirs. *Energy Conversion and Management*, 33(5), 619-626.
34. Kuuskraa, V. A., Sedwick, K., & Yost, A. B. (1985). Technically Recoverable Devonian Shale Gas in Ohio, West Virginia, and Kentucky. *paper*.

35. Lash, G. G., & Engelder, T. (2005). An analysis of horizontal microcracking during catagenesis: Example from the Catskill delta complex. *AAPG bulletin*, 89(11), 1433-1449.
36. Lash, G. G., & Engelder, T. (2011). Thickness trends and sequence stratigraphy of the Middle Devonian Marcellus Formation, Appalachian Basin: Implications for Acadian foreland basin evolution. *AAPG Bulletin*, 95(1), 61-103.
37. Lee, J. K., Taylor, P. G., Zakhidov, A. A., Fong, H. H., Hwang, H. S., Chatzichristidi, M., ... & Ober, C. K. (2009). Orthogonal processing: A novel photolithographic patterning method for organic electronics. *Journal of Photopolymer Science and Technology*, 22(5), 565-569.
38. Li, Y. V., Cathles, L. M., & Archer, L. A. (2014). Nanoparticle tracers in calcium carbonate porous media. *Journal of Nanoparticle Research*, 16(8), 1-14.
39. National Energy Technology Laboratory. 2012. *2012 United States Carbon Utilization and Storage Atlas* (Atlas IV).(DOE/NETL-2012).
40. Neuzil, C. E. (1994). How permeable are clays and shales?. *Water resources research*, 30(2), 145-150.
41. Nuttall, B. C., Eble, C. F., Drahovzal, J. A., & Bustin, R. M. (2005). Analysis of Devonian black shales in Kentucky for potential carbon dioxide sequestration and enhanced natural gas production. *Kentucky Geological Survey Report DE-FC26-02NT41442*.

42. Oldenburg, C. M., & Benson, S. M. (2002, January). CO₂ injection for enhanced gas production and carbon sequestration. In *SPE International Petroleum Conference and Exhibition in Mexico*. Society of Petroleum Engineers.
43. Poling, B. E., Prausnitz, J. M., John Paul, O. C., & Reid, R. C. (2001). *The properties of gases and liquids* (Vol. 5). New York: McGraw-Hill.
44. Ray, S. C., Saha, A., Jana, N. R., & Sarkar, R. (2009). Fluorescent carbon nanoparticles: synthesis, characterization, and bioimaging application. *The Journal of Physical Chemistry C*, 113(43), 18546-18551.
45. Sclater, J. G., & Christie, P. (1980). Continental stretching: An explanation of the post-Mid-Cretaceous subsidence of the central North Sea Basin. *Journal of Geophysical Research: Solid Earth (1978–2012)*, 85(B7), 3711-3739.
46. Shosa, J. D., & Cathles, L. M. (2001). Experimental investigation of capillary blockage of two-phase flow in layered porous media. In *Petroleum Systems of Deep-Water Basins: Global and Gulf of Mexico Experience: Proceedings of the GCSSEPM Foundation, 21st Annual Bob F. Perkins Research Conference* (pp. 725-739).
47. Soeder, D. J. (1986). *Porosity and permeability of eastern Devonian gas shale*. Institute of gas technology.
48. Stow, D. A. (1981). Fine-grained sediments: terminology. *Quarterly Journal of Engineering Geology and Hydrogeology*, 14(4), 243-244.

49. Subramanian, S. K., Li, Y., & Cathles, L. M. (2013). Assessing preferential flow by simultaneously injecting nanoparticle and chemical tracers. *Water Resources Research*, 49(1), 29-42.
50. Sun, Y. P., Wang, X., Lu, F., Cao, L., Meziani, M. J., Luo, P. G., ... & Veca, L. M. (2008). Doped carbon nanoparticles as a new platform for highly photoluminescent dots. *The Journal of Physical Chemistry C*, 112(47), 18295-18298.
51. Sundararajan, N., Yang, S., Ogino, K., Valiyaveettil, S., Wang, J., Zhou, X., ... & Allen, R. D. (2000). Supercritical CO₂ processing for submicron imaging of fluoropolymers. *Chemistry of materials*, 12(1), 41-48.
52. Tóth, J. (1962). A theory of groundwater motion in small drainage basins in central Alberta, Canada. *Journal of Geophysical Research*, 67(11), 4375-4388.
53. Vega, B., & Kovscek, A. R. (2010). Carbon Dioxide (CO₂) Sequestration in Oil and Gas Reservoirs and Use for Enhanced Oil Recovery (EOR). *Developments and Innovation in Carbon Dioxide (CO₂) Capture and Storage Technology (Ed. MM Maroto-Valer)*, Woodhead Publishing, Oxford, 104-126.
54. Vine, J. D., & Tourtelot, E. B. (1970). Geochemistry of black shale deposits; a summary report. *Economic Geology*, 65(3), 253-272.
55. Wilke, C. R., & Chang, P. (1955). Correlation of diffusion coefficients in dilute solutions. *AIChE Journal*, 1(2), 264-270.

56. Xu, Y., Chen, L., Zhao, Y., Cathles, L. M., Ober, C. K. (in review) Supercritical CO₂-philic Nanoparticles: A Prospective Tracer for Subsurface Mapping Technologies
57. Yang, S. T., Wang, X., Wang, H., Lu, F., Luo, P. G., Cao, L., ... & Sun, Y. P. (2009). Carbon dots as nontoxic and high-performance fluorescence imaging agents. *The Journal of Physical Chemistry C*, 113(42), 18110-18114.
58. Yang, S. T., Cao, L., Luo, P. G., Lu, F., Wang, X., Wang, H., ... & Sun, Y. P. (2009). Carbon dots for optical imaging in vivo. *Journal of the American Chemical Society*, 131(32), 11308-11309.
59. Zevi, Y., Dathe, A., McCarthy, J. F., Richards, B. K., & Steenhuis, T. S. (2005). Distribution of colloid particles onto interfaces in partially saturated sand. *Environmental science & technology*, 39(18), 7055-7064.

CHAPTER 3

NANOPARTICLE METHODS FOR MEASURING REMEDIATION OF FLOW HETEROGENEITY IN LABORATORY COLUMNS

Abstract:

Engineering uniform subsurface fluid flow is important in many applications. Gels, foams, and polymers are some of the current ways to reduce flow heterogeneity. Laboratory methods are important because they allow testing ahead of vastly more expensive and more difficult-to-interpret field experiments. This paper shows how nanoparticle tracers can be used in laboratory columns of optimal design to measure the remediation of flow heterogeneity. Three sets of experiments (varying permeability contrast, core diameter, and injection rate) determine the optimum column design and operation. The efficacy of deploying Micron-sized Polyacrylamide Elastic Microspheres (MPEMs) for flow remediation is then determined as an example. This paper shows that carefully designed column experiments can screen the effectiveness of flow-modifying additives using an inert nanoparticle tracer. Chapter 4 evaluates the flow remediation of an MPEM additive in detail.

Introduction

Engineering uniform subsurface fluid flow is important in many applications. For example, if carbon dioxide is to be sequestered in a geological formation, storage will be maximized if its introduction fills the porosity as uniformly as possible. Making flow more uniform could result in better geothermal energy extraction. Reducing flow heterogeneity through oil bearing reservoir rocks could increase the effectiveness of water flooding. Gels, foams, and polymers are some of the current ways to reduce flow heterogeneity. Laboratory methods are important in developing flow control methods because they allow testing ahead of vastly more expensive and more difficult-to-interpret field experiments. Laboratory experiments are an important bridge to field evaluations.

The purpose of this paper is to show how nanoparticle tracers can be used in laboratory columns to evaluate flow heterogeneity. Our motivation is the evaluation of the flow homogenization capabilities of micron-sized polyacrylamide elastic microspheres or MPEMs^{10,11,15,34}. The deformable microspheres purportedly retard flow where the flow velocity is greatest and thus make the flow more homogeneous. So far the MPEMs have been evaluated only in parallel-column experiments (e.g., two different permeability columns connected in parallel^{35,36}). In this configuration cross-flow between permeable and impermeable zones is not addressed. For example, MPEMs diverted from a remediated volume into a previously less accessed volume in the same column might seal the new pathways and their effectiveness might thus be overestimated in the parallel-columns tests. Here we describe how inert (non-sticking) nanoparticles can be used in heterogeneous columns of optimal design and operation

to assess flow homogenization. We demonstrate the advantages of using a particle rather than a chemical tracer, and we determine the optimum core-annulus permeability ratio, core-annulus diameter ratio, and flow rate through the column for assessing changes in flow homogeneity. We give one illustration of the application of the optimized column methods described. A companion paper evaluates the flow homogenizing capabilities of the MPEMs using the methods presented here.

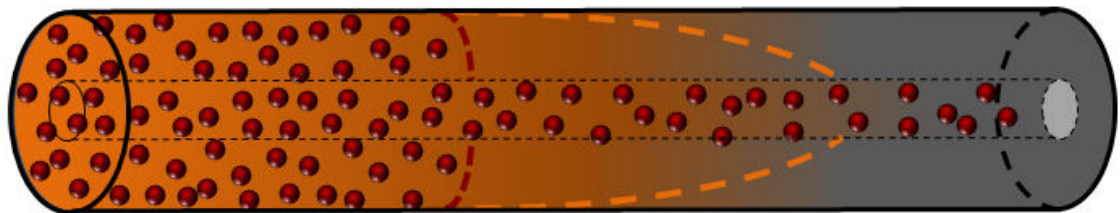


Figure 3.1: Graphical illustration of dual tracer flow behavior in a heterogeneous column. Red sphere represents less diffusive particle tracers and orange shading represents diffusive chemical tracers.

The apparatus we use for assessing changes in the uniformity of fluid flow using a nanoparticle tracer is illustrated in Figure 3.1. It consists of a permeable core surrounded by a less permeable annulus. Flow will occur through both the core channel and the annulus at a rate proportional to their permeability and at a flux proportional to their cross-sectional area. If a treatment preferentially reduces the core permeability, the flow throughput will be reduced in the core and increased in the annulus, and this will be reflected in changes in a tracer arrival curve. Tracer diffusion from the core into the annulus will degrade the signal, and this is the reason that there is an advantage to use nanoparticle tracers which have a much smaller aqueous diffusion constant than chemical tracer alternatives.

Heterogeneous columns of the kind shown in Figure 3.1 will have a distinct “step like” tracer breakthrough curve. For example, if the cross sectional area of the annulus is that same as the cross sectional area of the core but the core is twice as permeable as the annulus, assuming piston flow, tracer traveling through the core will arrive in half the time (or half the pore volumes passed through the column) as tracer moving through the annulus as shown in Figure 3.2. If introducing a flow-altering additive reduces the permeability of the core so that it is only 1.5 times more permeable than the annulus but does not change the permeability of the annulus, the tracer in the core will arrive only 66% sooner than tracer traveling through the annulus. The tracer in the core will arrive later, the tracer from the annulus will arrive sooner, and the annulus concentration step will be bigger (because a greater proportion of the flow is through the annulus), as shown in Figure 3.2. The horizontal contraction in the time between the two “steps” is a result from true velocity of the core and annulus fluid

front becoming more similar, and the vertical shift in the “step” is the result of more fluid passing through the annulus and less through the core.

Figure 3.2 illustrates how flow homogenization can be measured in the laboratory. Of course the flow will not be like a piston, flow will enter the annulus from the core at one end and exit into the core at the other leaving some areas un-swept, there will be diffusion and dispersion of the tracer into the annulus from the core, and the remediating additive is likely to affect flow into the annulus from the core as well as flow in the core. For these reasons interpretation of the tracer measurements will be more complicated than in Figure 3.2, and this figure and its discussion should be taken only as a simplistic illustration of how in principle tracer measurements can assess flow remediation. Also, to compare two column tests, the column and its operation must be the same for both tests. In the remainder of this paper we determine the optimum column design and operating conditions and show that the methods developed can identify quite subtle changes in flow homogeneity.

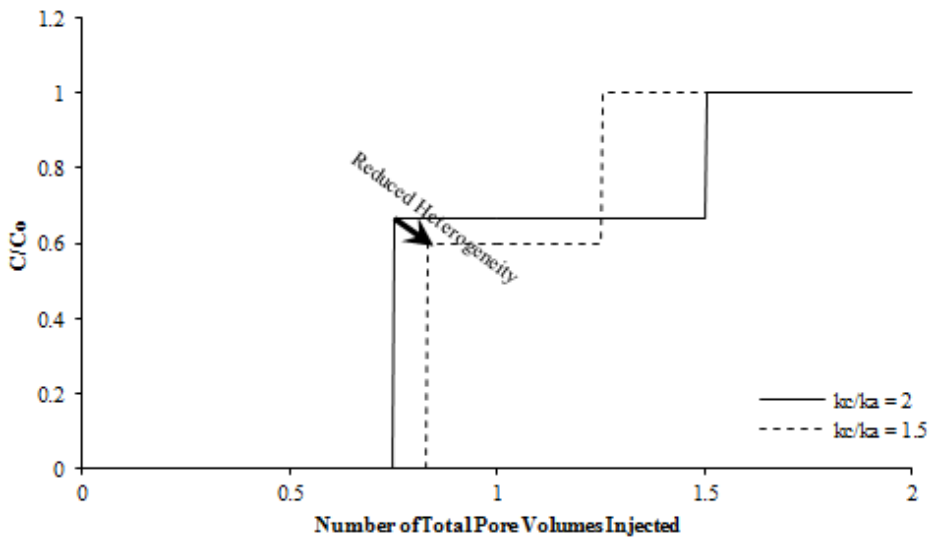


Figure 3.2: Graphical illustration of how the pattern of tracer arrival will change as the permeability of the core is reduced relative the annulus. Here the cross-sectional areas of the core and annulus are the same, the column design is as illustrated in Figure 3.1, and piston flow in the core and annulus is assumed. The tracer concentration in the column effluent is expressed in terms of the total pore volume passed through the column. The change illustrated is that resulting from changing the core permeability from twice to 1.5 times that of the annulus while keeping the annulus permeability the same. Methods of calculation are given in the supplemental material.

Heterogeneous column tests of the type described above have been carried out mainly to assess how much faster pollutants adsorbed onto naturally occurring colloids might be transported through fracture networks^{12,13,18,20,27}. Soil scientists have focused on gravity-driven heterogeneous fingering^{2,31}. Descriptions of the relevant heterogeneous column tests do not usually report tracer tests either because flow conditions are unfavorable or the tracers are not stable^{5,22,29}. In the case most similar to ours, Saiers et al.²⁹ adjusted solution chemistry to assist the suspension of colloidal silica particles and observed a distinct “step like” arrival behavior of the heterogeneous column but the colloidal particle they used adsorbed on sand grains. So far as we know, our group is the only one that has focused on developing inert nanoparticle tracers for measuring fluid bypass (see Subramanian et al.³²). This paper builds on and extends this previous work by our group.

Material and Methods

Column Packing and Design

Proper column packing has long been recognized crucial yet difficult to achieve even for uniform grain size material^{23,24,25,30}. Longitudinal and/or lateral heterogeneities can occur if a column is not packed carefully^{25,26}. We found that even when the best packing protocols are followed, residual air in the columns can lead to non-uniform flow and un-repeatable experimental results, and we have found that the air is difficult to eliminate. Our columns were wet packed following a strict column packing protocol that we developed to eliminate residual air with a medium duty vacuum pump

(Vaccubrand ME1, Germany) during both the packing and sand preparation processes.

This packing protocol is described at length in a Chapter 4.

As shown in Figure 3.3, the experimental column consists of caps and fittings that connect to influent and effluent tubing, copper filters to contain the sand, rubber O-ring seals, a 17.5 cm long 1.95 cm diameter Plexiglass tube, and a variable diameter copper net tube that separates coarse sand in the central core from fine sand in the annulus. The apparatus was constructed by the Cornell University Physics Department machine shop.

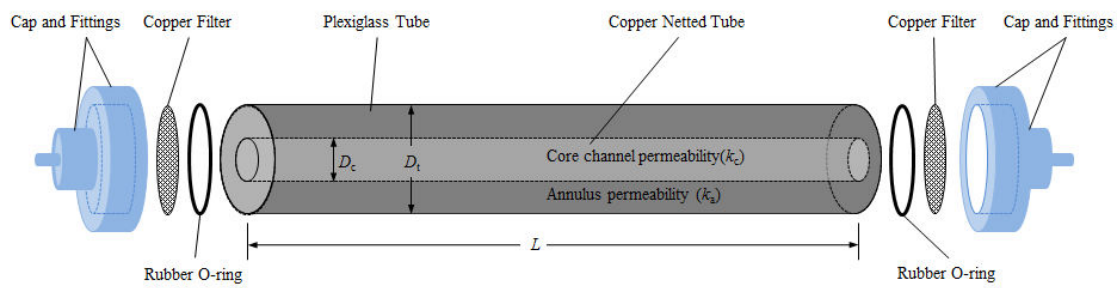


Figure 3.3: Graphically illustration of heterogeneous column, the copper netting is removed when packing the homogeneous columns.

As illustrated in Figure 3.4a, fluid was injected at a constant and precise rate using two 60 mL syringes mounted on a continuous-flow-syringe-pump (780200V, KD Scientific, MA, USA). A peristaltic pump is used to flush the system with a premixed 5000 ppm NaCl solution, and to inject the micron-sized polyacrylamide elastic microspheres (MPEMs). Injection pressure is monitored with a thin vertical tube secured to a tape measure. The effluent is connected to a fraction collector (Foxy R1, Teledyne ISCO, NE, USA) and samples collected at regular intervals and volumes. All components of the system are kept at the same elevation as illustrated in Figure 3.4b.

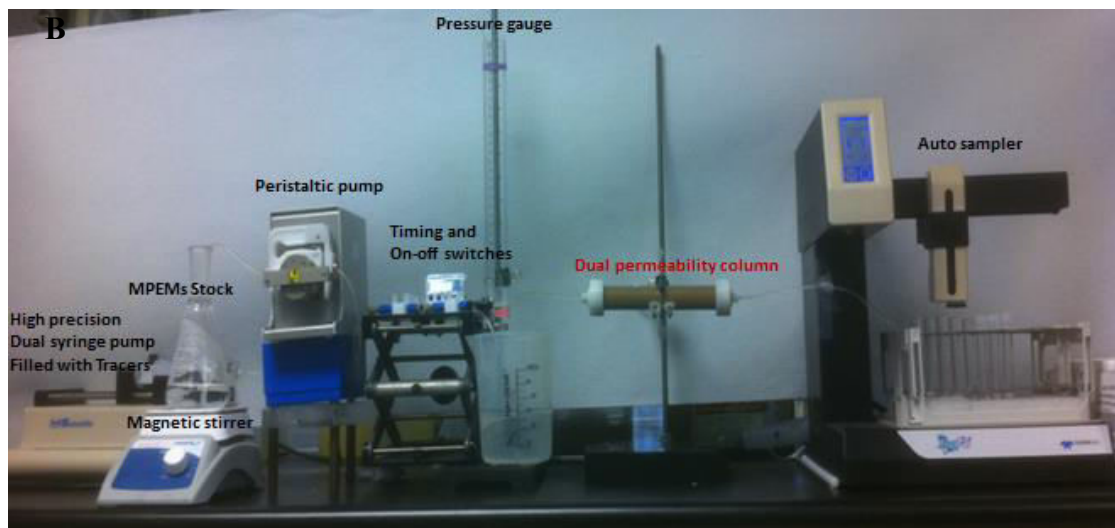
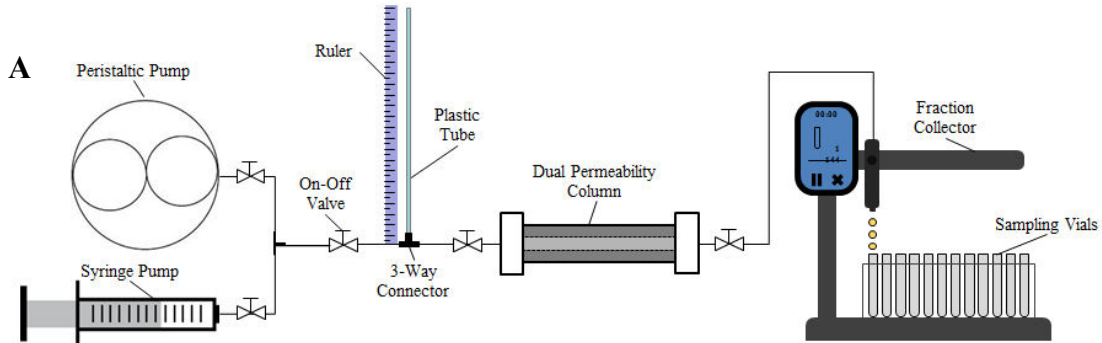


Figure 3.4: (A) Schematic of experimental setup. (B) Picture of the apparatus during operation. A magnetic stirrer in the MPEMs stock solution flask ensures a uniform concentration of MPEMs is injected. When flushing, the MPEMs stock is replaced with brine stock.

Solid Materials and Methods

The quartz sand used in the experiments was purchased from AGSCO Corporation. Its mean grain diameter ranges between 74-250 μm , the grain density is 2.65 g/cm³, and the pH of the DI water used to wash the sand was between 6.8-7.2. The sand is >98% SiO₂, with minor Al₂O₃, K₂O and Fe₂O₃. Sands were sieved, acid washed, rinsed in DI water, oven dried, and then re-saturated in DI water prior to the column experiments.

Four size range sands were prepared in the fashion described above. Their measured and calculated properties are listed in Table 3.1.

Table 3.1: Parameters for four sand types

Sand Type	Mean Grain Diameter (μm)	Sieve Size	Packed Porosity [ϕ] (%)	Permeability* [k] (μm^2)
A	74-106	150-200	0.42	9.91
B	106-125	120-150	0.41	15.17
C	125-177	80-120	0.39	21.05
D	177-250	60-80	0.38	38.33

*: Permeability is calculated with the Kozeny-Carman's equation with specific surface of sand given by^{3,7,8}. Permeabilities calculated by other methods^{4,19} can be up to a factor of 5 smaller, but the permeability ratio between the core and annulus (the important parameter here) remains essentially unchanged.

Tracer Materials and Methods

Br^- was chosen as a conservative chemical tracer because it is small, diffusive, and easily detected at low concentrations. The effluent Br^- concentration was measured with an ion-selective electrode attached to a handheld pH/mV/Temperature meter (6230N, Jenco Instruments, California, USA). Known concentrations of Br^- standard solutions were used to produce calibration curves prior to each set of experiments. The injection concentration of KBr tracer was 1000 ppm. The effective diffusion coefficient of Br^- is the aqueous diffusion coefficient multiplied by the sand column porosity divided by the tortuosity. The aqueous diffusion coefficient of Br^- is $2 \times 10^{-5} \text{ cm}^2/\text{s}$,²¹ and we take the tortuosity of uniformly packed spheres as 1.5^{3,28}, which is appropriate for the measured porosity of our sand packings⁹.

The nanoparticle CDot tracer consists of carbon-cored nanoparticles that are synthesized in a one-step thermal decomposition of citric acid monohydrate and ethanolamine in a 1-3 molar ratio and functionalized with highly hydrophilic polymer coronae hairs^{14,17}. The nanoparticles and their decoration are 2-5 nm in diameter and are inert (non-sticking) under the conditions of our experiments¹⁶.

The concentration of the CDot nanoparticle tracer was determined by the fluorescence of the solution, measured using a spectrofluorimeter (SpectraMax M2e, Molecular Devices, Sunnyvale, CA, USA). The optimum excitation wavelength was 358 nm and the emission peak at this excitation is 460 nm. Known concentration CDot standards were prepared and calibration curves determined prior to each set of experiments. The CDot concentrations of effluent samples were calculated using this calibration curve. CDot concentration is linear below 50 ppm, and the detection limit is ~10 ppb. We

verified that the concentration of particle and chemical tracers could be determined when both were present in the same solution using their independent concentration curves by showing that the CDot tracer calibration curve in DI water is identical to that in a 5000ppm NaCl, 1000ppm KBr solution. The injection concentration of CDot in all our experiments is 50 ppm. The aqueous diffusion coefficient of the CDots, calculated using Stoke-Einstein's Equation, is 1.5×10^{-6} , more than an order of magnitude less than Br⁻.

Experimental Results

Three sets of experiments were carried out to determine the optimum column design and operating conditions for testing remediation of flow heterogeneity. The first set of experiments varied the permeability contrast between the core and annulus by changing sand grain size while keeping everything else the same. The second set of experiments varied the core diameter keeping everything else the same. Only a CDot particle tracer was used in these two sets of experiments which determined the optimum column geometry. The third set of experiments determined the optimum experimental flow rate by varying the flow rate in the column design that was determined to be optimum in the first two sets. The final set of experiments investigates the flow alteration achieved by deploying the MPEMs using optimum column design and operating procedures. Table 3.2 lists the basic parameters of all the column experiments.

Table 3.2: Summary of basic parameters of heterogeneous column models.

Column	Note	D _t	D _c	Φ _c	Φ _a	V _c	V _t	k _c	k _a	V _c /V _t	k _c /k _a	Q
Exp. #	Core / Annulus	(cm)	(cm)	(%)	(%)	(cc)	(cc)	(μm ²)	(μm ²)	(%)	(%)	(cc/min)
1	Sand A / Sand A	1.95	1.04	0.42	0.42	6.24	21.95	9.91	9.91	0.28	1	1
2	Sand B / Sand A	1.95	1.04	0.413	0.42	6.14	21.85	15.17	9.91	0.28	1.53	1
3	Sand C / Sand A	1.95	1.04	0.394	0.42	5.85	21.56	21.05	9.91	0.27	2.12	1
4	Sand D / Sand A	1.95	1.04	0.385	0.42	5.73	21.43	38.33	9.91	0.27	3.87	1
5	Sand A Only	1.95	1.04	0.42	0.42	6.24	21.95	9.91	0	0.28	INF.	1
6	0 D _{Core}	1.95	0	0.385	0.42	0	21.95	38.33	9.91	0	3.87	1
7	Small D _{Core}	1.95	0.5	0.385	0.42	1.32	21.83	38.33	9.91	0.06	3.87	1
8	Medium D _{Core}	1.95	1.04	0.385	0.42	5.73	21.43	38.33	9.91	0.27	3.87	1
9	Large D _{Core}	1.95	1.36	0.385	0.42	9.8	21.07	38.33	9.91	0.46	3.87	1
10	Max D _{Core}	1.95	1.95	0.385	0.42	20.14	20.14	38.33	9.91	1	3.87	1
11	Flowrate I	1.95	1.0	0.385	0.42	5.30	21.47	38.33	9.91	0.25	3.87	0.017
12	Flowrate II	1.95	1.0	0.385	0.42	5.30	21.47	38.33	9.91	0.25	3.87	0.1
13	Flowrate III	1.95	1.0	0.385	0.42	5.30	21.47	38.33	9.91	0.25	3.87	1
14	Flowrate IV	1.95	1.0	0.385	0.42	5.30	21.47	38.33	9.91	0.25	3.87	10
15	Before MPEMs	1.95	1.0	0.385	0.42	5.30	21.47	38.33	9.91	0.25	3.87	0.1
16	After MPEMs	1.95	1.0	0.385	0.42	5.30	21.47	38.33	9.91	0.25	3.87	0.1

* The porosity was determined by measuring the mass difference before and after filling the system. Core and total pore volumes are determined by the dimension of the apparatus and porosities associated with different sized sand under same packing protocol. D_c is the physical diameter, Φ_c the porosity, V_c the volume, and k_c the permeability of the core channel, and similarly for the annulus (subscript a) and total (subscript t). Q is the flow rate in the experiments indicated in the first two columns.

Permeability ratio experiments

In this first set of experiments the permeability was varied by changing the core sand size while keeping the annulus sand size the same as indicated in Tables 3.1 and 3.2.

The last experiment was carried out in a sand-filled glass tube with the same inner diameter as the core channel. In this case the annulus permeability is zero. The flow rate was kept at 1 mL/min, and the core diameter was the same in all experiments.

The set of experiments is graphically illustrated in Figure 3.5. The experimental results are summarized in Figure 3.6.

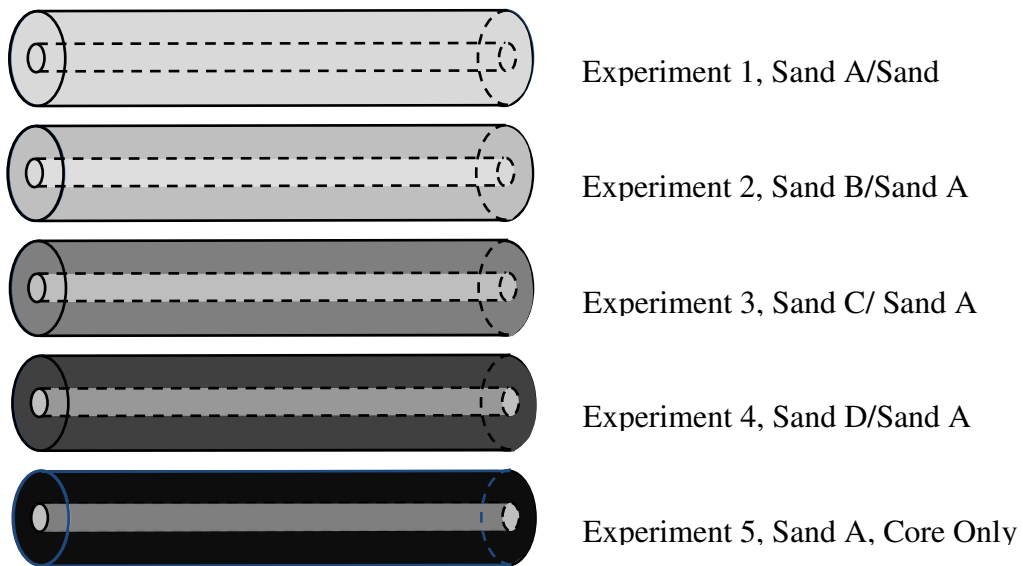


Figure 3.5: Graphical illustration of core-annulus permeability ratio column experiments. Shade indicates permeability (light most permeable). The dimension of the core channel is kept the same for all columns. Sand diameters are given for the sand types in Table 3.1. The annulus is always filled with Sand A.

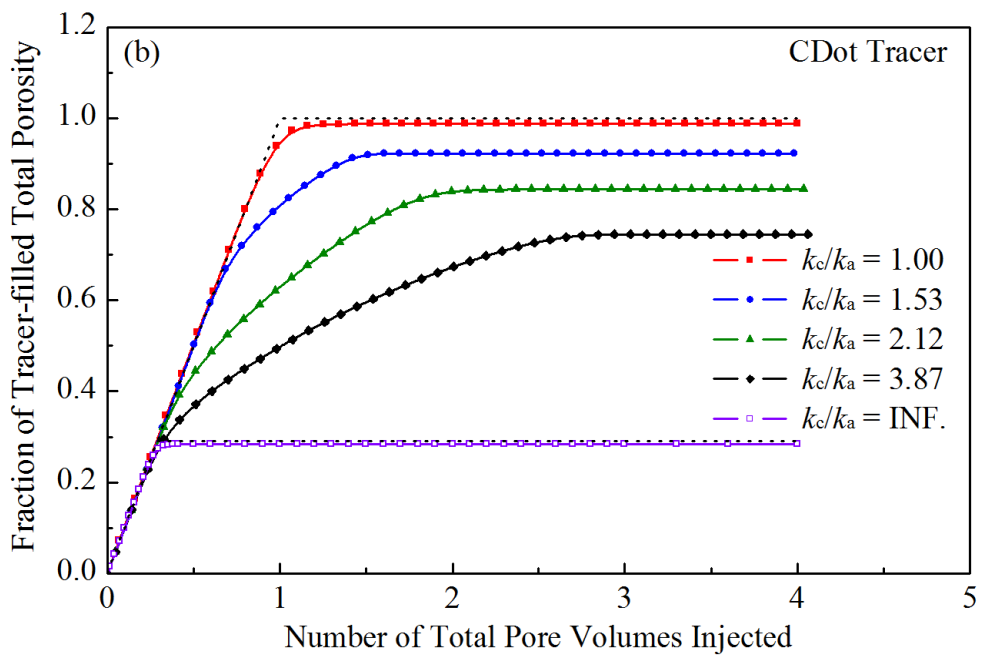
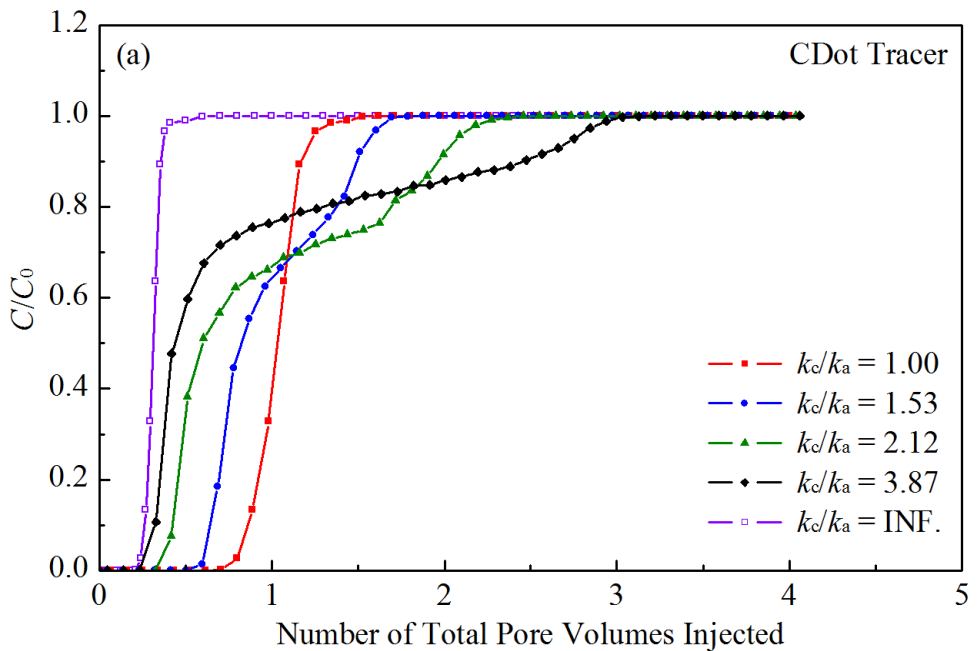


Figure 3.6: (a) Breakthrough curves of the CDot particle tracer for different ratios of core to annulus permeability. (b) Fraction of the column pore space filled with tracer (sweep efficiency) for the same set of experiments.

Figure 3.6a shows that there are two steps in the tracer breakthrough curve when the column is filled with two sands of contrasting permeability. The "step" in the tracer curve becomes more elongated and elevated as the core-annulus permeability ratio increases. This behavior is expected as indicated in Figure 3.2. Figure 3.6b shows how the fraction of the total pore volume that contains particle tracer changes with the injection volume. This fraction is determined by integrating the difference between particle mass that goes in and come out of the column over time. In the case where the annulus is impermeable, tracer is only able to fill the core porosity and once the core porosity is filled no more tracer is stored and the curve is flat (base purple curve in Figure 3.6b). When the column is filled with only one sand (e.g., is homogeneous) the tracer stored in the column rises to the total porosity of the column and then stops (red top curve). For cases where the core and annulus have contrasting permeability, the stored tracer rises to a level less than the total porosity of the column and plateaus. This reflects the fact that flow from the core into and through the annulus does not sweep the entire pore volume of the annulus. Flow avoids the corners at the ends of the column, and this tendency is greatest when the ratio of core to annulus permeability is greatest.

Core radius experiments

The second set of experiments varied the diameter of the core channel, keeping the injection rate at 1 mL/min and the core channel and annulus fill sand types D and A (Table 3.1) respectively. In experiment 6 the entire apparatus was filled with sand type A (74-106 μm sand), and in experiment 10 the entire apparatus was filled with sand type D (177-250 μm sand). In these two cases there is no core channel. Column

parameters are given in Table 3.2. Figure 3.7 graphically illustrates the experiment set, and the experimental results are shown in Figure 3.8.

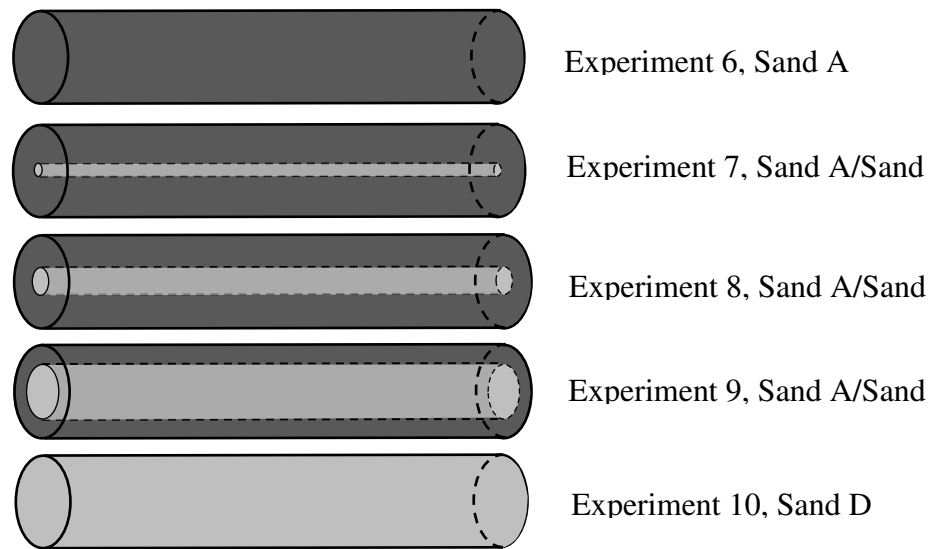


Figure 3.7: Graphical illustration of the flow experiments where core diameter is systematically varied. Lighter shading indicates coarser sand. The core diameters are given in Table 3.2.

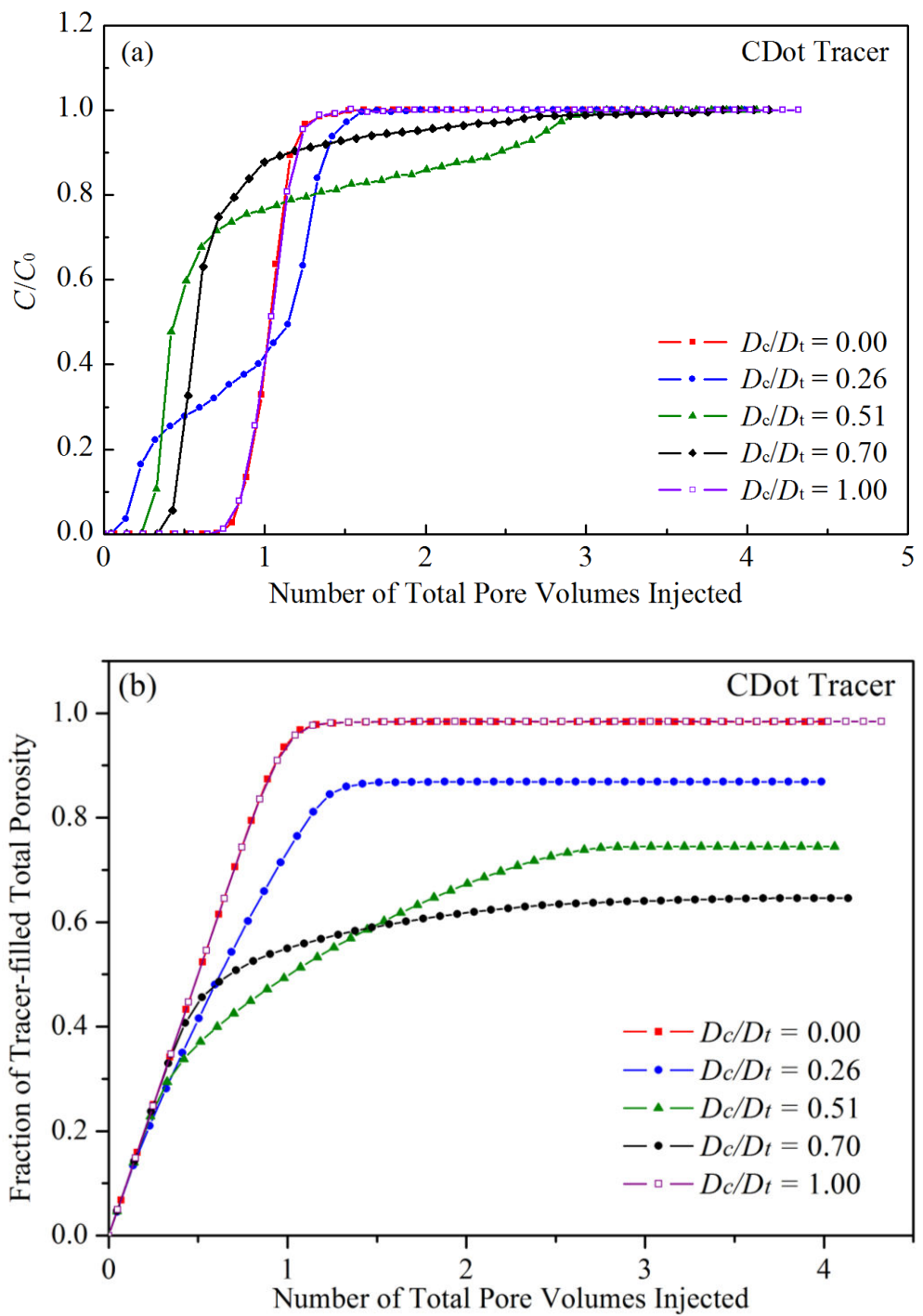


Figure 3.8: (a) Breakthrough curves of the CDot particle tracer for different values of the core/column diameter ratio. (b) Fraction of the column pore space filled with tracer (sweep fraction) for different core/column diameter ratios.

Figure 3.8a shows that increasing core channel diameter delays breakthrough, and elevates and elongates the “step”. This is expected as the system heterogeneity increases from $D_c/D_t = 0$ to 1. In a heterogeneous column the core channel true fluid velocity is highest when the core size is small, and it decreases with increasing core size. True velocity in the annulus also decreases as more fluids is diverted to the core, and becomes very small when the core size is large. The "step" is higher when more of the effluent volume comes from the core channel, as occurs as the core diameter becomes larger. Figure 3.8b shows that the fraction of the total pore volume that contains tracer is least when the core diameter is greatest. There are some curve cross-overs that would be interesting to investigate, but they are not important for column design, and we will not pursue their causes here other than to say they reflect how the annulus is swept by flow from the core channel.

Optimal column design

The two sets of heterogeneous column experiments just described show how flow “dead zones” developed with the introduction of column heterogeneities. Since the “dead zones” are what flow remediation additives would rectify, the optimum column design for testing these additives will be that which maximized the dead zone volume (e.g., has the smallest fraction of tracer-filled total porosity). Figure 3.9a shows that this condition is met when the permeability contrast between the core and annulus is as large as possible (Expt. 4), and Figure 3.9b shows that it is met when the core volume is half that of the column. However, extensive heterogeneity results a dominant single step arrival (Figure 3.8a) where dispersion smears the second step, as a demonstration of double step condition, we picked $V_c/V_t = 0.25$ for the following

flow-rate experiments and the showcase of MPEM evaluation. Extensive study on MPEM flow alteration will be documented in Chapter 4 where a wide range of V_e/V_t is studied.

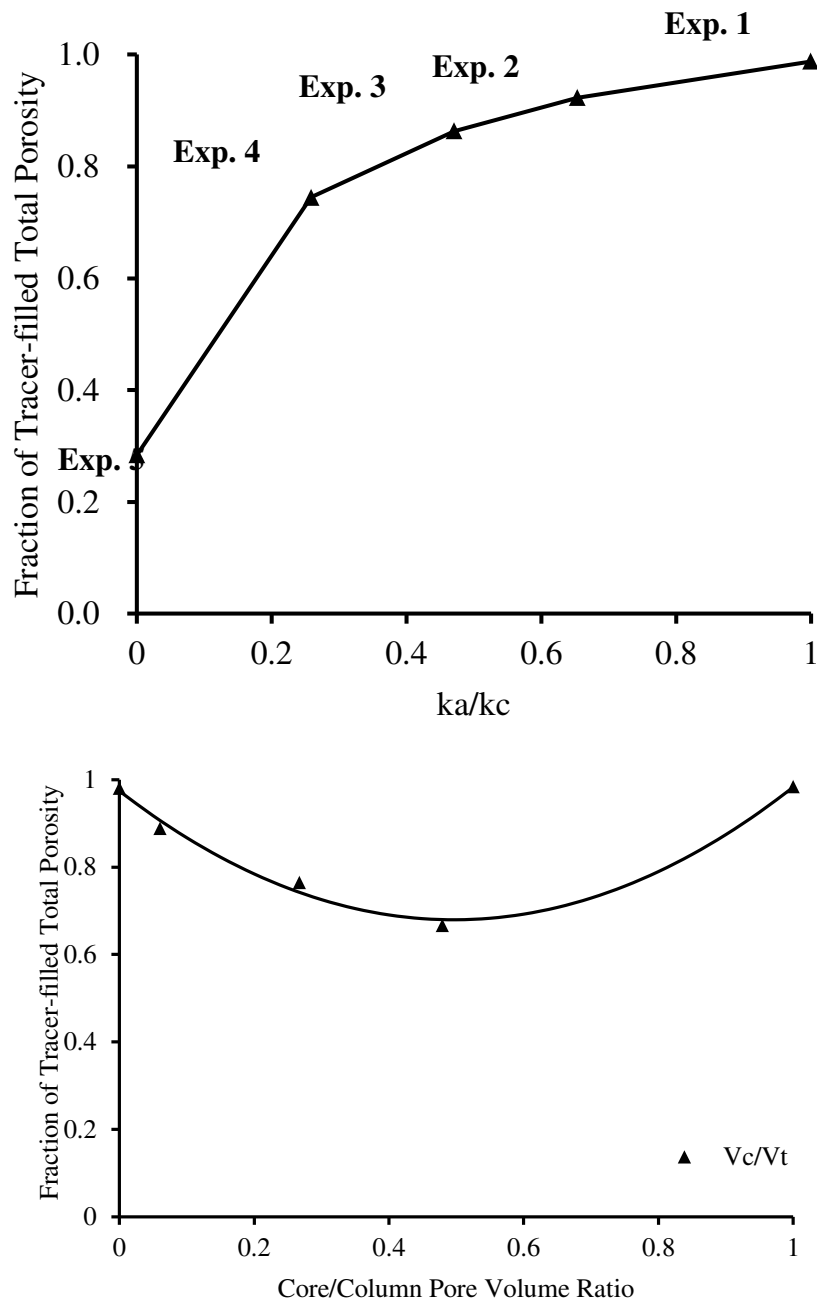


Figure 3.9: (a) Fraction steady state (4 pore volumes injected) tracer-filled total column porosity as a function of the annulus to core permeability ratio (first set of experiments shown in Figure 3.5 & 3.6). (b) The fraction of steady state tracer filled total column porosity as a function of the volume ratio of the core to the column (second set of experiments shown in Figure 3.7 & 3.8). Optimum column design has the maximum core/annulus permeability (a) and core volume half that of the column (b).

Optimizing flow rate

Heterogeneous column flow experiments using the optimum column design determined above were then carried out to determine the optimum column flow rate for detecting changes in the heterogeneity of flow. KBr tracer and CDot tracers were both used in these experiments and these tracers were premixed in known concentrations in the injected fluid. Both were simultaneously injected and their effluent concentrations compared. The core channel was the optimum at 1cm to display a good step arrival, and highest contrast sand fill combination was used. Only 1 column was packed and used for this set of experiments to eliminate any variations due to repacking. The flow rates were 1/60, 0.1, 1, and 10 mL/min. After each experiment the tracers were flushed from the column by passing with 5000ppm NaCl brine for at least 4 times the experimental pore volume through the column. Typically this flush was 16 total column pore volumes. Blank solutions are collected prior to each set of experiment. Experimental results are shown in Figure 3.10, and 3.11.

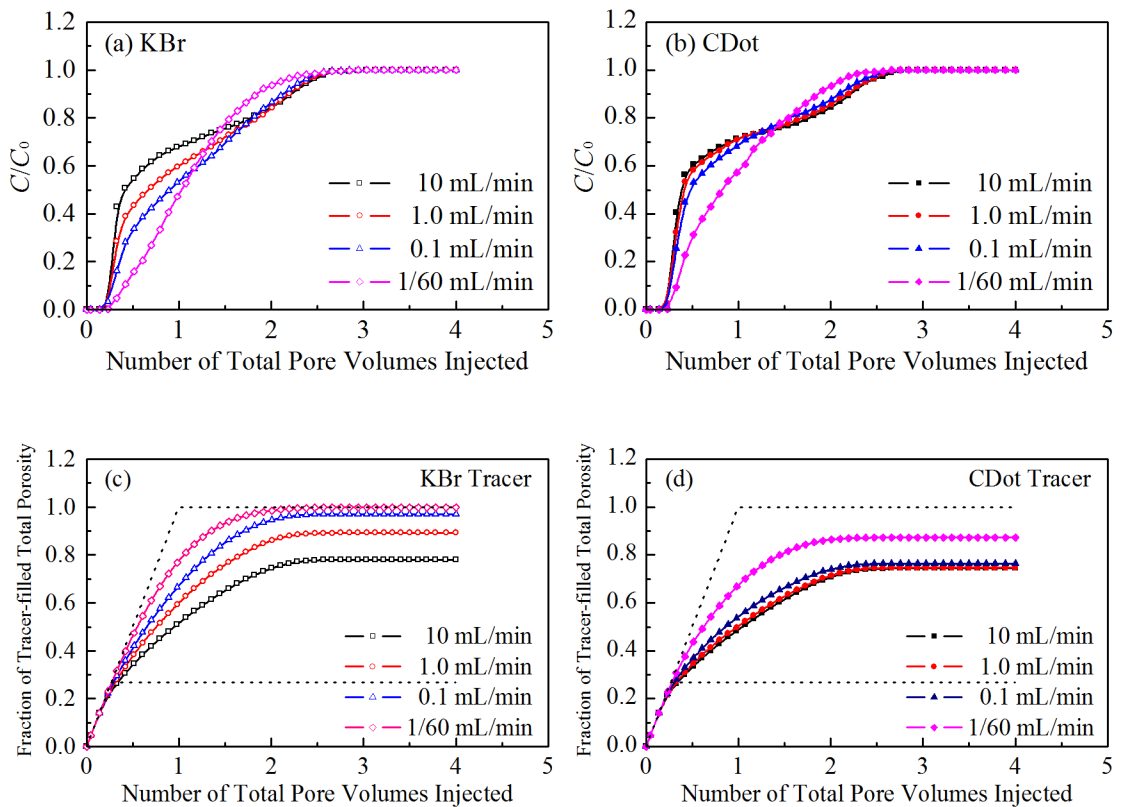


Figure 3.10: KBr and CDot tracer arrival (a and b) and the fraction of the porosity filled with tracer (c and d) for different flow rates through the column plotted as a function of the total pore volumes of tracer injected into the column. The column design was the optimum with core channel diameter of 1 cm, core channel mean grain size at 177-250 μm , annulus mean grain size at 74-106 μm . Details are given in Table 3.2, 11-14.

Figure 3.10 shows that with decreasing injection rate the increased fluid residence time allows more tracers to diffuse into the annulus. For the diffusive Br⁻ tracer the effect is most marked. The effluent arrival curves separate as a function of flow rate (Figure 3.10a), and the fraction of stored tracer increases because it is assisted by diffusional sequestration (Figure 3.10c). Importantly, the impact of diffusion is much less for the particle tracer (Figure 3.10b and d). Curve separation and increases sequestration is significant only for the slowest flow rate. The ratio of advection to diffusion (the inverse Peclet number) provides a good prediction of this phenomenon, as discussed in the supplemental material. Figure 3.11 compares tracer arrival curves at the same flow rate.

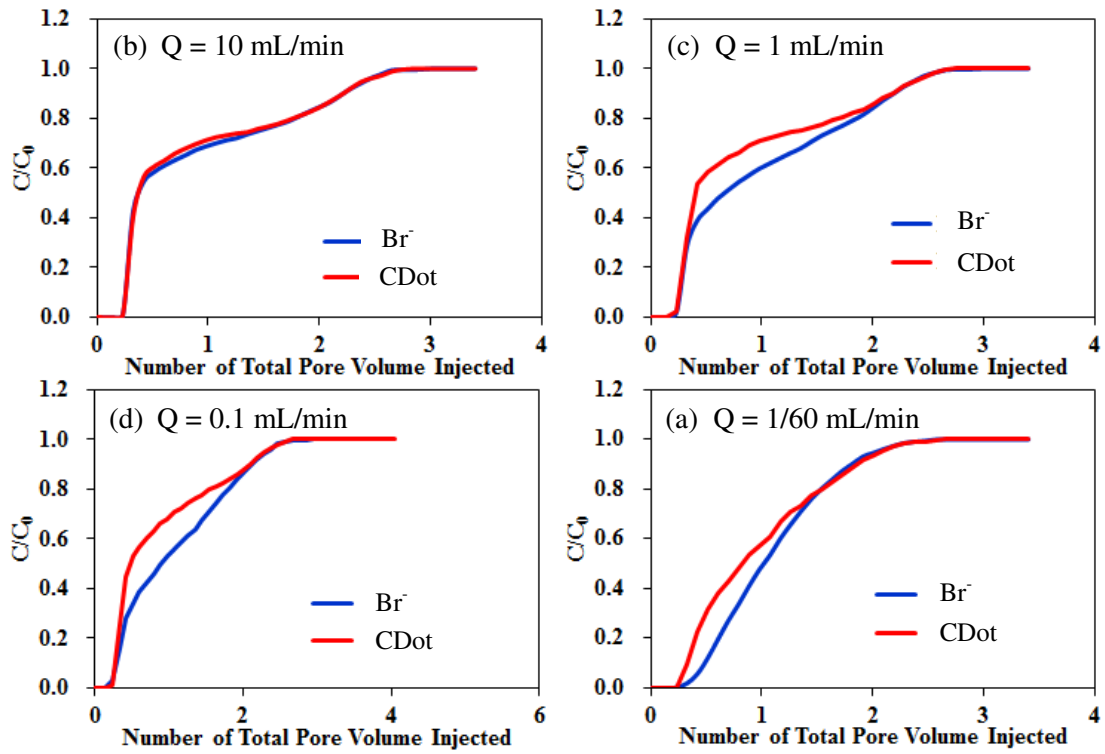


Figure 3.11: (a) is the dual tracer heterogeneous column flow experiment with 10 mL/min injection rate. Red curve is the CDot concentration and blue curve is Br^- concentration. (b), (c), and (d) is that with injection rate of 1, 0.1, and 1/60 mL/min respectively.

Figure 3.11 shows that at very high injection rates the diffusive chemical tracer and non-diffusive particle tracers arrived nearly identical times and concentrations. Neither has time to diffuse from the core into the annulus (N_{iPe} for both is very small, see supplemental material). With decreases in injection rate the ability of the Br⁻ tracer to measure annulus volumes filled by tracer is degraded by diffusion and the Br⁻ and CDot tracer curves in Figure 3.11 diverge. The ability of the CDots to measure tracer “dead zones” is unimpaired until the injection rate is very slow (Figure 3.10b and d). The CDot tracer yields reliable “dead zone” assessments over a broad range in injection rates.

Evaluating flow remediation

Figure 3.12 shows the “dead zone” changes produced when different concentrations of flow-remediating deformable microspheres (MPEMs) are injected into the optimally designed column at 0.1 mL/min. We want to use the lowest flow rate because with high flow rates, MPEMs are subjected to further migration, we want to make sure the evaluation process itself does not change the profile modification done by MPEMs in anyway. As MPEMs are added, the CDot tracer curve is clearly shifted in a direction that indicated the permeability of the core channel has been reduced relative to the annulus. Low amounts of MPEM injection suffice. There is not much difference in flow remediation between injecting 30 or 60 mL of MPEMs at concentration of 0.2% by weight in suspension. Easier to see is the clear increase in the fraction of tracer-filled porosity when the MPEMs are injected (Figure 3.12b). The changes are small. Hence the attention given here to column packing, design, and operating conditions. Subtle laboratory flow changes do not necessarily indicate that the flow in field

applications will be small. The important point for this paper is that carefully designed column experiments can screen the effectiveness of flow-modifying additives. Chapter 4 evaluates the effectiveness of MPEMs in flow remediation in much more detail.

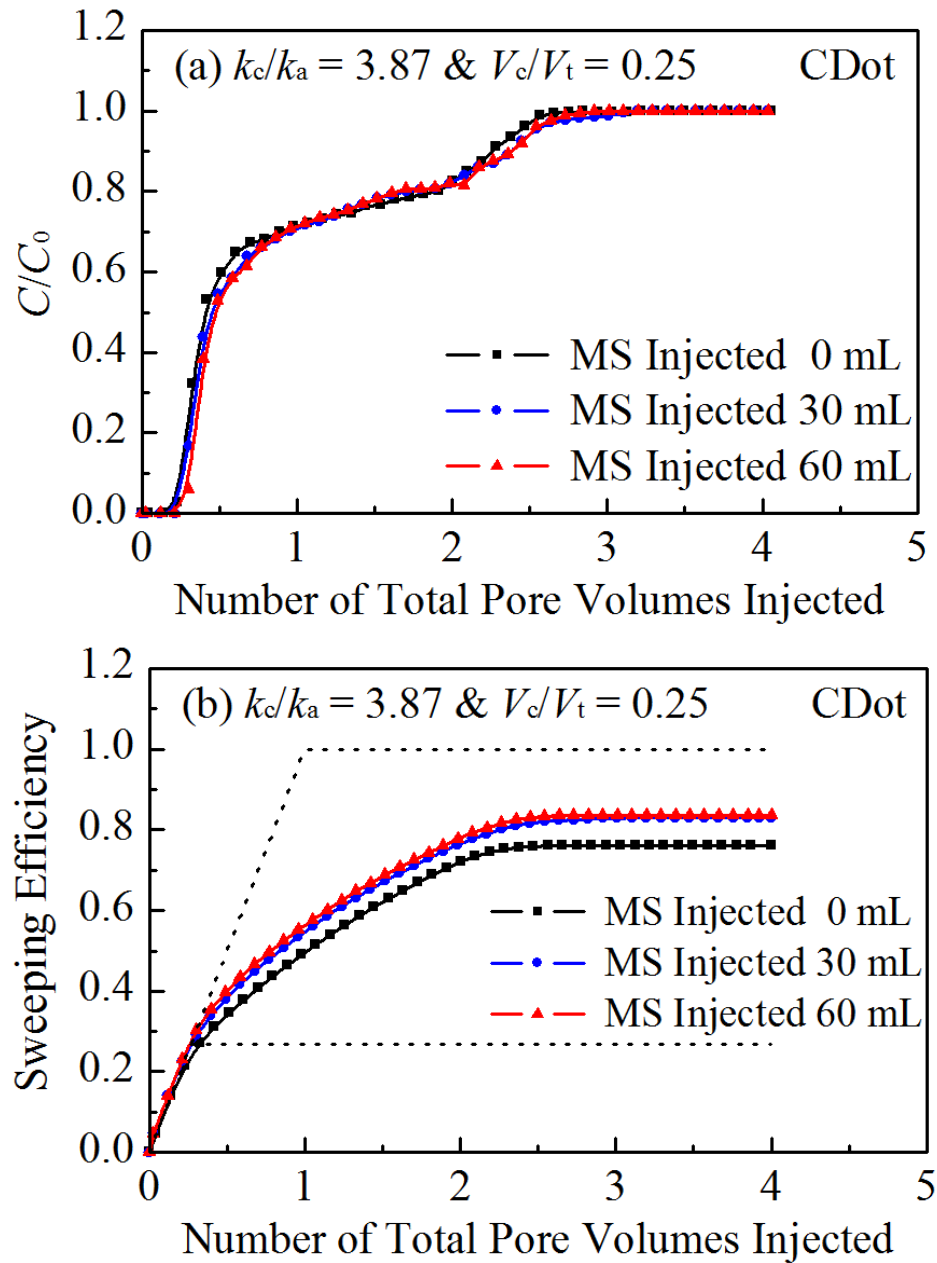


Figure 3.12: (a) Breakthrough curve of CDot tracer. Black, blue and red dots are the concentration of CDot tracer when 0 mL, 30 mL and 60 mL of elastic microspheres are injected. (b) is the sweeping efficiency plot for the same experiments (the same as the fraction of tracer-filled total porosity on previous plots).

It should be noted that the shift of curves in Figure 3.12a is not that envisioned from Figure 3.2. Specifically the arrival of annulus tracer is delayed rather than accelerated. We hypothesize that this results from the MPEMs producing a more piston-like flow in the annulus. Without the MPEMs the flow into the annulus avoids the corner of the annulus at the injection end of the column, but flow occurs into more of this corner if the MPEMs are present. Analysis of this hypothesis would require detailed modeling of how flow in the annulus is changed by the presence of MPEMs. This is beyond the scope of this paper. The conclusion of importance here is that column tests can clearly identify even quite subtle flow remediation by constructing retention plots of the kind shown in Figure 3.12b.

Conclusion

Experiments reported here show that the optimum column design for detecting the efficacy of flow-remediating additives has a central core of the same volume as the column annulus and a high contrast in permeability between core and annulus. The best evaluation is possible when a particle tracer is injected at 0.1 mL/min through the column. Particle tracers are much better for detecting the elimination of “dead zones” than chemical tracers because they have much less tendency to fill those zones by diffusion. Properly designed, constructed, and operated laboratory columns can measure flow remediation using an inert nanoparticle tracer.

Acknowledgements

The publication was based on work supported by award KUS-C1-018-02, made by King Abdullah University of Science and Technology (KAUST). We thank experts in the Cornell University Department of Biological and Environmental Engineering for advice and materials, and the Cornell University Physics Department Machine Shop for fabrication of the apparatus.

Supplementary Material

Testing measurement interference for combined KBr and CDot tracers

It has been previously documented CDot nanoparticles are stable in oil field brines¹⁶.

Here we verify that there is no detection interference when CDot and KBr tracers are deployed and measured simultaneously. Figure 3.S1 compares tracer pulse test in which CDots are dispersed in DI water to an identical test in which they are dispersed in a 5000 ppm NaCl, 1000 ppm KBr solution. The column was filled with sand with mean grain diameter of 177-250 μm , a porosity of 0.385, a permeability of 23.87 μm^2 , and the flow rate through the column was 1 mL/min. Same column is used in both experiments. The overlap of the curves indicates no measurement interference.

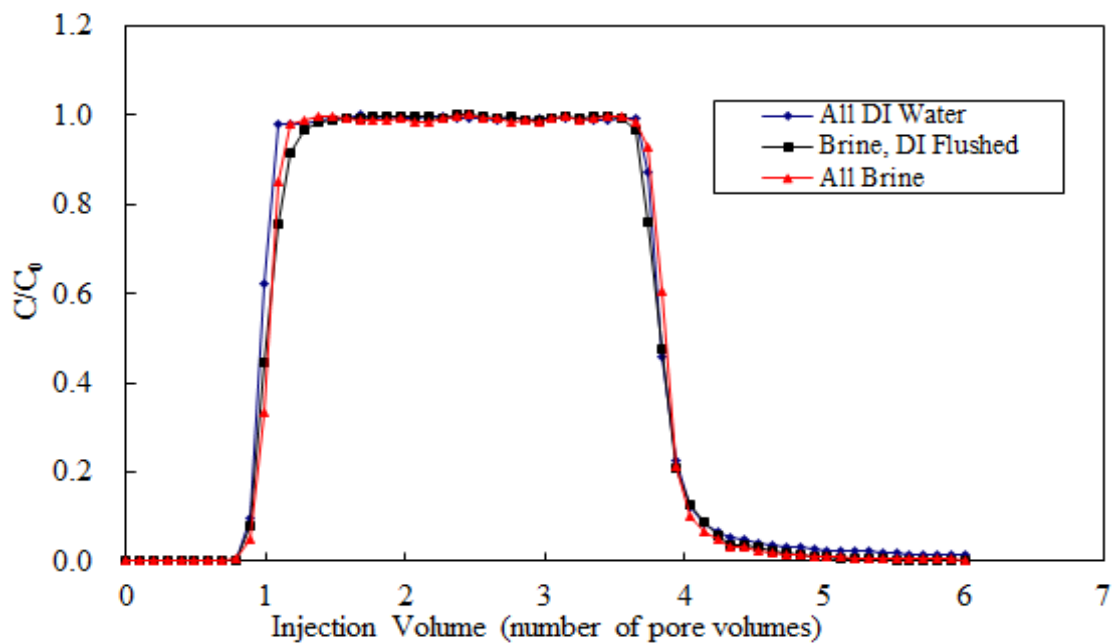


Figure 3.S1: Pulse tracer test for ~3 pore volumes injected. Blue curve is effluent concentration of CDot when it is dispersed, injected and then flushed with DI water. Black curve is CDot injected in 5000ppm NaCl and 1000ppm KBr brine and then flushed with DI water. Red curve is the same except flushing is with CDot-free brine.

Measuring CDot retention

The amount of tracer left behind from the start to the end of the experiment indicates the column volume accessed by tracer. The amount of tracer retained in the column is calculated:

$$f = \frac{\int_0^t Q \left(1 - \frac{C_{(t)}}{C_0}\right) dt}{V_{total}} \quad (3.S1)$$

Here f is the fraction of total pore volume filled with the tracers, Q is the volumetric injection rate, C_0 is the injection tracer concentration, $C_{(t)}$ is the effluent tracer concentration at time t , and finally, V_{total} is the total available pore volume of the system. f has a value that ranges from 0 and 1.

Predicting diffusion from the core into the annulus

We have found in previous work³² that the inverse Peclet number defined in 3.S2a provides a good measure of diffusion from the core of a heterogeneous column of the design described in the text into the column annulus. The inverse Peclet number, N_{iPe} , is defined as the ratio of time it takes the fluid to fill the total porosity of the system to the time for a tracer to diffuse into the annulus.

$$N_{iPe} = \frac{\text{time to fill total porosity}}{\text{annulus diffusion time constant}} = \frac{t_{fill}}{t_{diff}} \quad (3.S2a)$$

If N_{iPe} is much less than 1, the tracer passes through the system quickly with very little diffusion into the annulus. When N_{iPe} is close to or greater than 1, diffusion into the annulus is dominant. Because CDots and Br have very different diffusion constants, N_{iPe} will differ.

In our system, 3.S2a can be evaluated:

$$t_{fill} = \frac{L}{v_a}, \quad v_a = \frac{q_a}{\Phi_a}, \quad q_a = \frac{Q_a}{A_a}, \quad Q_a = \frac{-k_a' A_a \nabla P}{\mu} \quad (3.S2b)$$

The time it takes tracer to diffuse to the diameter of the annulus, r_a , in 3-dimensional system is:

$$t_{diff} = \frac{r_a^2}{6D_{ea}}, \quad r_a = r_t - r_c \quad (3.S2c)$$

D_{ea} is the effective diffusion coefficient, which depends on other parameters:

$$\begin{cases} D_{ec} \\ D_{ea} \end{cases} = D_\infty \begin{cases} \Phi_c/\tau_c \\ \Phi_a/\tau_a \end{cases} + \begin{cases} a_L \Phi_c v_c \\ a_T \Phi_a v_a \end{cases} \quad (3.S2d)$$

Here D_∞ is the aqueous diffusion constant calculated from Stoke-Einstein's Equation, Φ_c and Φ_a are the porosities in the core and annulus, τ_c and τ_a are the tortuosity of the core and annulus, a_L and a_T are the longitudinal (parallel to the flow direction) and transverse (perpendicular to the flow direction) dispersion coefficients, v_c and v_a are the true average velocity of the fluid in the core channel and annulus. The longitudinal dispersion used in the N_{iPe} calculation is 0.5 cm.

The N_{iPe} for the column experiments in the test are calculated from the experimental parameters (listed) in Table 3.S1.

Table 3.S1: Detailed parameters and calculated N_{iPe} for the flow rate varying heterogeneous column flow experiments.

Parameters	$Q = 10 \text{ mL/min}$		$Q = 1 \text{ mL/min}$		$Q = 0.1 \text{ mL/min}$		$Q = 1/60 \text{ mL/min}$	
	CDot	Br^-	CDot	Br^-	CDot	Br^-	CDot	Br^-
$Q_c (\text{cm}^3/\text{s})$	0.11	0.11	0.011	0.011	0.0011	0.0011	1.8E-4	1.8E-4
$Q_a (\text{cm}^3/\text{s})$	0.059	0.059	0.0059	0.0059	0.00059	0.00059	9.9E-05	9.9E-05
$D_\infty (\text{cm}^2/\text{s})$	1.82E-06	2.02E-05	1.82E-06	2.02E-05	1.82E-06	2.02E-05	1.82E-06	2.02E-05
$q_c (\text{cm/s})$	0.11	0.11	0.011	0.011	0.0011	0.0011	0.00019	0.00019
$q_a (\text{cm/s})$	0.029	0.029	0.0029	0.0029	0.00029	0.00029	4.86E-05	4.86E-05
$v_c (\text{cm/s})$	0.29	0.29	0.029	0.029	0.0029	0.0029	0.00049	0.00049
$v_a (\text{cm/s})$	0.069	0.069	0.0069	0.0069	0.00069	0.00069	0.00012	0.00012
$t_c (\text{s})$	59.74	59.74	597.44	597.44	5974.36	5974.36	35846.14	35846.14
$D_{\text{effc}} (\text{cm}^2/\text{s})^*$	0.056	0.056	0.0056	0.0056	0.00056	0.00057	9.45E-05	9.92E-05
$D_{\text{effa}} (\text{cm}^2/\text{s})^*$	5.08E-07	5.65E-06	5.08E-07	5.65E-06	5.08E-07	5.65E-06	5.08E-07	5.65E-06
$t_{\text{fill}} (\text{s})$	251.90	251.90	2519.02	2519.02	25190	25190	151141	151141
$t_{\text{diff}} (\text{s})$	59207.99	5328.72	59207.99	5328.72	59207.99	5328.72	59207.99	5328.72
N_{iPe}	0.00425	0.0473	0.0425	0.473	0.425	4.73	2.55	28.36

* D_∞ used above is based on Stoke-Einstein's Equation using CDot particle size of 3 nm, and Br^- ion size of 135 pm, viscosity of water at 25 °C. Cell length is 17.5 cm, $D_t = 1.95 \text{ cm}$, $D_c = 1.04 \text{ cm}$, $\tau = 1.5$, $a_L = 0.5 \text{ cm}$.

Simple piston flow model

The two steps in tracer concentration occur as the tracer supplied by flow through the

$$\Delta_c \left(\frac{C}{C_o} \right) = \frac{Q_c}{Q} \text{ so:}$$

$$\Delta \frac{C}{C_o} = \frac{Q_c}{Q} + \frac{Q_a}{Q}, \quad 3.S3$$

$$Q_a = \frac{-k'_a A_a \nabla P}{\mu}, \quad 3.S4a$$

$$Q_c = \frac{-k'_c A_c \nabla P}{\mu}, \quad 3.S4b$$

$$\frac{Q_c}{Q} = \frac{k'_c A_c}{k'_a A_a + k'_c A_c}, \quad 3.S5$$

In the case that $A_c = A_a$, $\frac{Q_c}{Q} = 2/3$ when $k'_c = 2k'_a$ and = 0.6 when $k'_c = 1.5k'_a$.

The time required for tracer to arrive through the core is:

$$t_c = \frac{V_c}{Q_c} = \frac{A_c \Phi_c L}{k'_c A_c \left(-\frac{\nabla P}{\mu} \right)} = \frac{\Phi_c L}{k'_c \left(-\frac{\nabla P}{\mu} \right)}, \quad 3.S6$$

Similarly, the time required for tracer to arrive through the annulus is:

$$t_a = \frac{V_a}{Q_a} = \frac{A_a \Phi_a L}{k'_a A_a \left(-\frac{\nabla P}{\mu} \right)} = \frac{\Phi_a L}{k'_a \left(-\frac{\nabla P}{\mu} \right)}, \quad 3.S7$$

The fraction of the total pore volume injected at this time is:

$$\frac{V_{t_c}}{V_{tot}} = \frac{(Q_a + Q_c)t_c}{A_c \Phi_c L + A_a \Phi_a L} = \frac{\frac{k'_a}{k'_c} A_a + A_c}{\frac{\Phi_a}{\Phi_c} A_a + A_c}, \quad 3.S8$$

where we have substituted from S4a and S4b. For $A_a=A_c$, and $\Phi_c=\Phi_a$, $\frac{V_{tc}}{V_{tot}}=0.75$ for

$k'_c=2k'_a$, and $\frac{V_{tc}}{V_{tot}}=0.83$ for $k'_c=1.5 k'_a$. Similarly,

$$\frac{V_{ta}}{V_{tot}} = \frac{(Q_a + Q_c)t_a}{A_c\Phi_c L + A_a\Phi_a L} = \frac{\frac{k'_c}{k'_a}A_c + A_a}{\frac{\Phi_c}{\Phi_a}A_c + A_a}, \quad 3.S9$$

For $A_a=A_c$, and $\Phi_c=\Phi_a$, $\frac{V_{ta}}{V_{tot}}=1.5$ for $k'_c=2k'_a$, and $\frac{V_{ta}}{V_{tot}}=1.25$ for $k'_c=1.5 k'_a$.

References

1. Baker, S. N., & Baker, G. A. (2010). Luminescent carbon nanodots: emergent nanolights. *Angewandte Chemie International Edition*, 49(38), 6726-6744.
2. Baver, C. E. (2013). *Dynamic contact angles and wetting front instability in soils* (Doctoral dissertation, Cornell University).
3. Bear, J. (1972). Dynamics of fluids in porous media. *Eisevier, New York*.
4. Berg, R. R. (1970). Method for determining permeability from reservoir rock properties.
5. Bradford, S. A., Bettahar, M., Simunek, J., & Van Genuchten, M. T. (2004). Straining and attachment of colloids in physically heterogeneous porous media. *Vadose Zone Journal*, 3(2), 384-394.
6. Cao, L., Wang, X., Meziani, M. J., Lu, F., Wang, H., Luo, P. G., ... & Sun, Y. P. (2007). Carbon dots for multiphoton bioimaging. *Journal of the American Chemical Society*, 129(37), 11318-11319.
7. Carman, P. C. (1938). The determination of the specific surface of powders. *J. Soc. Chem. Ind. Trans*, 57, 225.
8. Freeze, R. A., & Cherry, J. A. (1979). Groundwater, 1979. *Printice-Hall, New Jersey*.

9. Gommes, C. J., Bons, A. J., Blacher, S., Dunsmuir, J. H., & Tsou, A. H. (2009). Practical methods for measuring the tortuosity of porous materials from binary or gray-tone tomographic reconstructions. *AIChE journal*, 55(8), 2000-2012.
10. Huai-zhen, Z. H. A. O. (2005). 1, WU Zhao-liang~ 1, ZHENG Xiao-yu~ 2, LIN Mei-qin~ 1, LI Ming-yuan~ 1 (1. Enhanced Oil Recovery Research Center, University of Petroleum, Beijing 102249, China; 2. School of Chemical Engineering, University of Petroleum, Beijing 102249, China); Preparation and Performance Research of Water-soluble Crosslinked Polymer Microspheres [J].*Fine Chemicals*, 1.
11. Huanquan, S., Tao, W., Jianhong, X., & Hui, C. (2006). Novel technique of in-depth profile control step by step by polymer microspheres. *Petrol. Geol. Recovery Effic*, 13, 77-79.
12. Kanti Sen, T., & Khilar, K. C. (2006). Review on subsurface colloids and colloid-associated contaminant transport in saturated porous media. *Advances in Colloid and Interface Science*, 119(2), 71-96.
13. Kretzschmar, R., Borkovec, M., Grolimund, D., & Elimelech, M. (1999). Mobile subsurface colloids and their role in contaminant transport. *Advances in agronomy*, 66, 121-193.
14. Krysmann, M. J., Kelarakis, A., Dallas, P., & Giannelis, E. P. (2011). Formation mechanism of carbogenic nanoparticles with dual photoluminescence emission. *Journal of the American Chemical Society*, 134(2), 747-750.

15. LEI, G. L., & ZHENG, J. P. (2007). Composing of pore-scale polymer microsphere and its application in improving oil recovery by profile control [J].*Journal of China University of Petroleum (Edition of Natural Science)*, 1, 017.
16. Li, Y. V., Cathles, L. M., & Archer, L. A. (2014). Nanoparticle tracers in calcium carbonate porous media. *Journal of Nanoparticle Research*, 16(8), 1-14.
17. Markova, Z., Bourlinos, A. B., Safarova, K., Polakova, K., Tucek, J., Medrik, I., ... & Zboril, R. (2012). Synthesis and properties of core–shell fluorescent hybrids with distinct morphologies based on carbon dots. *J. Mater. Chem.*, 22(32), 16219-16223.
18. McCarthy, J. F., & Zachara, J. M. (1989). Subsurface transport of contaminants. *Environmental Science & Technology*, 23(5), 496-502.
19. Nelson, P. H. (1994). Permeability-porosity relationships in sedimentary rocks. *The log analyst*, 35(03).
20. Neretnieks, I. (1993). Solute transport in fractured rock: applications to radionuclide waste repositories. *Flow and contaminant transport in fractured rock*, 39-127.
21. Newman, J. S. Electrochemical systems, 1973.
22. Niehren, S., & Kinzelbach, W. (1998). Artificial colloid tracer tests: development of a compact on-line microsphere counter and application to soil column experiments. *Journal of contaminant hydrology*, 35(1), 249-259.

23. Nimmo, J. R., & Akstin, K. C. (1988). Hydraulic conductivity of a sandy soil at low water content after compaction by various methods. *Soil Science Society of America Journal*, 52(2), 303-310.
24. Oliviera, I. B., Demond, A. H., & Salehzadeh, A. (1996). Packing of sands for the production of homogeneous porous media. *Soil Science Society of America Journal*, 60(1), 49-53.
25. Ripple, C. D., James, R. V., & Rubin, J. (1973). Radial particle-size segregation during packing of particulates into cylindrical containers. *Powder Technology*, 8(3), 165-175.
26. Ripple, C. D., James, R. V., & Rubin, J. (1974). Packing-Induced Radial Particle-Size Segregation: Influence on Hydrodynamic Dispersion and Water Transfer Measurements. *Soil Science Society of America Journal*, 38(2), 219-222.
27. Ryan, J. N., & Elimelech, M. (1996). Colloid mobilization and transport in groundwater. *Colloids and surfaces A: Physicochemical and engineering aspects*, 107, 1-56.
28. Saffman, P. G., & Taylor, G. (1958). The penetration of a fluid into a porous medium or Hele-Shaw cell containing a more viscous liquid. *Proceedings of the Royal Society of London. Series A. Mathematical and Physical Sciences*, 245(1242), 312-329.

29. Saiers, J. E., Hornberger, G. M., & Harvey, C. (1994). Colloidal silica transport through structured, heterogeneous porous media. *Journal of Hydrology*, 163(3), 271-288.
30. Schiegg, H. O. (1990). Laboratory setup and results of experiments on two-dimensional multiphase flow in porous media, English translation JF McBride, DN Grahame, Rep. PNL-7453Pac. Northwest Lab., Richland, Wash.
31. Steenhuis, T. S., Baver, C. E., Hasanzadeh, B., Stoof, C. R., DiCarlo, D. A., & Selker, J. S. (2013). Pore scale consideration in unstable gravity driven finger flow. *Water Resources Research*, 49(11), 7815-7819.
32. Subramanian, S. K., Li, Y., & Cathles, L. M. (2013). Assessing preferential flow by simultaneously injecting nanoparticle and chemical tracers. *Water Resources Research*, 49(1), 29-42.
33. Yang, S. T., Wang, X., Wang, H., Lu, F., Luo, P. G., Cao, L., ... & Sun, Y. P. (2009). Carbon dots as nontoxic and high-performance fluorescence imaging agents. *The Journal of Physical Chemistry C*, 113(42), 18110-18114.
34. Yao, C., Lei, G., Cathles, L. M., & Steenhuis, T. S. (2014). Pore-Scale Investigation of Micron-Size Polyacrylamide Elastic Microspheres (MPEMs) Transport and Retention in Saturated Porous Media. *Environmental science & technology*.

35. Yao, C., Lei, G., Li, L., & Gao, X. (2012). Selectivity of pore-scale elastic microspheres as a novel profile control and oil displacement agent. *Energy & Fuels*, 26(8), 5092-5101.
36. Yao, C., Lei, G., Li, W., Li, L., & Gao, X. (2012). An Experiment and Simulation of Elastic Microspheres Enhanced Oil Recovery (EMEOR). *Energy Sources, Part A: Recovery, Utilization, and Environmental Effects*, 34(8), 692-701.

CHAPTER 4

MEASURING THE SWEEP ENHANCEMENT OF MICRON-SIZED POLYACRYLAMIDE ELASTIC MICROSPHERES (MPEMs)

Abstract:

Quantitative evaluation of the enhanced sweeping produced by the injection of micron-size polyacrylamide elastic microspheres (MPEMs) into a heterogeneous porous media is essential for using them to improving oil recovery. Using dual-tracer methods established in a Chapter 3, five dual-permeability columns packed with angular quartz sand are used to investigate the sweep improvement and profile modification related to injecting MPEMs into a heterogeneous porous media. In the best case where the matching factor between the MPEMs and sand pore throat size is 1.36, injecting the MPEMs increased the sweep by 9.6%, and larger core pore volume columns enhanced the sweep more. These experimental results validate the feasibility and effectiveness of dual-tracer methods for measuring sweep enhancements.

Introduction

Oil recovery from a reservoir by flooding is mainly controlled by the swept volume and displacement efficiency.^{1,2} Expanding the swept volume and increasing displacement efficiency are the two ways oil recovery might be enhanced by chemical flooding. Expanding the swept volume has enhanced recovery more than increasing displacement efficiency.³ One of the more promising methods of expanding swept volume is to preferentially plug the high-permeability flow paths with micron-size polyacrylamide elastic microspheres (MPEMs) so that flow is forced through unswept low-permeable zones which contain oil.⁴⁻⁶ MPEMs treatment has proven a cost-effective method to modify flow heterogeneity and enhance oil recovery from reservoir rocks in Daqing, Shengli, Changqing, Jidong and Bohai Oilfield in China.⁷⁻¹¹ It is not clear however how the MPEMs contributed to enhanced recovery.

Heterogeneous double-tube models are most commonly used to evaluate the enhanced sweeping of flow modifying additives such as particulate MPEMs.¹⁷ These double-tube experiments are evaluated by the change of the proportion of flow through each tube.¹⁸ Although these experimental results provide valuable insights into the plugging and diversion capabilities of the MPEMs, they cannot evaluate the cross-flow between the layers in actual oil reservoirs,¹⁹ and thus cannot clearly indicate the benefits of the greater depth penetration that is possible with the deformable MPEMs.

Many properties of MPEMs have been studied: The MPEMs are size- and strength-controlled, environmentally friendly, and not sensitive to reservoir minerals and formation water salinity.¹² The MPEMs have good swelling properties, and are stable

in harsh reservoir conditions (temperatures of ~ 90 °C, salinities of > 20,000 mg/L, and pH values from 4.0–10.3).¹³ Owing to their low viscosity and good dispersibility in brine, MPEMs can be pumped into the oil formation at any rate.¹⁴ In oil formations, MPEMs can selectively plug large pore-throats through the mechanisms of capture-plugging, superposition-plugging and bridge-plugging, all of which produces resistance to water flow. In addition, MPEMs particulate filtering in the interior of porous media can enhance their plugging effect, while MPEMs filtering on the surface of low-permeability layer can prevent the permeability of the low-permeability layer from being decreased by the MPEMs. More importantly, MPEMs can remigrate in when pore-throats are put under pressure and impair flow in up to four successive pore-throats.¹⁵ The ability to force MPEMs further into the reservoir because they elastically deform is perhaps their greatest advantage.¹⁶ The matching relationship between the MPEMs and oil reservoirs plays an important role in sweep improvement. Conventional particles have difficulty migrating deeper into the oil reservoir once they are retained near the wellbore. The matching factor, or the ratio of MPEMs particle diameter to average pore-throats diameter of oil reservoirs, is optimum between 1.35–1.55. Outside this range, sweep improvement and profile modification is be poor.¹⁶

It is difficult to evaluate all these claims in the field where many processes and factors can apply. The quantitative evaluation of the enhanced sweeping of MPEMs in the laboratory is therefore important. Little is in fact known about how the MPEMs enhanced sweep in heterogeneous media.

In this work, a series of dual-permeability single-tubed columns packed with angular quartz sand more realistically reflect the cross flow that occurs between more and less

permeable portion of heterogeneous media. Using a dual-tracer analysis method and simultaneously injecting a potassium bromide (KBr) and fluorescent carbon nanoparticles (CDot) tracer described in Chapter 3, the fraction (f_v) of the column swept by the tracers can be determined, and the change in this fraction caused by injecting the MPEMs can be determined. The aim of the research reported here is to quantitatively evaluate the enhanced sweeping of MPEMs in heterogeneous porous media when cross-flow between the layers is allowed.

Materials and methods

Dual-Permeability Column Model.

The dual-permeability column consists of an outer acrylic glass tube, a copper netted tube, two copper filters, two rubber O-rings, and two plastic fittings, as illustrated in Figure 4.1. The outer acrylic glass cell has inner diameter of 1.95 cm diameter and is 17.50 cm in length. All parts are machined by Cornell University Machine Shop.

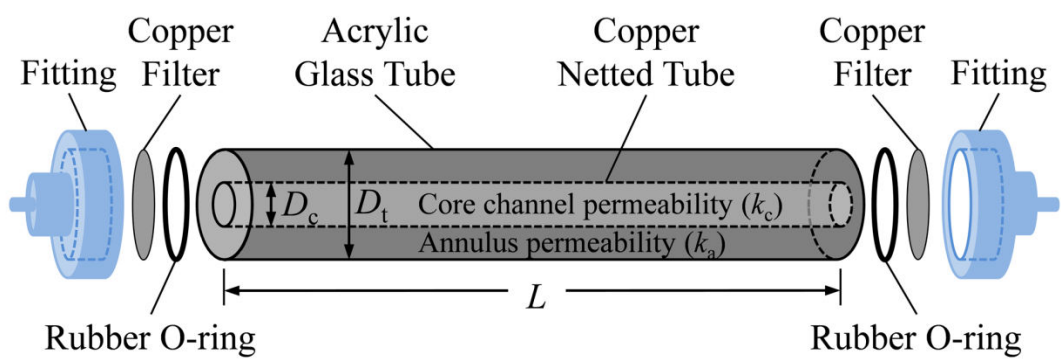


Figure 4.1. Diagram of dual-permeability column model. L is the length of acrylic glass tube, D_t is the diameter of acrylic glass tube, and D_c is the diameter of copper netted tube.

Materials and Reagents.

Micron-size polyacrylamide elastic microspheres (MPEMs) used in this study were prepared using the methods reported by Yao et al.²⁰ The MPEMs are milky-white in color and have a density of ~1.0 g/cm³. Dry MPEMs have average diameters, d_{ave} ~27.4 μm. The average particle size of MPEMs after swelling in 5000 mg/L NaCl solution at 25 °C for 10 days is ~49.3 μm. An inverse microscope image of the MPEMs is shown in Figure 4.2. The viscosity of a 0.1%–0.3% (mass fraction) MPEM suspension is <1.6 mPa·s at 25 °C, and pH ~7.0. The chemical tracer used in the experiments was reagent grade KBr provided by ACROS (Geel, Belgium). The diffusion constant of KBr in aqueous solution at 25 °C is known from direct calculation using the Stokes-Einstein equation²¹ and the value is ~ 2.45×10^{-5} cm²/s. The particle tracer used in our experiments was composed of fluorescent carbon nanoparticles, or CDots. The CDots particle size is 3–5 nm. They were prepared in the method described by Krysmann et al.²² The diffusion constant for CDot in aqueous solution at 25 °C is ~ 1.25×10^{-6} cm²/s, which corresponds to the average particle size of ~3.9 nm according to Stokes-Einstein equation.

Angular quartz sand provided by AGSCO (Hasbrouck Heights, NJ) was selected as the porous media. The sand density is ~2.65 g/cm³ and the pH value in deionized (DI) water is ~7.0. The major components of the sand are SiO₂, Al₂O₃, Fe₂O₃ and K₂O, where SiO₂ contributes > 98% of the total mass. Prior to use, the sand was acid-washed and oven dried to remove surface impurities and to minimize chemically attractive microsites on the sand, as described by Zevi et al.²³ Then the sand was

ground and sieved into four size ranges: 74–106, 106–125, 125–177 and 177–250 μm .

The NaCl solution with a salinity of 5000 mg/L was the injected brine.

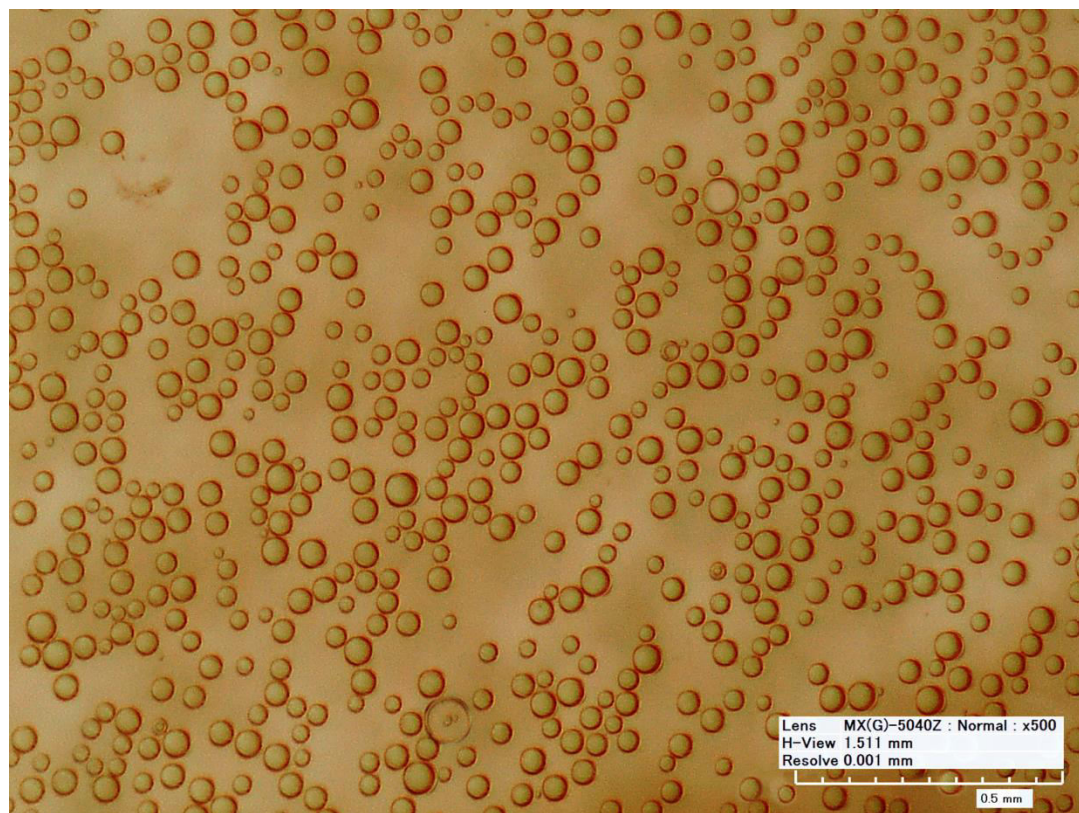


Figure 4.2. Inverse microscope image of MPEMs after swelling in NaCl solution of 5000 mg/L at 25 °C for 10 days.

Apparatus and Process.

The major components of the experimental apparatus included a syringe pump, a peristaltic pump, a magnetic stirrer, a small tube, a steel ruler, a dual-permeability column, and an automatic sampler. The experimental process is schematically illustrated in Figure 4.3. Injection and production are placed at the same elevation to avoid gravity flow.

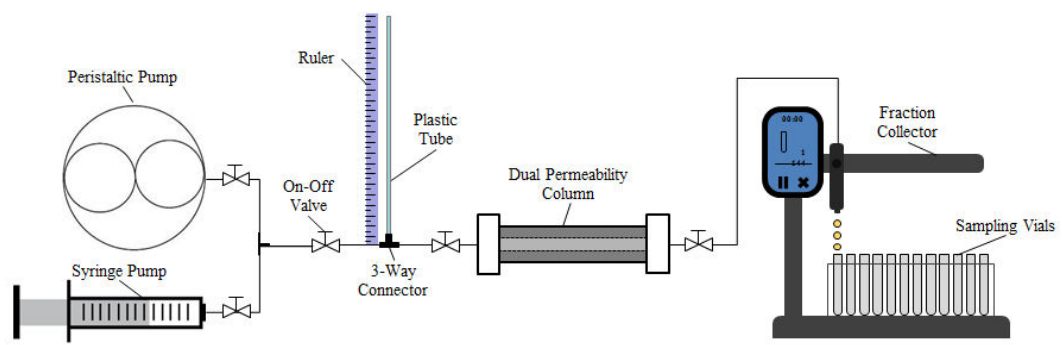


Figure 4.3. Flow diagram for dual-tracer experiments.

Methods and Procedures.

Five dual-permeability columns were constructed for this study. The columns were packed with the angular quartz sand using air-free packing protocol described in Chapter 5. The size ranges of the quartz sand packed into the core channel covered the 4 size ranges given above. The annulus was always filled with the finest 74~106 μm sand. Table 4.1 lists the important column parameters and Figure 4.4 illustrates the column. The core channel diameters (D_c) of the columns were controlled by the copper net tubes of 1.0, 1.0, 1.0, 0.50, and 1.36 cm diameter, respectively. The matching factor (δ) between the particle size of MPEMs and the pore-throat diameter of porous media was calculated with eq. 4.1.¹⁶

$$\delta = \frac{d_{\text{ave}}}{2r} \quad (4.1)$$

where d_{ave} is the average particle size of MPEMs, μm ; r is the average pore-throat radius of porous media, μm .

The average pore-throat radius of porous media in eq. 4.1 was calculated using eq. 4.2.²⁴

$$r = \sqrt{\frac{8k}{\varphi}} \quad , \quad (4.2)$$

where k is the permeability of porous media in unit of μm^2 , and φ is the porosity of porous media.

Table 4.1. Key Parameters of Dual-Permeability Columns.^a

Experiment	L (cm)	D_t (cm)	D_c (cm)	φ_a	φ_c	V_t (cm ³)	V_c (cm ³)	k_a (μm^2)	k_c (μm^2)	k_c/k_a	V_c/V_t	δ_a	δ_c
1	17.50	1.95	1.0	0.42	0.41	21.81	5.63	3.28	9.87	3.01	0.25	3.12	1.78
2	17.50	1.95	1.0	0.42	0.40	21.68	5.50	3.28	16.46	5.01	0.25	3.12	1.36
3	17.50	1.95	1.0	0.42	0.39	21.54	5.36	3.28	23.87	7.27	0.25	3.12	1.11
4	17.50	1.95	0.50	0.42	0.39	21.85	1.34	3.28	23.87	7.27	0.06	3.12	1.11
5	17.50	1.95	1.36	0.42	0.39	21.19	9.91	3.28	23.87	7.27	0.48	3.12	1.11

^a L is the model length, D_t is the total diameter, D_c is the core channel diameter, φ_a is the annulus porosity and φ_c is the core channel porosity, V_t is the total pore volume and V_c is the core pore volume, k_a is the annulus permeability and k_c is the core channel permeability, δ_a , δ_c are the matching factors of the MPEMs with the pore-throat diameter of annulus and core channel calculated for an MPEM diameter of 49.3 μm using the methods in reference¹⁶.

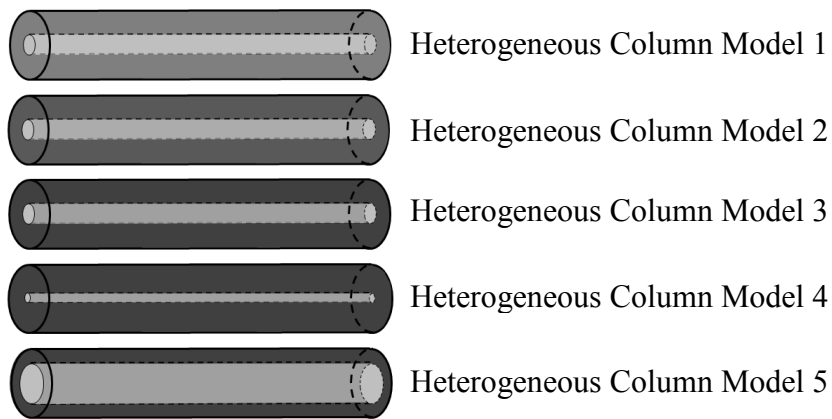


Figure 4.4: Illustration of Column 1-5. Greater core-annulus permeability ratios are illustrated as the greater color contrast between the core and annulus channel. Core size differences are reflected by the size of the light gray center channel.

All experiments were conducted at ~25 °C. Before each experiment, the heterogeneous column was flushed with 4.0 pore volumes (PV) of brine water with a salinity of 5000 mg/L NaCl to ensure that the porous media was completely saturated with the brine water of 5000 mg/L NaCl. Then 4.0 PV of brine water with the same concentration of 5000 mg/L containing 0.1% KBr and 0.005% CDot by weight was injected with a flow rate (Q) of 0.1 mL/min. Effluent samples were collected at constant time intervals of 20 min using an automatic sampler. At the end of each experiment, tracer-free 5000 mg/L NaCl brine was injected through the porous media for until the effluent concentrations reached the baseline levels for the tracers. Next, a 15 mL pulse of MPEMs suspension of 0.2% by weight in 5000 mg/L NaCl was injected into the column followed by the injection of 4.0 PV of tracer with 0.1% KBr and 0.005% CDot by weight in 5000 mg/L NaCl at the same flow rate of 0.1 mL/min, and the effluent samples collected. The column was flushed again with brine, another 15 mL pulse of 0.2% MPEMs suspension in 5000 mg/L NaCl was injected, 4.0 PV of tracer with 0.1% KBr and 0.005% CDot in 5000 mg/L NaCl was injected, and so on, until 60 mL of 0.2% MPEMs had been injected. The effluent concentrations of KBr before and after each pulse of the MPEMs suspension were measured using an ion-selective electrode connected with a pH/mV/temperature microprocessor handheld meter (6230N, Jenco Instruments, CA), and the concentrations for CDot were measured with a fluorescence spectrophotometer (SpectraMax M2e, Molecular Devices, Sunnyvale, CA). At the end of each experiment, the fraction (f_v) of the total column pore volume filled with tracer was calculated using eq. 4.3.²⁵

$$f_v = \frac{\int_0^{t_f} Q \left(1 - \frac{C}{C_0}\right) dt}{V_t}, \quad (4.3)$$

where C_0 is the injected tracer concentration, C is the effluent tracer concentration, V_t is the total pore volume, Q is the injection flow rate, and t_f is the elapsed time since tracer injection.

Results and discussion

Breakthrough Curves of KBr and CDot before and after Injection of MPEMs.

As described in Chapter 3, no-flow or “dead” zones are created when heterogeneities are introduced. The injection of MPEMs selectively plugs the pore throats in the higher permeability flow channels and diverts the flow to lower permeability flow zones. As a result, the fluid flow becomes more uniform, and the “dead zone” volume is reduced. The changes in dead zone volume can be seen in the breakthrough curves (BTCs) of the KBr and CDot tracers, but are better and more clearly seen in the fraction plots derived from these curves using equation (4.3).

Figure 4.5 shows the breakthrough curves (BTCs) of the KBr and CDot tracers, and Figure 4.6 plots the integral fraction (f_v) curves of KBr and CDots before and after injection of MPEMs in experiment 3 in Table 4.1.

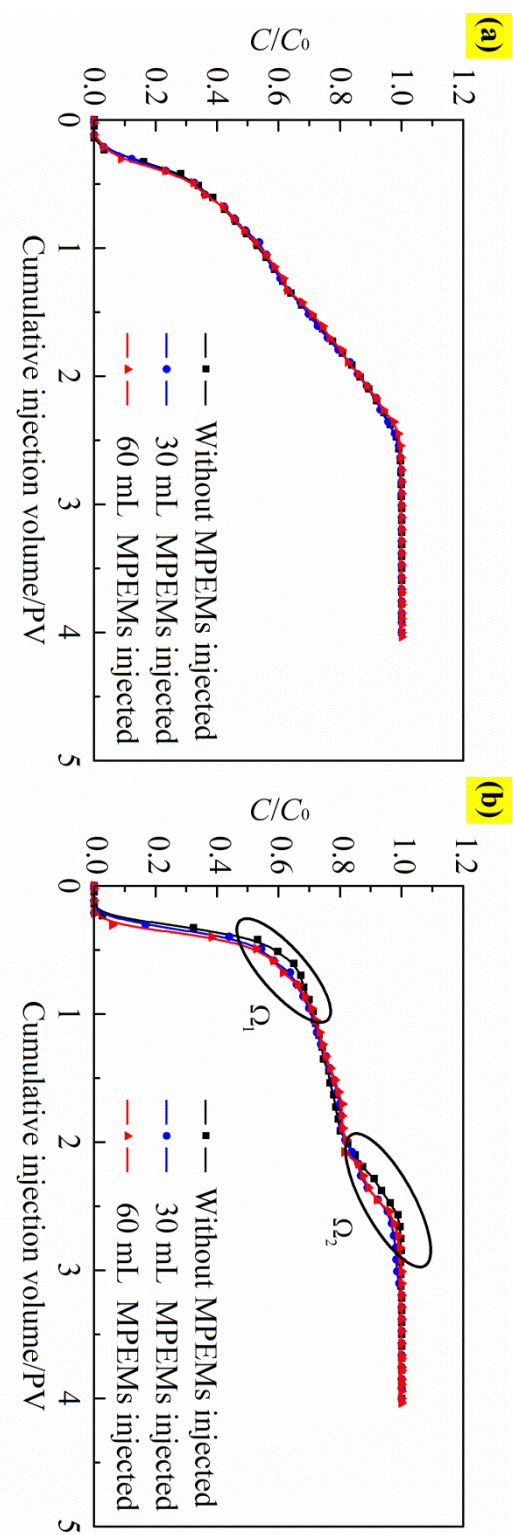


Figure 4.5. Breakthrough curves (BTCs) of (a) KBr and (b) CDot before and after injection of MPMEMs in model 3: $k_c/k_a = 7.27$ & $V_c/V_t = 0.25$.

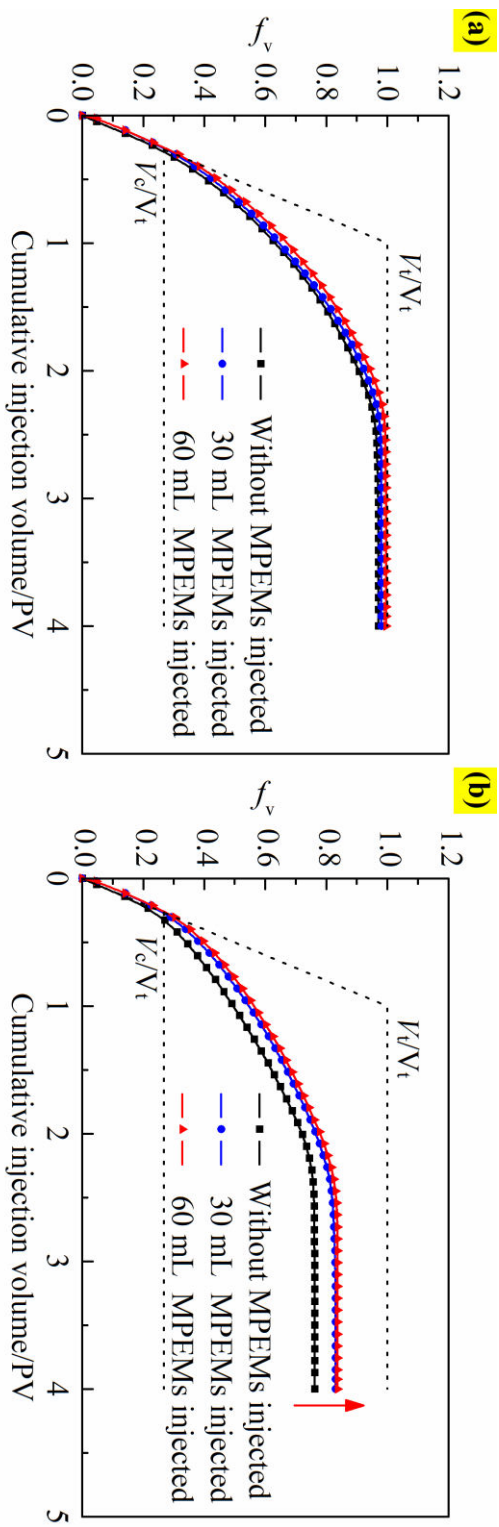


Figure 4.6. Integral fraction (f_v) curves of (a) KBr and (b) CDot before and after injection of MPMEMs in model 3: $k_c/ka = 7.27$ & $V_c/V_t = 0.25$.

Subtle changes in the KBr BTC are observed after injecting MPEMs, but the change in the CDot BTC is much more pronounced. The same effect is seen in the fraction curves in Figure 4.6. The f_v curves of KBr all tend toward the upper limit of 1.0 and overlap, but the f_v curves of the CDots clearly shows the reduction in dead zone volume produced by the MPEMs.

In Figure 4.5b there are two pockets marked as Ω_1 and Ω_2 that appear between the CDot BTCs before and after the injection of MPEMs. The retardation of core tracer arrival creates the first pocket (or Ω_1). The retardation results from increased flow rate in the annulus channel due to degradation of the core permeability by MPEMs injection. The shift at Ω_2 reflects a greater sweep (reduction of dead flow zones) in the annulus. Figure 4.7 illustrated how this greater sweep is produced by pushing flow more into the column corner at its influent end.

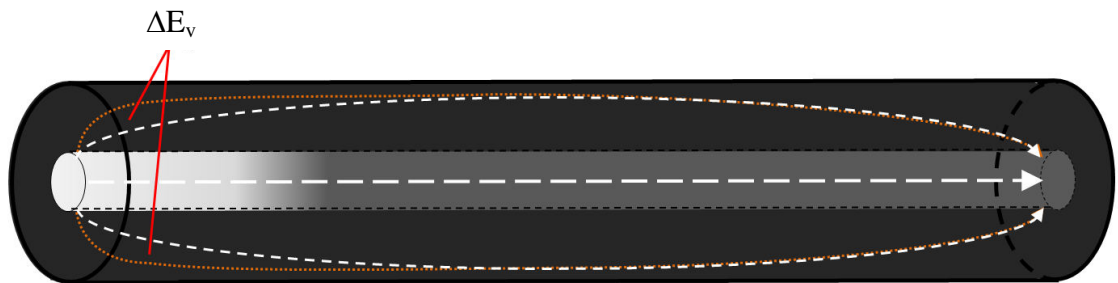


Figure 4.7: Graphical illustration of heterogeneous column flow. The white shade in the core channel illustrates the core plugging of MPEMs. The white dashed lines indicate flow in the core and annulus before injection of the MPEMs. The orange dotted line indicates flow in the annulus after MPEM injection. The flow in the core is similar but slower. The increased sweep in the annulus is indicated by ΔE_v .

It is important to note in Figure 4.6 that the flow changes are clearly apparent only for the CDot tracer. The KBr tracer diffuses so rapidly into the annulus (in fact completely filling it) that the changes in sweep are masked. However, the KBr tracer still provides an important confirmation of flow heterogeneity. The complete filling of the annulus with KBr (Figure 4.6a) and the only partial filling with CDots (Figure 4.6b) indicated heterogeneous flow, but only the CDots indicate the changes in sweep (Ω_1 and Ω_2).

Enhanced Sweeping of MPEMs in Heterogeneous Porous Media.

The five dual-permeability column models with different permeability ratios (k_c/k_a) and core pore volume proportions (V_c/V_t) were evaluated by the change of the CDot BTCs before and after the MPEMs injection. Additionally, the enhanced volumetric sweep efficiency (ΔE_v , %) achieved by injecting the MPEMs was calculated by using eq. 4.4.

$$\Delta E_v = \left([f_{v\text{-Cdot}}]_{\max}^a - [f_{v\text{-Cdot}}]_{\max}^b \right) \quad (4.4)$$

Here $[f_{v\text{-Cdot}}]_{\max}^a$ and $[f_{v\text{-Cdot}}]_{\max}^b$ refer to the maximum fraction (f_v) values of CDot after and before the injection of MPEMs calculated from eq. (4.3), respectively. Results are shown in Table 4.2.

Table 4.2. Enhanced Sweeping of MPEMs in Dual-Permeability Models.

Model	k_c/k_a	V_c/V_t	V_{inj} (mL)	$[f_{v\text{-CDot}}]_{\max}$	ΔE_v (%)
1	3.01	0.25	0	0.9228	0.00
			15	0.9579	3.51
			30	0.9677	4.49
			45	0.9699	4.71
			60	0.9701	4.73
2	5.01	0.25	0	0.8386	0.00
			15	0.9281	8.95
			30	0.9325	9.39
			45	0.9341	9.55
			60	0.9346	9.60
3	7.27	0.25	0	0.7618	0.00
			15	0.8076	4.58
			30	0.8295	6.77
			45	0.8343	7.25
			60	0.8363	7.45
4	7.27	0.06	0	0.8687	0.00
			15	0.9257	5.70
			30	0.9296	6.09
			45	0.9318	6.31
			60	0.9329	6.42
5	7.27	0.48	0	0.6459	0.00
			15	0.6714	2.55
			30	0.6935	4.76
			45	0.7119	6.60
			60	0.7254	7.95

(1) Effect of Permeability Ratio (k_c/k_a) on ΔE_v .

Figure 4.8 plots the breakthrough curves (BTCs) of the CDot tracer before and after MPEM injection for three dual-permeability column designs (Experiments 1–3), and the change in volumetric sweep efficiency (ΔE_v) as the result of successive pulsed of MPEM injection. Volumetric sweep efficiency increases as the result of MPEM injection in all the columns..The sweep increases with the volume of MPEMs injected up to about 30 mL, and then increases only very slowly (Figure 4.8d). The sweep increase is most pronounced for $k_c/k_a=5.01$. Lower and higher values of this ratio show less increase in sweep. This surprising effect results from the matching factor being optimum (between 1.35 to 1.55) for the core sand in experiment 2. As shown in Table 4.1 the matching factor for experiments 1-3 are 1.78, 1.36 and 1.11 respectively. The matching factor is just right for experiment 2, but too high in experiment 1 and too low in experiment 3.

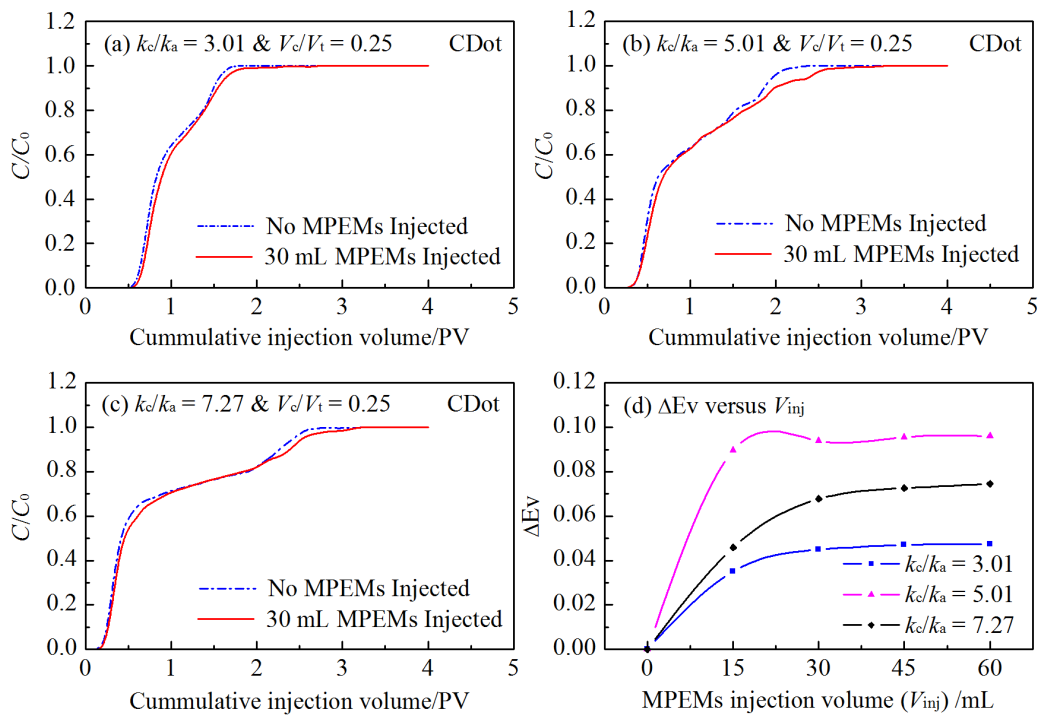


Figure 4.8. Breakthrough curves (BTCs) of CDot before and after injection of MPEMs in dual-permeability models (Experiments 1–3): (a) Experiment 1: $k_c/k_a = 3.01$ & $V_c/V_t = 0.25$, (b) Experiment 2: $k_c/k_a = 5.01$ & $V_c/V_t = 0.25$, (c) Experiment 3: $k_c/k_a = 7.27$ & $V_c/V_t = 0.25$. (d) Enhanced volumetric sweep efficiency (ΔE_V) for the three experiments as a function of the volume of MPEMs injected.

(2) Effect of Core Pore Volume Proportion (V_c/V_t) on ΔE_v .

Figure 4.9 shows the breakthrough curves (BTCs) of CDot before and after injection of MPEMs in three dual-permeability columns (Experiments 3–5), and the enhanced volumetric sweep efficiency (ΔE_v) as a function of the injection volume (V_{inj}) of MPEMs. The CDot BTCs show the same characteristic as in Figures 4.5b and 4.8. As the core volume increases the step height of the core arrival increases (Figure 4.9a and b), but at the highest pore volume ratio of 0.48 there is only one step. The “step height” is so high that the dispersion in the column smears out the annulus arrival. Figure 4.9d shows that the sweep ΔE_v curves increase as more MPEMs are injected for the three experiments, but the curves cross each other. The ΔE_v for the smallest volume core increases very fast as MPEMs are injected, but the impact of MPEM injection diminishes after 15 mL injection. It takes more MPEMs to fully treat the second largest core, and even more to fully treat the largest core. The important implication is that, in any reservoir, there will be an optimum MPEM volume that will treat (remedy) the heterogeneities in the reservoir, and injecting MPEMs beyond this optimum will have diminishing benefit.

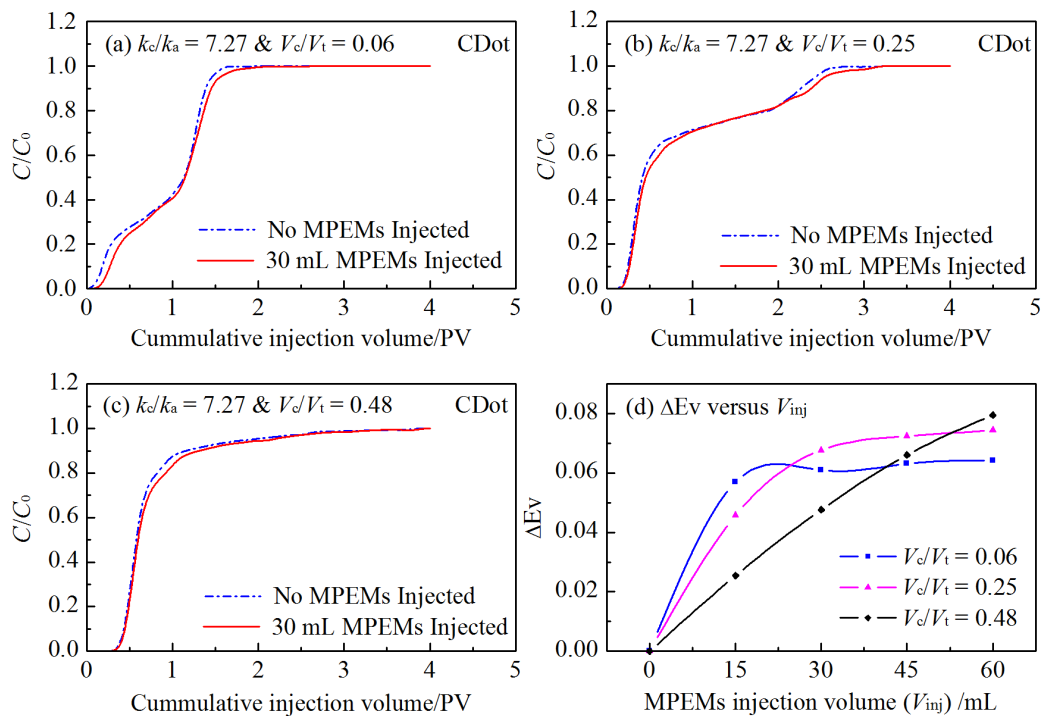


Figure 4.9. Breakthrough curves (BTCs) of CDot before and after injection of MPEMs in dual-permeability columns (Experiments: 3–5): (a) Experiment 3: $k_c/k_a = 7.27$ & $V_c/V_t = 0.06$, (b) Experiment 4: $k_c/k_a = 7.27$ & $V_c/V_t = 0.25$, (c) Experiment 5: $k_c/k_a = 7.27$ & $V_c/V_t = 0.48$, and (d) Enhanced volumetric sweep efficiency (ΔE_v) for the three experiments as a function of the volume of MPEMs injected.

Summary and Conclusions

We have shown how nanoparticles can be used in heterogeneous columns to evaluate sweep improvements associated with flow homogenizing treatments even if the change is small. We show that MPEM injection can increase sweep by almost 10% in some circumstances (Table 4.2). Furthermore we have shown how changes in the effluent tracer curves can identify, to some degree, the mechanisms and locations of flow remediation (Figure 4.6b). The experiments reported here verify the previously-determined optimum range of MPEM to pore throat size ratio (matching factor, Table 4.1). This ratio has proved useful in predicting oil recovery in field treatments, and it is satisfying that it is so clearly indicated in laboratory experiments. Finally, the experiments indicate that each situation (column design or reservoir) will have an optimum treatment intensity (volume of MPEM injection to treated volume) at which flow remediation will be near maximum and beyond which further benefits will be diminishing. The most important of these conclusions is the first: that a new laboratory method of evaluating flow remediation using nanoparticles has been demonstrated. We believe that this new method will find wide application.

Acknowledgement

The publication was based on work supported by award KUS-C1-018-02, made by King Abdullah University of Science and Technology (KAUST). We thank experts in the Cornell University Department of Biological and Environmental Engineering for advice and materials, and the Cornell University Physics Department Machine Shop for fabrication of the apparatus.

References

1. Zhao, F. L. *Enhanced Oil Recovery Principles*; China University of Petroleum Press: Dongying, PRC, 2000.
2. Liu, H. Q.; Zhang, H. L. Research on mechanisms of steam breakthrough and profile control designing for steam soaking well. *Pet. Sci.* 2006, 3(3), 51–55.
3. Wang, J.; Liu, H. Q.; Wang, Z. L.; Hou, P. C. Experimental investigation on the filtering flow law of pre-gelled particle in porous media. *Transp. Porous. Med.* 2012, 94(1): 69–86.
4. Yu, Q. T. A study on strategy and approach to enhance ultimate recovery from oilfields. *Acta Pet. Sinica* 1996, 17 (2), 35–37.
5. Zhao, H. Z.; Wu, Z. L.; Zheng, X. Y.; Lin, M. Q.; Li, M. Y. Preparation and performance research of water-soluble crosslinked polymer microspheres. *Fine Chem.* 2005, 22(1), 62–64.
6. Sun, H. Q.; Wang, T.; Xiao, J. H.; Chen, H. Novel technique of in-depth profile control step by step by polymer microspheres. *Pet. Geol. Recovery Eff.* 2006, 13(4), 77–79.
7. Gao, S. Y. Profile-controlling performances of the crosslinked polymer microsphere in the sub-layers of Daqing Oilfield. *Pet. Geol. Oilfield Dev. Daqing* 2013, 32(4), 112–116.

8. Liu, C. J.; An, Y. R. Research and application of polymer microspheres deep profile control technology. *Drill. Prod. Technol.* 2010, 33(5), 62–64.
9. Li, X. R.; Zhang, Y.; Jia, Y. Q.; Liu, X. C.; Yang, T. Y.; Ma, L. P. Application of polymer microspheres profile-controlling technology in Changqing Oilfield. *Oilfield Chem.* 2012, 29(4), 419–422.
10. Xiong, T. J.; Liu, W.; Lei, Y. L.; Zhang, J.; Luo, D. X.; Luo, H. M. Online profile control technology of Gel microspheres at Liu28 fault block. *Oil Drill. Prod. Technol.* 2007, 29(4), 64–67.
11. Liao, X. W.; Liu, C.; Zhang, Y. L.; Mou, C. R.; Liu, W. Y. Application of novel nano-microspheres profile control and displacement technology in offshore heavy oil field. *Spec. Oil Gas Reservoirs* 2013, 20(5), 129–132.
12. Lei, G. L.; Zheng, J. P. Composing of pore-scale polymer microsphere and its application in improve oil recovery. *J. Chin. Univ. Pet.* 2007, 31(1), 87–90.
13. Lei, G. L. *New Deep Profile Control and Flooding Technology Using Pore-Scale Elastic Microspheres*; China University of Petroleum Press: Dongying, PRC, 2011.
14. Yao, C. J.; Lei, G. L., Gao, X. M., Li, L. Controllable preparation, rheology and plugging property of micron-grade polyacrylamide microspheres as a novel profile control and flooding agent. *J. Appl. Polym. Sci.* 2013, 130(2), 1124–1130.

15. Yao, C. J.; Lei, G. L.; Cathles, L. M., Steenhuis, T. S. Pore-scale investigation of micron-size polyacrylamide elastic microspheres (MPEMs) transport and retention in saturated porous media. *Environ. Sci. Technol.* 2014, 48(9), 5329–5335.
16. Yao, C. J.; Lei, G. L., Li, L., Gao, X. M. Selectivity of pore-scale elastic microspheres as a novel profile control and oil displacement agent. *Energy Fuels* 2012, 26(8), 5092–5101.
17. Zhang, Y. B.; Lu, X. G.; Ren, Y. B.; et al. Displacement efficiency for three different EOR Chemical agents in two-dimension hetrogeneous physical model after polymer flooding. *Oilfield Chem.* 2007, 24(3), 242–245,254.
18. Li, Z. M; Sun, M. S.; Lin, R. Y.; Li, Y.; Xu, Y. H. Laboratory study on foam plugging and selective divided-flow. *Acta Pet. Sinica*, 2007, 28(4), 115–118.
19. Yao, C. J.; Li, L.; Lei, G. L; Gao, X. M. Deep profile control and flooding performance of throat-scale elastic microspheres. *J. Southwest Pet. Univ.* 2013, 35(4), 114–120.
20. Yao, C. J.; Lei, G. L., Gao, X. M., Li, L. Controllable preparation, rheology and plugging property of micron-grade polyacrylamide microspheres as a novel profile control and flooding agent. *J. Appl. Polym. Sci.* 2013, 130(2), 1124–1130.
21. Yin, X. Y. *Microscopic research on diffusion coefficient*; Tianjin University: Tianjin, PRC, 2006.

22. Krysman, M. J.; Kelarakis, A.; Dallas, P.; Giannelis, E. P. Formation mechanisms of carbogenic nanoparticles with dual photoluminescence emission. *J. Am. Chem. Soc.* 2012, 134(2), 747–750.
23. Zevi, Y.; Dathe, A.; McCarthy, J. F.; Richards, B. K.; Steenhuis, T. S. Distribution of colloid particles onto interfaces in partially saturated sand. *Environ. Sci. Technol.* 2005, 39(18), 7055–7064.
24. Hong, S. D. *Basic of Reservoir Petrophysics*; Petroleum Industry Press: Beijing, PRC, 1985.
25. Subramanian, S. K.; Li, Y.; Cathles, L. M. Assessing preferential flow by simultaneously injecting nanoparticle and chemical tracers. *Water Resour. Res.* 2013, 49(1), 29–42.

CHAPTER 5

AIR-FREE PACKING OF SATURATED LABORATORY SAND COLUMNS

Abstract

Laboratory scale column experiments are an important way to test many processes prior to more extensive testing in the field. It has long been recognized that it is critical to properly pack the columns, and good packing protocols have been developed. A relatively un-recognized problem is that under current protocols small amounts of air are retained in the columns that significantly impair experiment repeatability. We describe here a air-free packing protocol that employs a medium duty vacuum pump during preparation of the sand and water and after the column is filled. The method should be of interest in many applications where precision in column testing is desired.

Introduction

Lab scaled column experiments are an important way to test many processes prior to more extensive testing in the field. A great many column tests have been performed to understand the transport of colloidal sized particles, microorganisms, radionuclides, organic molecules, viruses, various polymers, and chemical compounds. It has long been recognized that it is critical to properly pack the columns. A poorly prepared column can result in irreproducible data, mislead the researcher, and compromise data interpretation. Physical heterogeneities can cause colloid aggregation, straining and deposition.^{1,3,8,13,20} A small amount of air can prevent flow to parts of the column.¹⁷ Often multiple column tests are carried out to assess process variability, but for this method to be valid the packing must be consistent enough that differences in packing are not responsible for the differences in column performance that are observed. Achieving column homogeneity is not trivial,^{10,12} even when the packing is with material that has a very uniform grain size distribution.^{10,16} A dense packing can usually be achieved by vibrating during deposition.⁵ However, denser packing does not always mean the flow through the column is uniform. Longitudinal and lateral heterogeneities can occur if deposition and vibration are not very carefully done during dry packing.^{10,15} Mechanical systems have been devised to automate and standardize (usually to a uniform porosity) the filling of the large columns used in soil science studies.^{10,16} But for fluid flow laboratory experiments, as well as many applications outside of soil science where the columns are small, or where the columns are too fragile for mechanical packing, it is not practical to adopt automated mechanical column packing methods.

Packing under saturated conditions was long ago documented. Felt² noted sands could be packed with greater bulk density when moisture is introduced. Hysteretic moisture characteristics and hydraulic conductivities of granular materials have been documented for different compacting methods.^{10,11,19} Oliveira et al.¹² investigated six dry packing and three wet packing procedures for packing rectangular filtration columns. They concluded that the best dry packing technique involves the compaction of 0.2cm layers of sand by tamping with a metal pestle (which gave better results than a wood pestle), and the best wet packing technique was to deposit thin layers of sand in water while mechanically vibrating the column. Both dry packing and wet packing give reproducible column performance if performed carefully. Dry packing is the method of choice if the desired initial state is unsaturated sand, since wet packing would involve extensive care in column drying. Wet packing is the method of choice for saturated columns. A fully saturated homogeneous column packing protocol can serve as an initial condition for studying flow under progressively under-saturated conditions.

In the case motivating the development of the protocol reported here, we sought to evaluate the increase in the homogeneity of flow when expandable and deformable particles were introduced into the permeable central core of a heterogeneous column. We knew the changes induced by the particles would be small, and therefore devoted great effort to careful column packing and to demonstrating that the packing produced reproducible column results. We found the methods described in the literature (as reviewed above) provided good column packing, with one exception. We found that more attention needed to be devoted to being sure that there is no air in the column.

We found that even a small amount of air was detrimental. This note reports the protocols we have developed for assuring that packed columns contain no air. They involve preparation of both the water introduced into a column about to be filled with granular material, and to the preparation of the granular material prior to its being introduced into the water-filled column.

Air in the column

After long trial and error period, we discovered that, with time, small amounts of air separate from the water in a column and collect especially between column inner wall and packed sand. Investigating this issue lead to the conclusion that, in contrast to glass beads, the irregular shape of sand grains tends to trap air. Dissolved or suspended air in the water used for wet packing nucleates on grain surface defects after packing so that air bubbles are physically trapped onto or between sand grains. Figure 5.1 illustrates the inter-granular and intra-granular trapping observed. Figure 5.2 shows the air bubbles that had nucleated on the walls of an empty column 4 hours after filling, showing how air can be introduced into the column from its initial filling with water in preparation for wet-packing.

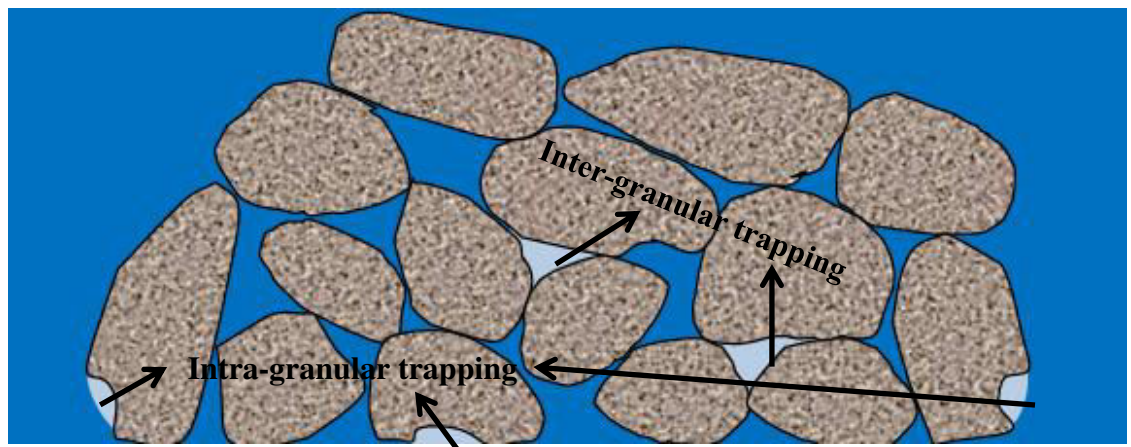


Figure 5.1: Illustration of air trapping mechanisms. Air trapped among multiple grains is denoted as inter-granular trapping, air trapped from a single grain is denoted as intra-granular trapping.



Figure 5.2: Visible air bubbles nucleated on surface defects 4 hours after the column was filled with DI water.

It might be that trapped air is not a significant problem in larger columns or for under-saturated columns. Air degradation of column packing seems not to have been discussed much in the published literature. Niehren et al.⁹ used a vacuum pump for 15 minutes at 50 mbar to remedy visible air bubbles after column packing, but we find it is very difficult to remove trapped air after columns are packed. To ensure the highest packing standard, we find that a vacuum pump must be employed during sand saturation and water filling as well as after column packing. The removal of trapped air by the de-gassing procedures is visible.

The air-free packing protocol

The column design and construction

In this study, we established a packing protocol for a fully saturated homogeneous cylindrical column whose dimensions are 17.5 cm in length, and diameter of 1.95 cm, and a fully saturated heterogeneous cylindrical column with a coarse grained cylindrical core channel and a fine grained annulus. We now describe these procedures and demonstrate their effectiveness. .

The system consist caps and fittings that connect to influent and effluent tubing, copper filters to prevent sand movement, rubber O-ring seals, a Plexiglass tube, and, for heterogeneous columns, a centered copper mesh tube filled with coarse sand that is surrounded by an annulus filled with fine sand. The Plexiglass columns were constructed by Cornell the University Physics Department machine shop.

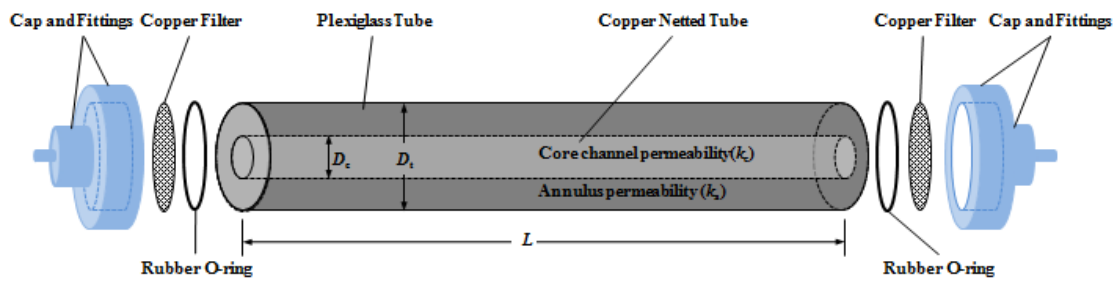


Figure 5.3: Diagram of the Plexiglass column components. The homogeneous column does not have the copper-mesh-defined central core. The length of the column is 17.5cm and the inner diameter of the Plexiglass tube is 1.95cm. The core channel wire mesh has a diameter of 1.04 cm.

The quartz sands used in our experiments were purchased from AGSCO Corporation. Mean grain diameter ranges between 74-250 μm . Individual grains have a density of 2.65 g/cm³. The pH of DI water was between 6.8-7.2. The sands were mainly composed with SiO₂, Al₂O₃, Fe₂O₃ and K₂O where SiO₂ accounted for > 98% of total composition. All sands were sieved, acid washed, thoroughly rinsed with DI water, and then oven dried at 105°C.

The tracer used is a highly fluorescent, 3-5 nm carbon-cored particle tracer decorated with ethanolamine⁶ that is inert (non-sticking) under our experimental conditions.^{7,18} The high diffusion constant (compared to chemical) of the inert particle tracer minimizes diffusion from the core into the annulus, allowing better definition of heterogeneous flow in the column. Tracer concentration is measured with a SpectraMax M2e spectrofluorimeter (Molecular Devices, Inc., Sunnyvale, CA, USA).

Homogeneous Column Packing

For homogeneous column packing, a 3-liter jar is filled with DI water and allowed to sit for a day. Sand (either fine 74 to 106 μm diameter, or coarse 177 to 250 μm), prepared as described above, is re-saturated by immersing in this aged DI water over night. The sand is then carefully transferred under saturated conditions into another container also filled with aged DI water so that it forms a thin layer ~0.3 cm thick. This container is placed in a vacuum chamber and de-gassed for about 30 minutes. Depending on the power of the vacuum pump, sand layers that are too thick will not degas properly. After enough sand has been processed, the column, together with all its end caps and fittings, is immersed in a larger container filled with aged DI water which is then placed in a vacuum chamber and de-gassed for ~10 minutes. After 10

minutes, there should be no more air bubbles visibly emerging. The bottom cap is then placed on the column keeping all parts submerged. Prepared (degassed) sand is then slowly deposited into the water filled column without contacting air. Gentle vibration is applied to all directions using two wood blocks during slow deposition process and the column is slightly overfilled with sand. Sonification was avoided because it could re-suspend precipitated air. The second end cap is then locked on to the over filled end of the column. The entire packed cell, still inside the larger container, is then placed into the vacuum chamber and evacuated overnight (See Figure 5.4). The reason to maintain immersion in DI water in this evacuation process is so that any air removed from the pore space, is replaced by water. The vacuum pump used is Vacuubrand ME1, Germany. Homogeneous column tests are performed the next day, right after taking the column out of the vacuum chamber.

A diagram illustrating this column packing protocol is shown in Figure 5.5.

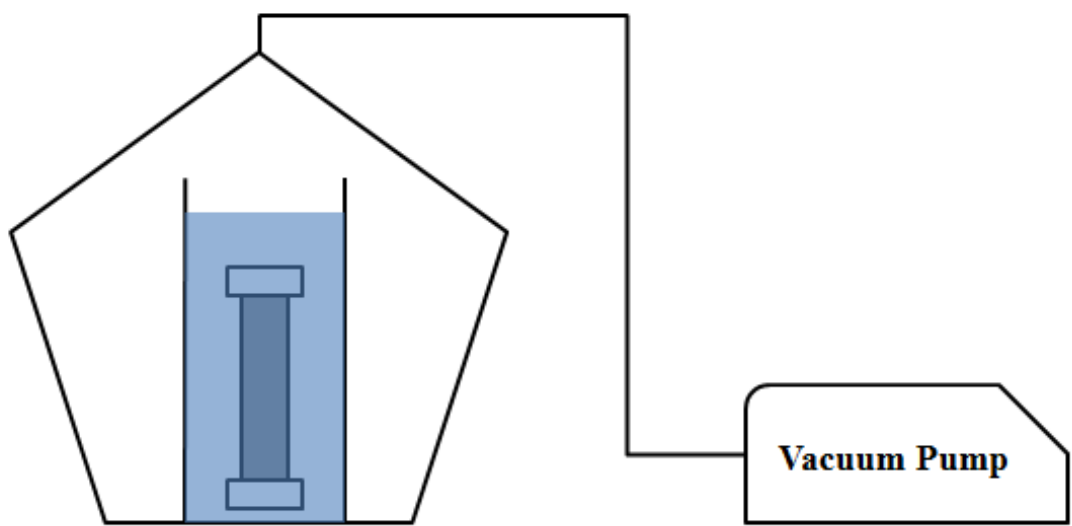


Figure 5.4: Graphical illustration of column vacuum de-gassing.

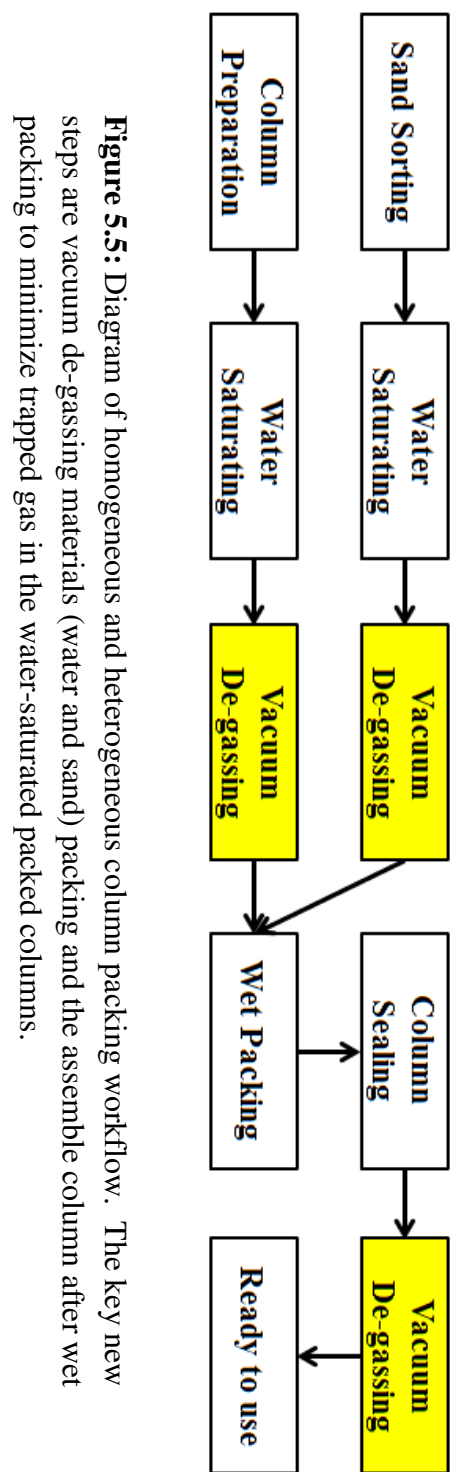


Figure 5.5: Diagram of homogeneous and heterogeneous column packing workflow. The key new steps are vacuum de-gassing materials (water and sand) packing and the assemble column after wet packing to minimize trapped gas in the water-saturated packed columns.

Heterogeneous Column Packing

The procedure is the same as for the homogeneous column except that a thin copper mesh is placed in the center of the column, guided by a very thin circular track on the caps that ensure it is centered properly. Vacuum de-gassing of column is performed with the copper mesh immersed as the fine copper mesh tends to nucleate and trap air bubbles. Sand is introduced into in the copper mesh with an appropriate sized funnel simultaneously with the introduction of finer sand into the annulus between the copper mesh and inner wall of the plexiglass tube. Filling the core channel and the annulus separately will distort the shape of the copper mesh, and filling simultaneously avoids this problem. Gentle vibration using two wood blocks is applied uniformly in all directions.

Results and Discussions

The metric we use to measure the quality of column packing is the reproducibility of tracer tests. Figure 5.6a shows the arrival and termination of a CDot tracer pulse passed through a homogeneous column that is packed and then re-packed with 177 to 250 μm diameter sand. The first column was packed strictly following the protocol described above. After the first test the column was carefully unpacked and the removed material used to repack the column, also strictly following the protocol. A second tracer test was then run in the new, re-packed column. The tracer curves are superimposed in Figure 5.6a. The tracer results are essentially identical which we take as evidence that the packing of a homogeneous column using our air-free procedures is repeatable.

Figure 5.6b compares two tracer experiments in a similarly packed and then re-packed heterogeneous column. Tracer passing through the core channel arrives first and then tracer from the annulus arrives, producing a second step in concentration. The results from the re-packed column are superimposed, and again the two tracer experiments are identical. In both experiments the core was filled with 177-250 μm diameter sand with a porosity of 0.38, and the annulus with 74-105 μm diameter sand with a porosity of 0.42. Porosities were measured by the filled minus unfilled column mass. The column injection rates were 1 mL/min. CDot concentration was measured by fluorescence.

Figure 5.7 shows three tracer experiments of the same kind for which the air-free packing protocol was not followed. The multiple and erratic tracer arrival steps indicate a complicated flow pattern in the annulus due to flow diversion by the presence of air which was sometimes observed to be mobile. The non-repeatability of tracer experiments in Figure 5.7 and the repeatability in Figure 5.6b demonstrates the value of our air-free packing protocol.

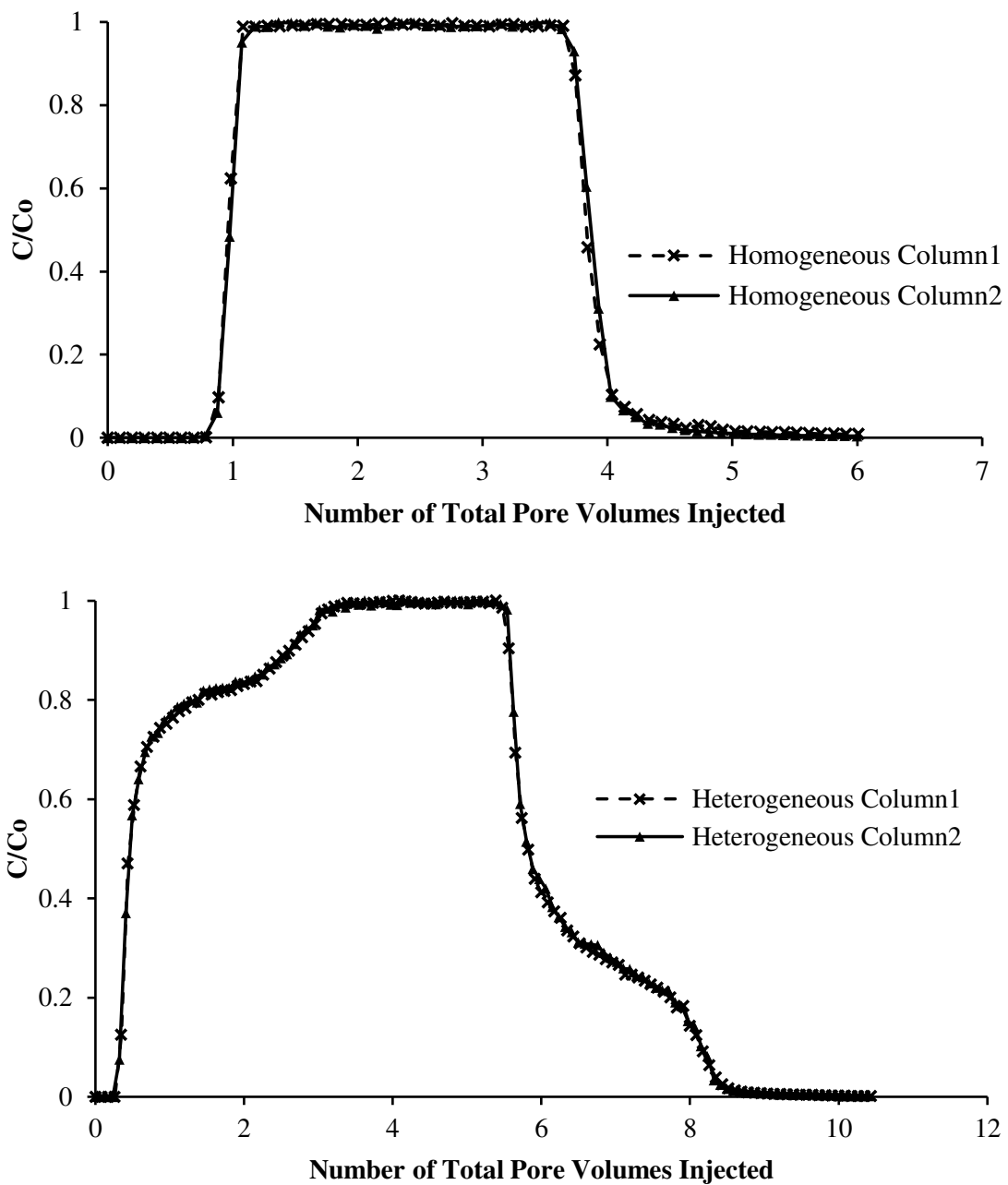


Figure 5.6: (a) CDot tracer arrival curves of repeated homogeneous column tests following air-free packing protocol. (b) CDot tracer arrival curve of repeated heterogeneous column tests following air-free packing protocol.

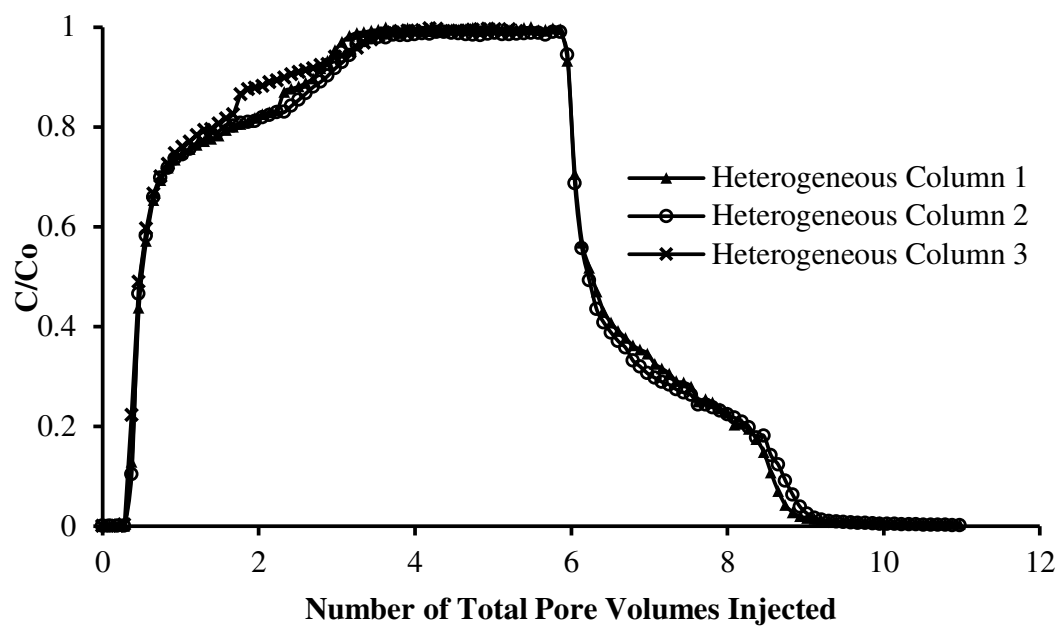


Figure 5.7: CDot tracer arrival curves for repeated heterogeneous column tests in re-loaded columns without following the air-free packing protocol.

Conclusions

Uniform and reproducible column packing is important for column studies. For wet packing of a fully saturated sand column, it is vital that dissolved air not be introduced during packing. The importance of this is clearly shown by the contrast between Figure 5.6b and 5.7. Vacuum procedures are described that assure that air is not trapped in a wet-packed column. The vacuum procedures apply to the sand and water that will fill the column and to the column after it is packed. We believe that the methods described here will be of interest in many applications where precision in column testing is desired.

Acknowledgements

The publication was based on work supported by award KUS-C1-018-02, made by King Abdullah University of Science and Technology (KAUST). We thank experts in the Cornell University Department of Biological and Environmental Engineering for advice and materials, and the Cornell University Physics Department Machine Shop for fabrication of the apparatus.

References

1. Auset, M., & Keller, A. A. (2004). Pore-scale processes that control dispersion of colloids in saturated porous media. *Water Resources Research*, 40(3).
2. Felt, E. J. (1958). Laboratory Methods of Compacting Granular Materials. *ASTM STP*, 239, 89.
3. Frimmel, F. H., Von der Kammer, F., & Flemming, H. C. (2007). *Colloidal transport in porous media*. Berlin, Heidelberg: Springer.
4. Gardner, W. H., & Klute, A. (1986). Water content. *Methods of soil analysis. Part 1. Physical and mineralogical methods*, 493-544.
5. Hausner, H. H., Roll, K. H., & Johnson, P. K. (Eds.). (1967). Vibratory Compacting: Principles and Methods. *Plenum Press, New York*.
6. Krysmann, M. J., Kelarakis, A., Dallas, P., & Giannelis, E. P. (2011). Formation mechanism of carbogenic nanoparticles with dual photoluminescence emission. *Journal of the American Chemical Society*, 134(2), 747-750.
7. Li, Y. V., Cathles, L. M., & Archer, L. A. (2014). Nanoparticle tracers in calcium carbonate porous media. *Journal of Nanoparticle Research*, 16(8), 1-14.
8. McCarthy, J. F., & McKay, L. D. (2004). Colloid transport in the subsurface. *Vadose Zone Journal*, 3(2), 326-337.

9. Niehren, S., & Kinzelbach, W. (1998). Artificial colloid tracer tests: development of a compact on-line microsphere counter and application to soil column experiments. *Journal of contaminant hydrology*, 35(1), 249-259.
10. Nimmo, J. R., & Akstin, K. C. (1988). Hydraulic conductivity of a sandy soil at low water content after compaction by various methods. *Soil Science Society of America Journal*, 52(2), 303-310.
11. Nimmo, J. R., & Miller, E. E. (1986). The temperature dependence of isothermal moisture vs. potential characteristics of soils. *Soil Science Society of America Journal*, 50(5), 1105-1113.
12. Oliviera, I. B., Demond, A. H., & Salehzadeh, A. (1996). Packing of sands for the production of homogeneous porous media. *Soil Science Society of America Journal*, 60(1), 49-53.
13. Ryan, J. N., & Elimelech, M. (1996). Colloid mobilization and transport in groundwater. *Colloids and surfaces A: Physicochemical and engineering aspects*, 107, 1-56.
14. Ripple, C. D., James, R. V., & Rubin, J. (1973). Radial particle-size segregation during packing of particulates into cylindrical containers. *Powder Technology*, 8(3), 165-175.
15. Ripple, C. D., James, R. V., & Rubin, J. (1974). Packing-Induced Radial Particle-Size Segregation: Influence on Hydrodynamic Dispersion and Water Transfer Measurements. *Soil Science Society of America Journal*, 38(2), 219-222.

16. Schiegg, H. O. (1990). Laboratory setup and results of experiments on two-dimensional multiphase flow in porous media, English translation JF McBride, DN Grahame, Rep. *PNL-7453Pac. Northwest Lab., Richland, Wash.*
17. Shosa, J. D., & Cathles, L. M. (2001). Experimental investigation of capillary blockage of two-phase flow in layered porous media. In *Petroleum Systems of Deep-Water Basins: Global and Gulf of Mexico Experience: Proceedings of the GCSSEPM Foundation, 21st Annual Bob F. Perkins Research Conference* (pp. 725-739).
18. Subramanian, S. K., Li, Y., & Cathles, L. M. (2013). Assessing preferential flow by simultaneously injecting nanoparticle and chemical tracers. *Water Resources Research*, 49(1), 29-42.
19. Topp, G. C., & Miller, E. E. (1966). Hysteretic moisture characteristics and hydraulic conductivities for glass-bead media. *Soil Science Society of America Journal*, 30(2), 156-162.
20. Wan, J., & Wilson, J. L. (1994). Colloid transport in unsaturated porous media. *Water Resources Research*, 30(4), 857-864.

CHAPTER 6

ASSESSING FLOW HETEROGENEITY IN A SINGLE NATURAL FRACTURE USING AN INERT NANOPARTICLE TRACER

Abstract:

The uniformity of fluid flow in the subsurface is important in many applications ranging from oil and geothermal energy recovery to CO₂ sequestration and radioactive waste and contaminant migration. In fractured media the simplest and most fundamental component is the uniformity of flow in a single fracture. Here this type of flow heterogeneity is assessed by injecting a mixed CDot particle tracer and CsI ionic tracer into a sub-horizontal natural fracture at Altona Flat Rock, Northern NY. The iodide and CDot tracers are both inert and pass between wells 5 to 7 meters apart without retention. The CDot concentrations in three different recovery wells are more variable than the iodide tracer. Our preliminary interpretation is that this variability reflects different flow pathways through the fracture which are less damped for the CDot tracer because of its lower diffusion constant compared to iodide. Non-uniform flow in the fracture is also indicated by shifts in tracer arrival times and broad variations in the percent of the tracer captured between different well pairs. It is also supported by the observation that well pairs with the greatest CDot concentration variation were also those with the greatest Cs⁺ tracer adsorption indicating a greater flow that could support more flow channels.

Introduction

The uniformity of fluid flow in the subsurface is important in many applications ranging from oil and geothermal energy recovery to CO₂ sequestration and radioactive waste and contaminant migration. In fractured media the simplest and most fundamental component of uniformity is the uniformity of flow in a single fracture. Here we investigate whether deploying an inert nanoparticle tracer together with an inert chemical tracer can contribute data on the uniformity of flow in a single natural fracture.

The test site is located in the William Miner Experimental Forest, Altona Flat Rocks northeastern New York, about 4 miles northwest of West Chazy, New York where a catastrophic glacial flood^{12,30,37}, uncovered the Cambrian, low porosity < 1%³², quartz rich Potsdam Sandstone. The high transmissivity sub-horizontal bedding fractures were discovered^{4,37} when a dam was constructed and leakage through the fractures precluded its use for hydroelectric power generation. Today the dam still keeps Chasm Lake filled, and this lake, located northwest of the field site provides a constant hydraulic head and steady flow through the bedding fracture (Figure 6.1). The site is ideal for tracer field tests because the natural flow flushes tracer from the fracture in a short period of time (half a day), allowing repeated tests to be run.

A five-spot pattern of 15 cm diameter wells were drilled in 2004 to penetrate a conductive sub-horizontal fracture 7.6 meters below the surface. Many experiments has been done at the site to investigate fluid-flow, solute transport, and heat exchange in fractured bedrock^{4,5,7,14,18,35,36}. Land elevation drops to the south and southeast, and water can be seen seeping out of the fracture where it outcrops at the base of a small

escarpment. The water then enters the Little Chazy River southeast of the injection site which flows northeast to Lake Champlain. Figure 6.1 shows the dam, Chasm lake, Little Chazy River that the 5 wells on the test site.

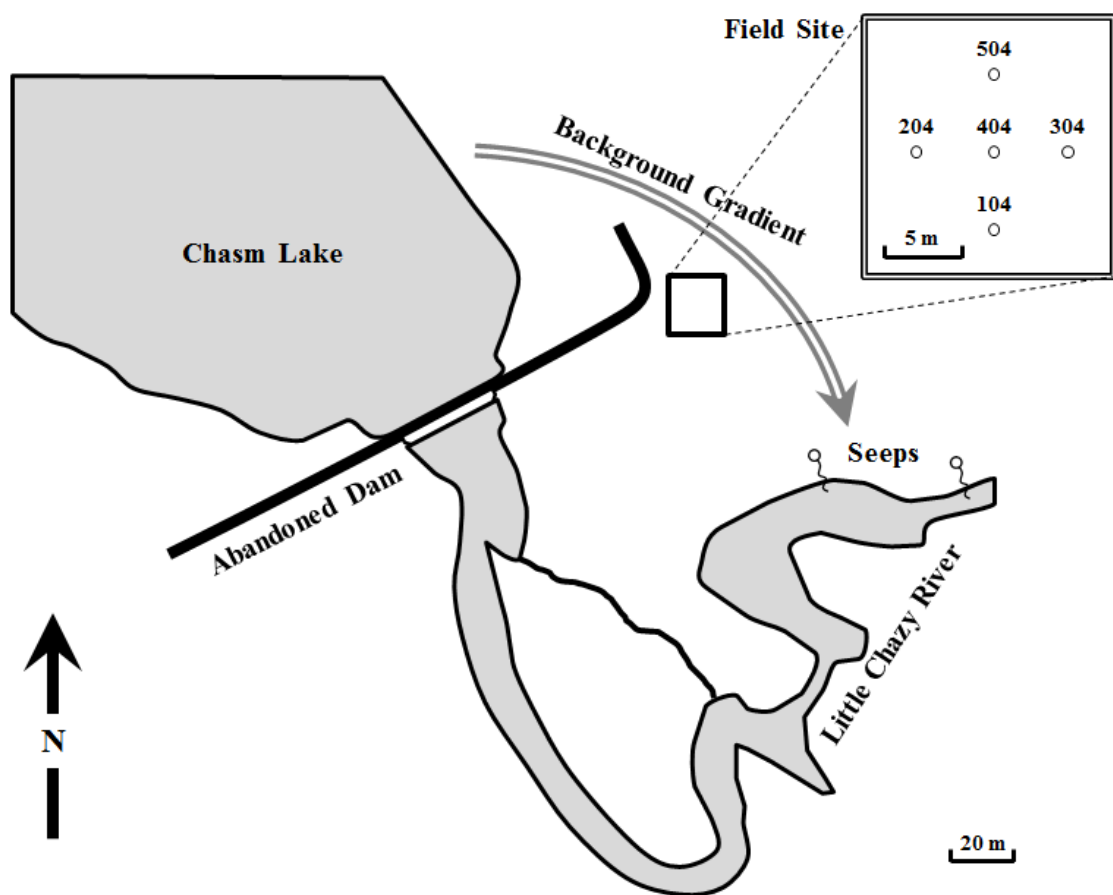


Figure 6.1: Illustrated map of experimental field site. Well number is marked on top of each of the five-spot wells. The site location is $44^{\circ}50'55.05''\text{N}$ and $73^{\circ}35'19.50''\text{W}$

This site is ideal for testing a CDot nanoparticle tracer we have recently developed. Our purpose was twofold: First, although we have demonstrated the inertness (non-sticking properties) of this tracer in the laboratory^{25,34} and in a field experiment in carbonate²², we wanted to evaluate tracer inertness in the field under tightly controlled conditions. Second, we wanted to see if the low diffusion of the nanoparticle tracer in combination with the higher diffusion of an inert chemical tracer could provide information on the heterogeneity of flow in the Altona fracture.

The CDot nanoparticle tracer consists of a carbon core decorated with highly fluorescent polymer. The particles are synthesized in a one-step process from citric acid and ethanolamine²⁴. The 3-5 nm diameter particles are highly water soluble, inert (do not stick to sand or carbonate²⁵), and detectable by their fluorescence to ~10 ppb concentrations. Similar carbon-cored particles have been developed for medical applications where they have been demonstrated to have very low toxicity^{1,29,38,39}.

Because of this we were able to obtain permission from the NYSDEC and the USEPA to run the field tests at the Altona site.

The inert chemical tracer we deployed in conjunction with the CDot tracer was CsI, commercially obtained from Sigma-Aldrich. The I portion of this tracer is inert, but the Cs portion slowly adsorbs to the crack surfaces, providing a measure of the crack surface area contacted^{4,10}. Iodide has been widely used as ionic tracers for subsurface fluid flow studies^{3,9,26}.

Field scaled colloid-size (0.1 to 5 microns) particle transport experiments have been carried out in natural formations. These include bacteria, viruses, natural and synthetic colloids, engineered nanoparticles, fluorescent dyes, and microspheres

decorated with fluorescent molecules^{2,3,6,8,11,15,16,23,26,27,31}. Due to poor tracer stability, unfavorable size, and complicated interactions, the particles have not been useful as tracers in subsurface applications. Only a very few nanoparticle tracer field with inert particles have been reported^{8,22}.

Materials and Methods

The wells at the site shown in Figure 6.1 were originally drilled to 12.2 meters deep and deepened to explore more conductive fractures at greater depths in 2011¹⁷. The present depths of the wells are listed as table 6.1:

Table 6.1: New depths of five-spot wells.

Well Number	Total Depth (meters)
104	18.3
204	21
304	21.3
404	20.1
505	20.4

Pneumatic packers are employed to isolate the test fracture. A capped, perforated stainless steel pipe is run into the well with packers on each side of the perforations. The packers are inflated to 30 psi on either side of the crack, and the integrity of the sealing is tested by inducing a hydraulic head and measuring water level response. The stainless steel pipe allows fluids to be injected or recovered from the fracture. A temperature and pressure logger is immersed in each of the wells for the duration of the experiment. A separate barologger was placed roughly 25 meters away from the well site to record barometric pressure. The sampling times of all these loggers are calibrated with Levelogger® software before and after the field tests. The packers are pumped with a Grundfos Rediflow-2 submersible electrical pump. The entire assembly is deflated, moved, and re-inflated for experiments involving different well pairs. Injection and production in the well pairs is at the same rate.

A mixture of CDot particle tracer and CsI ionic tracer are injected together. Effluent tracer samples are collected in a waxy plastic bottle at the producing well. Samples are labeled, stored in the trunk of a van and transported to storage every day. At the end of ~3 weeks of field work, the samples were transported to our laboratory at Cornell. The samples were exposed to room lighting conditions between their sampling and analysis at Cornell.

The concentration of the CDot nanoparticle tracer was determined at Cornell by the fluorescence of the solution, measured using a spectrofluorimeter (SpectraMax M2e, Molecular Devices, Sunnyvale, CA, USA). The optimum excitation wavelength was 358 nm and the emission peak at this excitation is 460 nm. Known concentration CDot standards were prepared and calibration curves determined prior to each set of

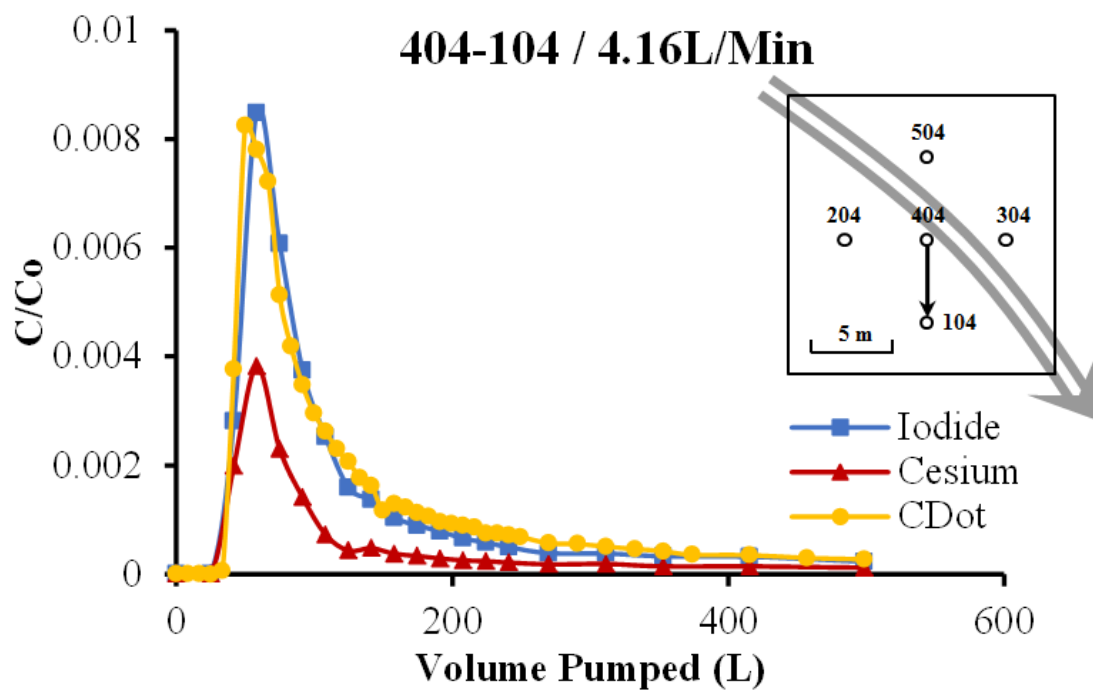
experiments. The CDot concentrations of effluent samples were calculated using this calibration curve. CDot concentration is linear below 50 ppm, and the detection limit of CDot in Altona ground water is ~50 ppb. The sample fluorescence was corrected for photo bleaching as described in the supplementary material.

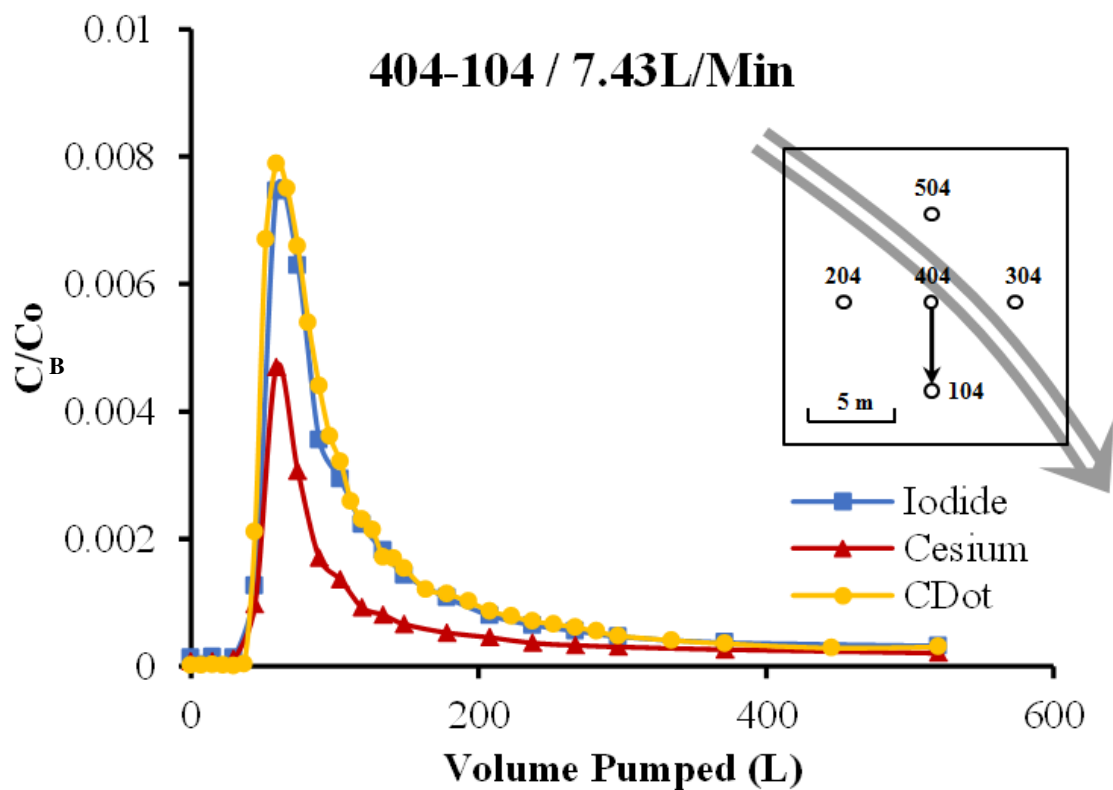
The concentration of ionic tracer Cs^+ and I^- was determined by inductively coupled plasma mass spectrometry (Element 2TM ICP-MS, Thermo Fisher Scientific Inc., MA USA). Standard curves for Cs^+ and I^- are prepared and used to determine the concentration of samples. Samples were diluted to acceptable concentration range. The detection limit for Cs^+ and I^- is ~ 200 ppt.

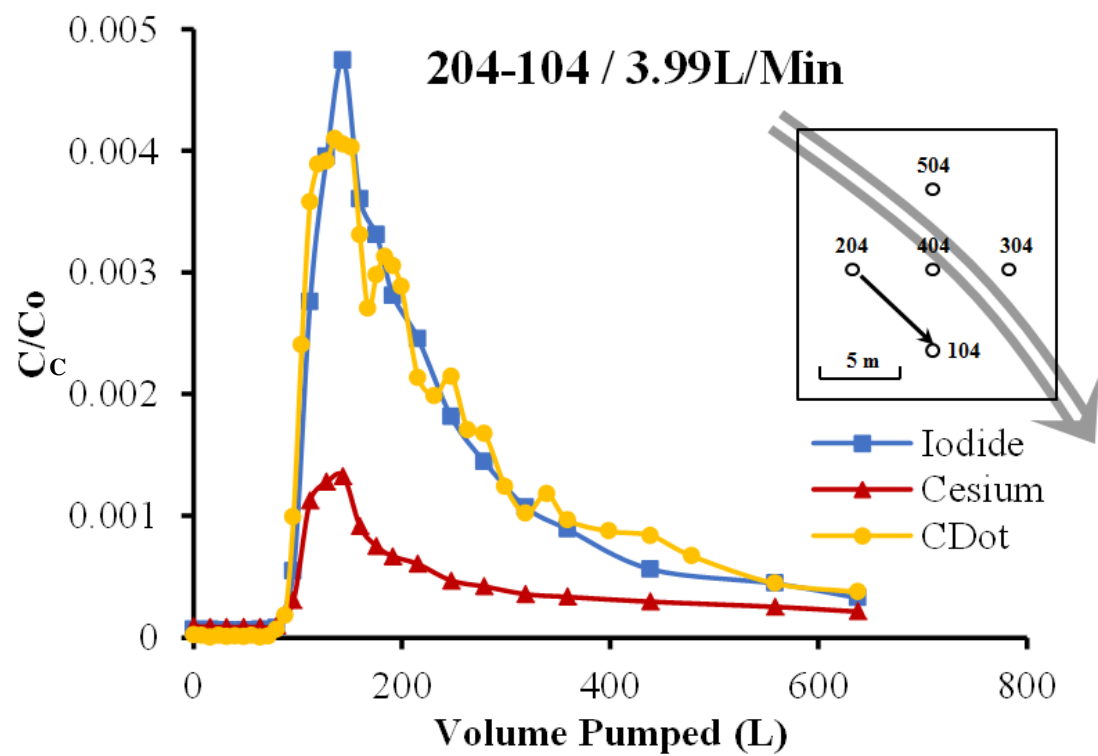
Results and Discussions

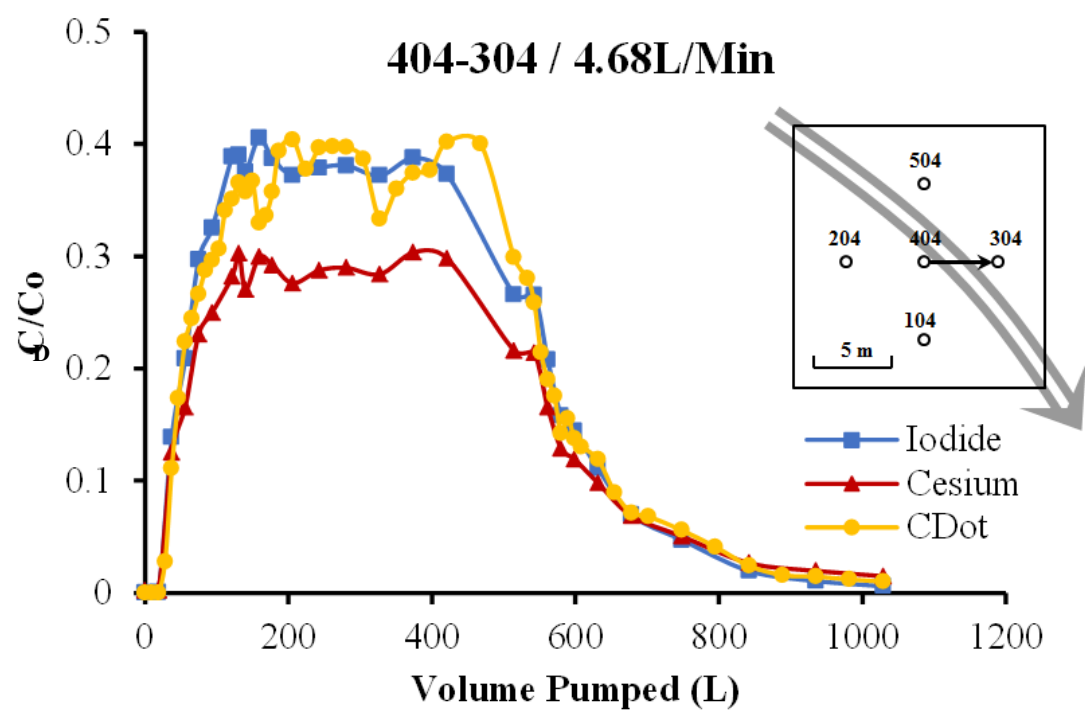
The tracer arrival curves are shown in Figure 6.2. The insert shows the well pair active in each test.

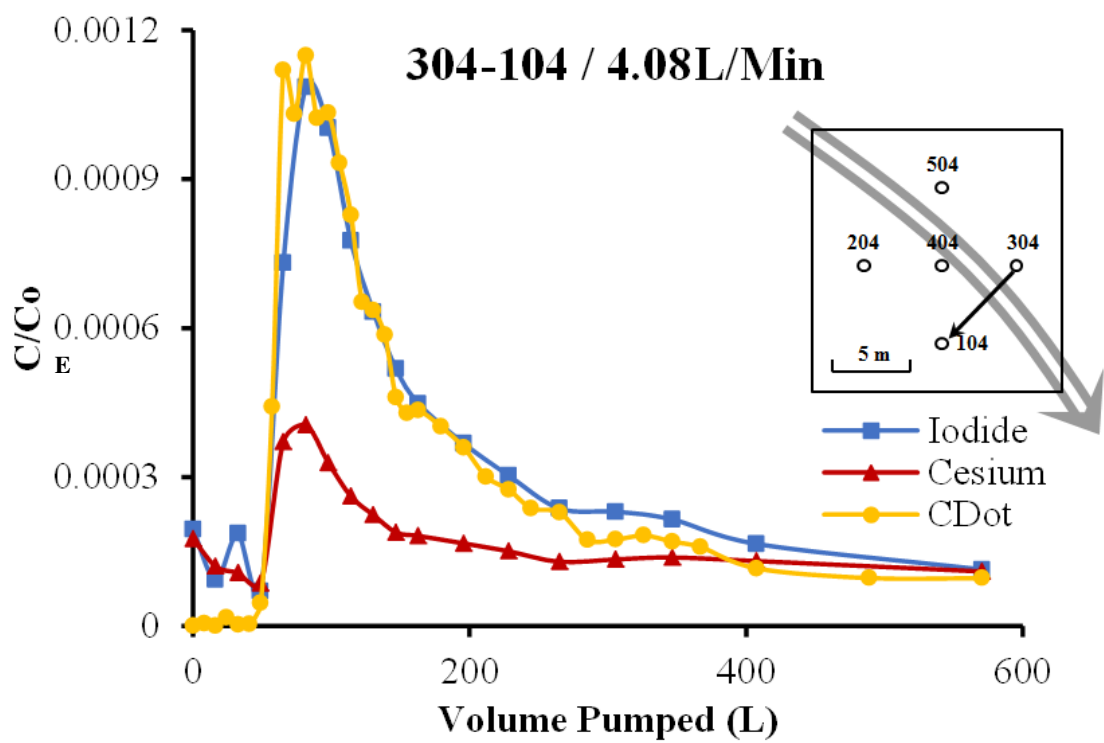
Figure 6.2: Combination tracer arrival curve. Blue solid squares indicate the breakthrough curve of the inert iodide chemical tracer, red triangles the sorbing cesium chemical tracer, and solid yellow circles the CDot nanoparticle tracer. The abscissa is the total volume pumped, and the ordinate is the normalized effluent concentration C/C_0 . The insert shows the test site, a solid black arrow indicates the flow from the injection to the production well, and a large gray arrow indicates the presumed background flow direction. The injection and production rate and the well pair is given above each plot.











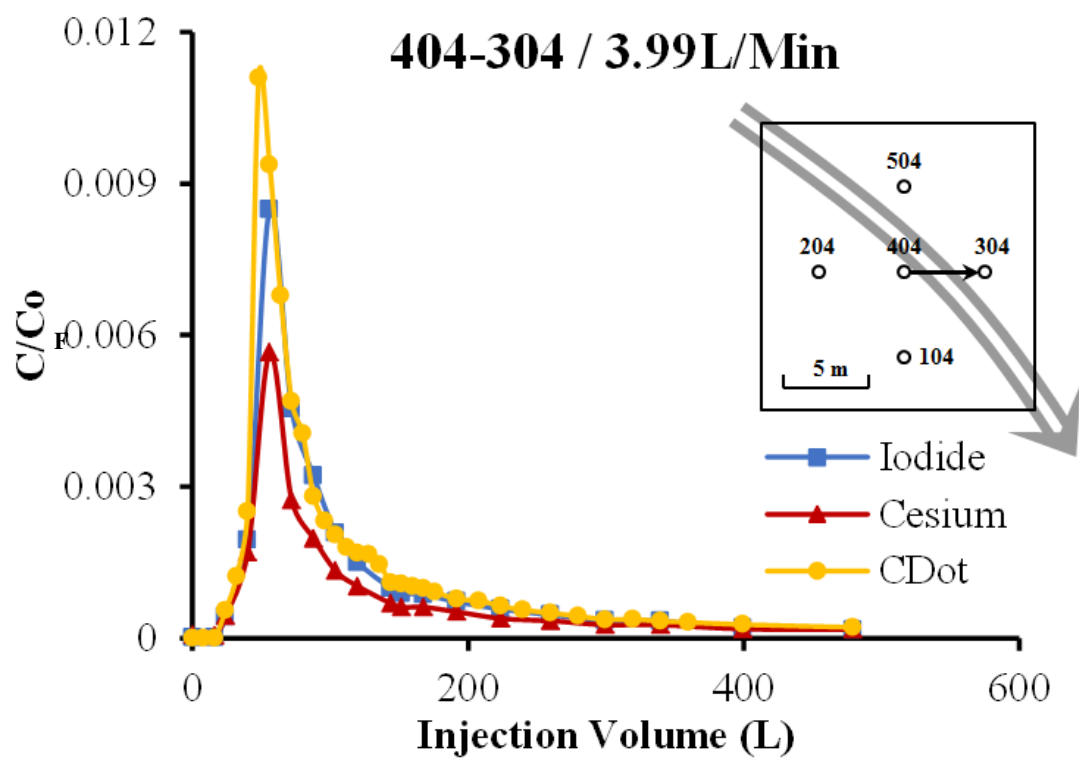


Figure 6.2 shows that the CDot and iodide tracers behaved similarly in the 6 different well pair experiments. Since iodide is known to be an inert tracer, this indicates that the CDots are also an inert tracer. The inertness of the CDot tracer is thus verified. The similarity of the two curves also indicates that, as might be expected, there is very little diffusion of iodide away from the fracture into the quartzite matrix. The quartzite has very low porosity < 1%^{32,37} and the diffusion of the chemical tracer into it from the fracture, measured at $\sim 6 \times 10^{-9} \text{ cm}^2 \text{ s}^{-1}$ is negligible.

The CDot breakthrough curves are erratic compared to those of the iodide tracer (most pronouncedly Figure 6.2C, 6.2D, and 6.2E). Furthermore the CDot curves for the well pairs that show the greatest Cs^+ adsorption tend to be the most erratic. Our preliminary interpretation is that the erratic nature of the tracer recovery reflects the arrival of different flow pathways through the fracture. Diffusional mixing between these pathways is greater for the more diffusive iodide tracer and this smoothes its concentration variations more than those of the less diffusive CDot tracer. The flow between well pairs with greater Cs^+ adsorption occurs through a greater area, and this provides opportunity for more flow pathways and more variations in recovered tracer concentration, as observed.

This idea is explored with a potential flow model illustrated in Figures 6.3. Steady state flow from well 204 to 104 is calculated along a selection of 64 streamlines assuming a constant background gradient and constant fracture aperture by methods presented in the supplemental material. Tracer breakthrough is calculated in each streamline with advection-dispersion equation¹³. The regional flux in the crack is 0.02

m/min to the east and 0.02 m/min to the south. The aperture is 1.9 mm, and the injection and production rates are 3.99 L/Min.

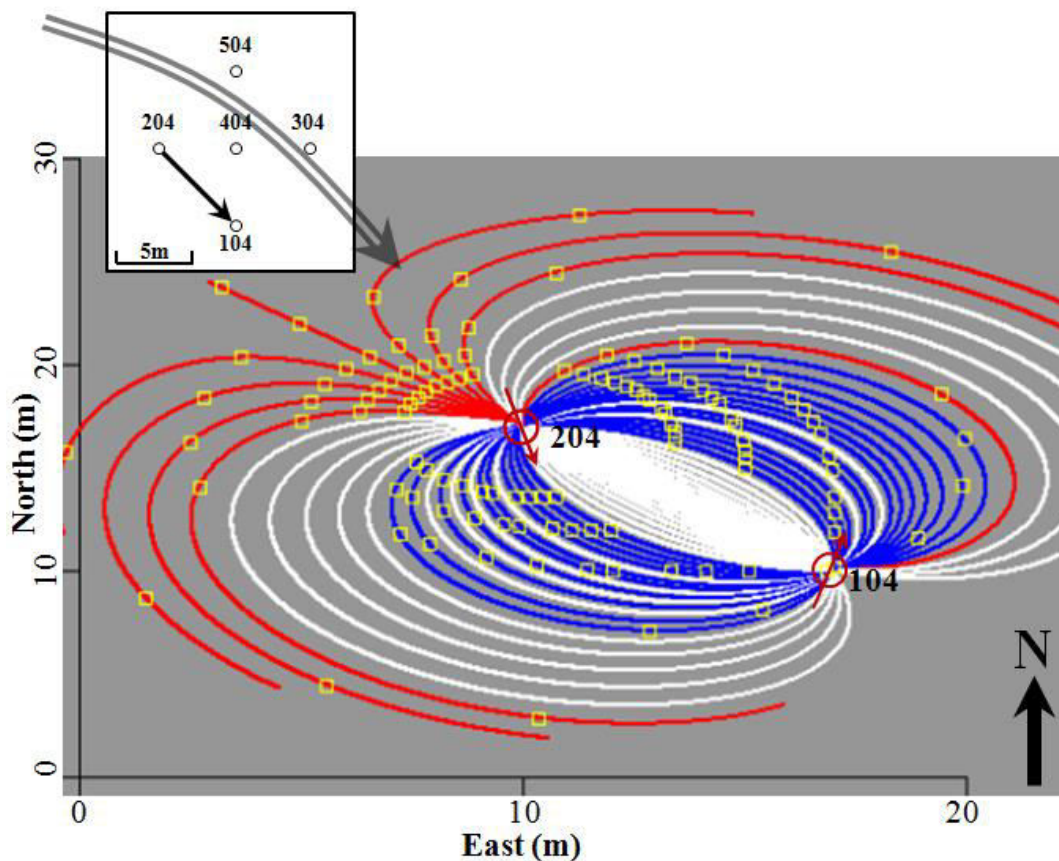


Figure 6.3: Streamline model for injection into well 204 and production from well 104. Blue streamlines connect the injection and production wells and transmit tracer between the wells in the experiment period. Flow along red streamlines is slow enough that tracer is not transmitted to the production well in the experiment period. White streamlines are the streamlines that have been turned off and their flow allocated to the remaining active streamlines. Yellow squares so the position of the tracer front at regular time intervals. Directly connected streamlines are disabled because GPR data from previous salt tracer tests indicated poor direct connection between well 204 and 104 and a flow pattern similar to that shown⁴. The insert is as described in Figure 6.2.

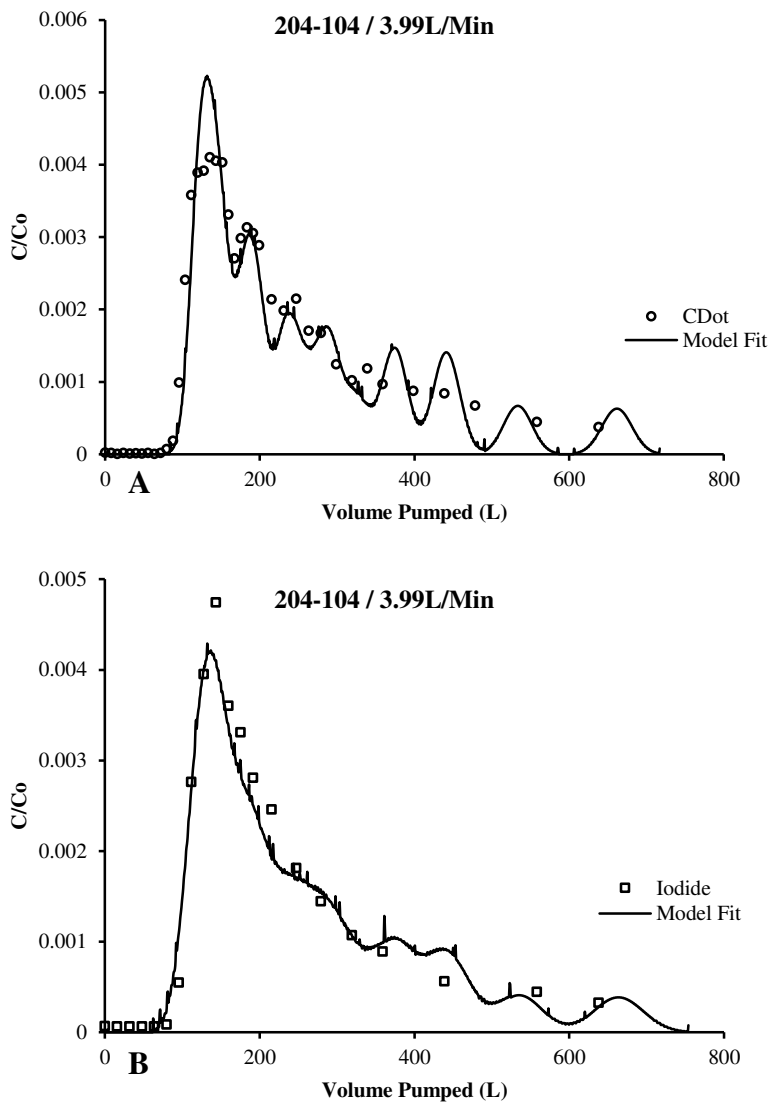


Figure 6.4: Comparison of observed and simulated (solid lines) tracer concentrations for the streamline flow from well 204 to well 104 shown in Figure 6.3. The sole difference between the theoretical curves in (A) and (B) is the value of the longitudinal dispersion constant, a_L , used in the advective-dispersion equation. (A) is the model's prediction for less diffusive CDot nanoparticle tracer and $a_L=1.5$ m, and (B) is that for more diffusive iodide tracer and $a_L=4$ m.

Figure 6.4 compares the calculated and observed arrival curves for the CDot and iodide tracers. The difference in the two calculated curves is only the value of the longitudinal dispersion coefficient, a_L , used in the advective dispersion equation. For the CDot tracer $a_L = 1.5$ m, and for the iodide tracer $a_L = 4$ m. The bumps in the arrival curve indicate the arrival of tracer transmitted by different streamlines.

The suggestion in Figure 6.3 and 6.4 that flow in the Altona fracture occurs in channels (proxied by selected streamlines) is supported by other observations on the transmission of tracer between the well pairs shown in Figure 6.4. The most striking evidence is that the tracer capture ranges from 15 to 78%, as shown in Table 6.2. Some well pairs are much more directly connected than others. As Figure 6.5 shows, with the constant aperture assumption, only the arrival curve of the most directly connected well pairs are predicted, any well pairs with very slight complications will result a huge disagreement (Figure 6.5d, e, f). If the first well pair in Figure 6.2 is modeled for the conditions of that test and then applied to the other wells, it can be seen that the arrival times for the different tests require very different numbers of connecting streamlines and/or fracture aperture. Flow in the single Altona Flat Rock fracture is clearly channelized and anything but uniform.

Figure 6.5: Model prediction (black dashed line) of all 6 well pairs with the parameter used to fit the directly connected cases (a, b and c). All the 64 streamlines are active, there is no background flow added to this base case, the aperture used is 1 mm, and the dispersion constant used is 1 m. The insert shows the test site, and is described in Figure 6.2.

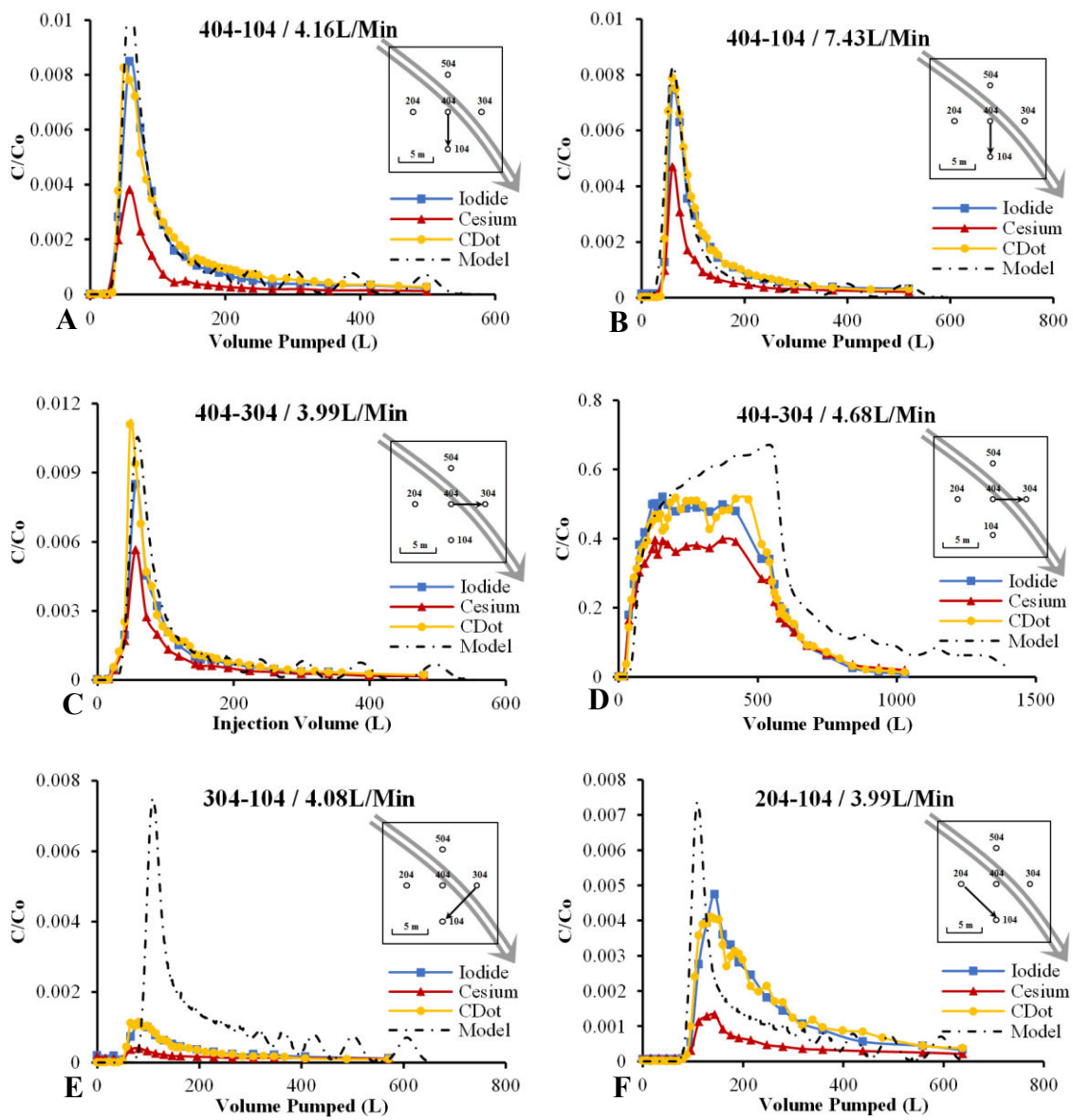


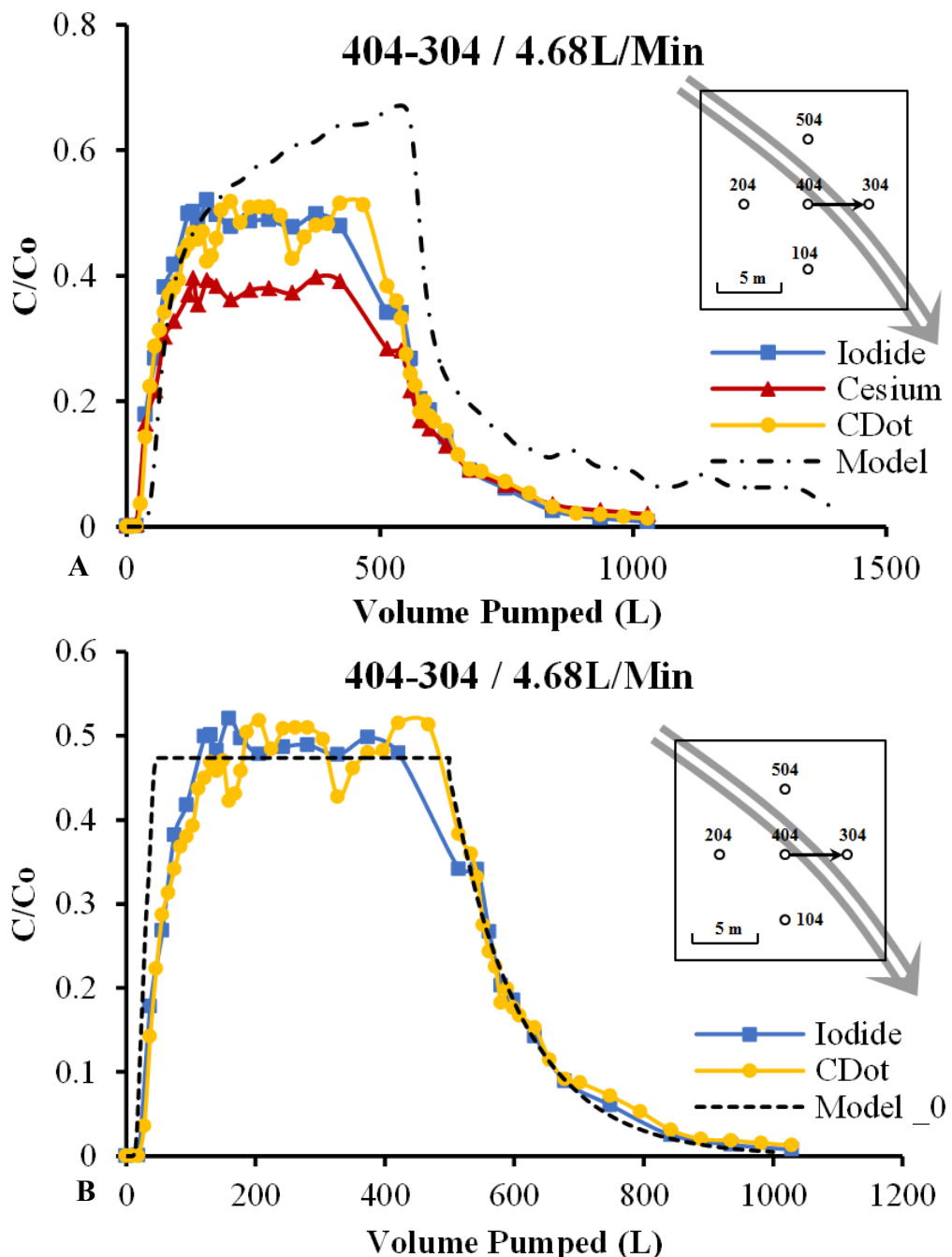
Table 6.2: Tabulated mass balance for all well pairs dual tracer tests.

Well Pair	Injection Rate (L/Min)	Mass Injected (M_i)			Mass Recovered (M_r)			Recovery = M_r/M_i		
		Cs^+	Γ	CDot	Cs^+	Γ	CDot	Cs^+	Γ	CDot
404-304	3.99	5.13	4.90	5.09	1.83	2.51	3.03	35.62%	51.26%	59.56%
404-304	4.68	15.8	15.09	39	5.74	6.84	17.60	36.31%	45.30%	45.13%
404-104	4.16	2.77	2.64	12.3	0.70	1.58	7.93	25.22%	59.89%	64.60%
404-104	7.43	2.65	2.53	12.3	0.87	1.51	7.85	32.97%	59.79%	63.96%
304-104	4.08	2.42	2.32	10.2	0.22	0.41	1.62	9.16%	17.53%	15.88%
204-104	3.99	2.42	2.32	12.3	0.62	1.74	9.65	25.57%	75.03%	78.61%

Physically, flow along a fracture channel could produce the differences in the smoothness of the CDot and iodide tracer arrival curves if flow along the channel induced parallel flow adjacent to it. Flow entering the adjacent channel and moving more slowly along it would take tracer from the upstream part of the main channel and replace it, until the tracer in the main channel arrived, with tracer-free pore water further downstream where the adjacent channel rejoins the main channel. If tracer diffuses quickly into the adjacent channel, the dilution will be diminished. Thus, the concentration of non-diffusive particles will be more affected by this parallel flow than will a diffusive chemical tracer.

The misfit between prediction and observation as shown in Figure 6.5 d, e and f indicated that the flow in this fracture is not very uniform. The capability of turning on and off streamlines and adding in different degree of background gradients gives us a simple tool to explain our observations. A case is shown as Figure 6.6 where tracers are injected from well 404 and produced at well 304. ~470L of tracer solution was injected in a step fashion. The flat peaked arrival curve indicated that there are very direct flows in between these two wells, and no late arriving streamlines because if there is we would expect the arrival curve to ramp up with injection.

Figure 6.6: Model fit for well pair 404-304 step test. Yellow line is CDot data, blue line is iodide data, red line is cesium data, and black dashed line is the model fit. (A), is the base case (no background flow, 1 mm aperture, 1 m dispersion constant) where agreed with direct connected wells (Figure 6.5 a, b, c); (B) is the case with all arriving streamlines turned off except for 6, with no background flow; (C) is the case with 11 incoming streamlines remaining, and 0.1 m/min eastward and southward background flow; (D) is the case with 16 incoming streamlines on, and 0.2 m/min eastward and southward background flow. The insert shows the test site, and is described in Figure 6.2.



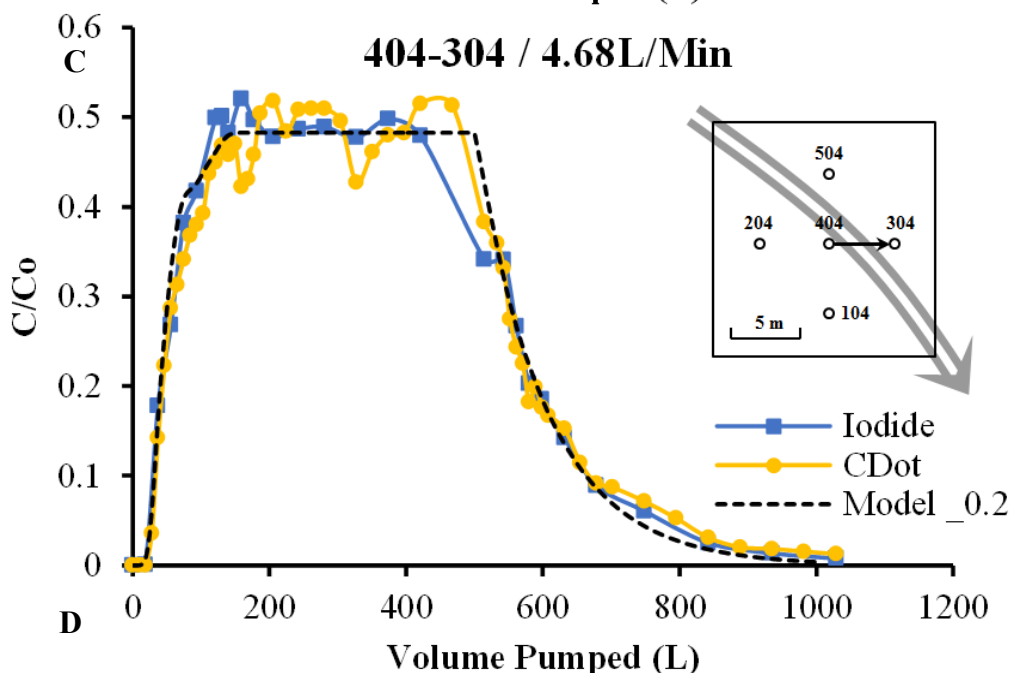
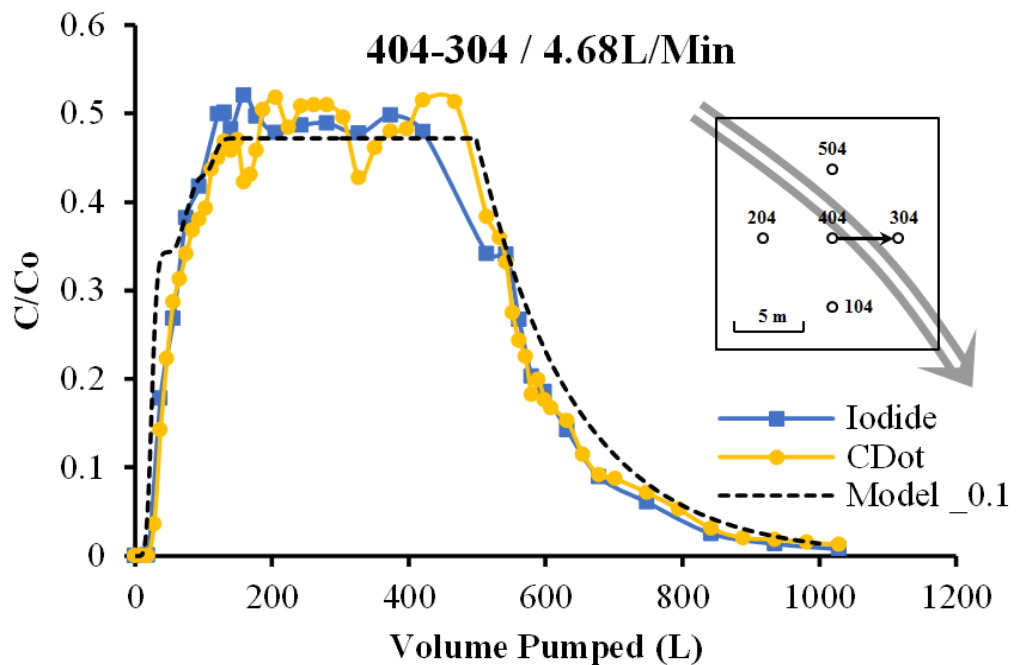


Figure 6.6 above showed how complications in the subsurface can be explained with this simple streamline model. However we do need to give more constraints on the parameters, such as the intensity of background flow, and aperture thickness to make this model more realistically reflect what is really happening in the subsurface.

The longitudinal dispersion constant provides a convenient way to mathematically capture this effect for a short duration pulse (Figure 6.4). However, this model would not produce concentration variability for the step tracer injection case shown in Figure 6.2D. For a long-duration tracer step test, individual streamlines would not contribute pulses of tracer separated enough in time to produce variable tracer concentrations in the recovered fluids. Concentration variations along a single channel streamline of the kind described in the previous paragraphs would produce such variability, however, even for a long duration step tracer injection. The models shown in Figure 6.4 are thus only illustrative. A more powerful model with a realistic aperture field which can predict the entire data set remains to be constructed and demonstrated.

Conclusion

A dual-tracer field scaled experiment was performed in Altona Flat Rock field site where a five-spot well pattern intersects a sub-horizontal fracture in impermeable and very low porosity quartzite. The CDot tracer behaves like the inert chemical iodide tracer in all 6 well pair experiments (Figure 6.4). On this basis we conclude the CDot tracer is inert (non-interacting with the fracture surface just as is the iodide tracer). The CDot recovery curve has larger (but similar) variations in concentration than the iodide recovery curve, especially in well pairs 204-104, 404-304, and 304-104. We argue that this reflects flow channeling in the sub-horizontal bedding fracture and this is supported by deviations from base predictions of arrival times in the different well combinations and in their very different tracer recoveries. The concentration variations were greater when the Cs⁺ was more adsorbed indicating a more spread out flow that could support more flow channels.

Acknowledgements

This material is based upon work supported by the National Science Foundation Graduate Research Fellowship under Grant No. (0966045). We thank Dominic Fontana of NYSDEC and Norma Ortega of USEPA for assistance in permitting this field test. We also thank Stephan Kramer of The William H. Miner Agricultural Research Institute for accommodating this field test. We also thank Gregg McElwee and Caryl Mansing for assistance in this project.

Supplementary Materials

Photobleaching

Initially we thought photo bleaching would be small and we made no correction for it.

The exposure of sunlight was not severe and with the protection of waxy bottles it was originally thought to be enough to protect the samples from photobleaching. We found, however, that the CDot tracer concentrations were less than the inert chemical tracer Iodide, as if the CDots were adsorbing, but the drop in CDot concentration was not proportional to the Cesium drop, but rather was a constant fraction of the inert tracer Iodide concentration. For this reason, and also because a decrease in sample fluorescence was suspected from field measurements, we suspected that photo bleaching might the reason for the apparent drop in CDot concentration relative to the iodide tracer. Extensive photobleaching or poor photostability of CDot nanoparticles had not previously been reported in other CDot studies including field tests^{21,22}.

To confirm the fluorescence loss of our field sample is due to photobleaching, a simple laboratory CDot photobleaching experiment was conducted. A fresh 1 gallon batch of 100ppm CDot solution was prepared and divided to two identical glass bottles, one of which was placed on a window sill with strong sunlight exposure and periodically sampled and analyzed over a 50 day period, and the other was kept in dark. The fluorescence intensity of CDot window sill solution is plotted against time in days in Figure 6.S1.

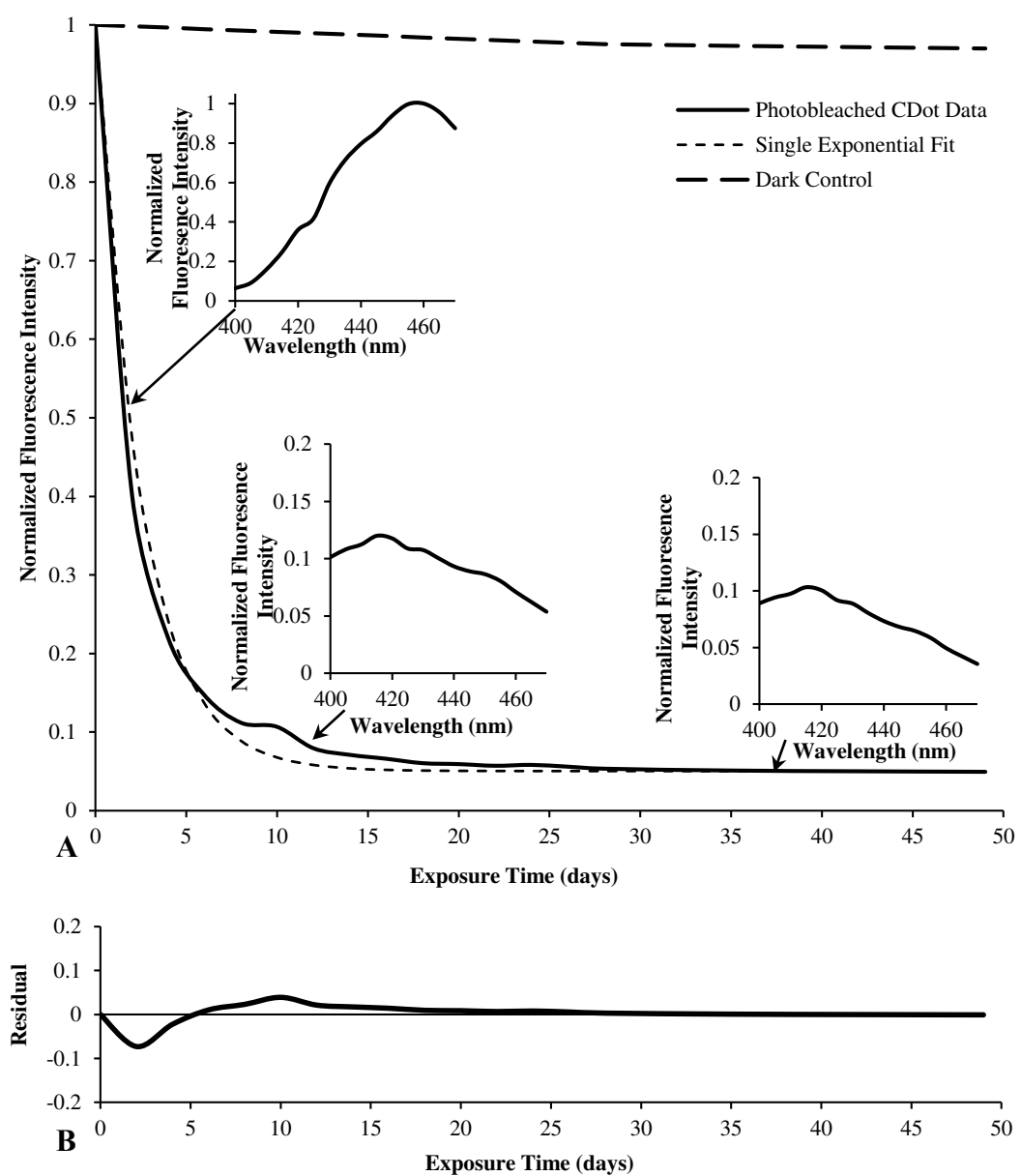


Figure 6.S1: a) CDot photobleaching profile. Solid line is the measured CDot fluorescence intensity. Samples were taken every other day at first and after a month once a week. The dashed line is exponential fit with a decay rate of 0.4 per day to a terminal intensity of ~5% of the intensity at $t=0$. Long dashed-line is the fluorescence intensity of CDot sample kept in the dark. Subplots are the emission profiles of CDot at the times indicated. They show the peak emission wavelength shifts from 460 nm to 415 nm. b) The residual plot showing the difference between observed fluorescence and the exponential curve.

Figure 6.S1 shows that the CDot solution kept in the dark has remained at ~96% of its original intensity while the exposed CDot solution intensity decreased exponentially to ~5% of its initial value in a month. The fact that CDot tracer photobleaching plateaus, and that the peak emission wavelength has shifted from 460nm to ~415nm suggests that the source of the fluorescence has changed. It has been previously documented that both of CDot carbon core and polymer hairs fluoresces²⁴, it could be that the core is protected from fluorescence destruction. The photostability of the CDots will be studied in subsequent experiments. Variations in photobleaching rates related to particle collisions and therefore CDot concentration are possible but considered to be very small because the particles are dialyzed during synthesis (and thus lack small colliding fragments) and all the samples are very dilute.

To correct the measurements for photobleaching, a photobleaching experiment was then done on a sample of solution that was injected in the field at 83 ppm CDots. This sample was analyzed for 40 days starting 40 days after the field test, as shown in Figure 6.S2. Between the field test and the start of measurement 40 days later, the sample has been mostly stored on a bench in the laboratory. Prior to this the sample had been stored in warehouse in Altona with lighting similar to that in the laboratory at Cornell. The initial fluorescence intensity at day 0 (the first data point in Figure 6.S2) was measured on a newly prepared sample of 83 ppm CDot. A single exponential fit to the CDot fluorescence intensity data (all the open diamonds in Figure 6.S2) indicates an exponential decay to the fluorescence intensity plateau determined in the first experiment (Figure 6.S1) with a decay constant of 0.0165 per

day. This decay rate is then used to correct concentrations determined from fluorescence intensity for photobleaching as shown in Table 6.S1.

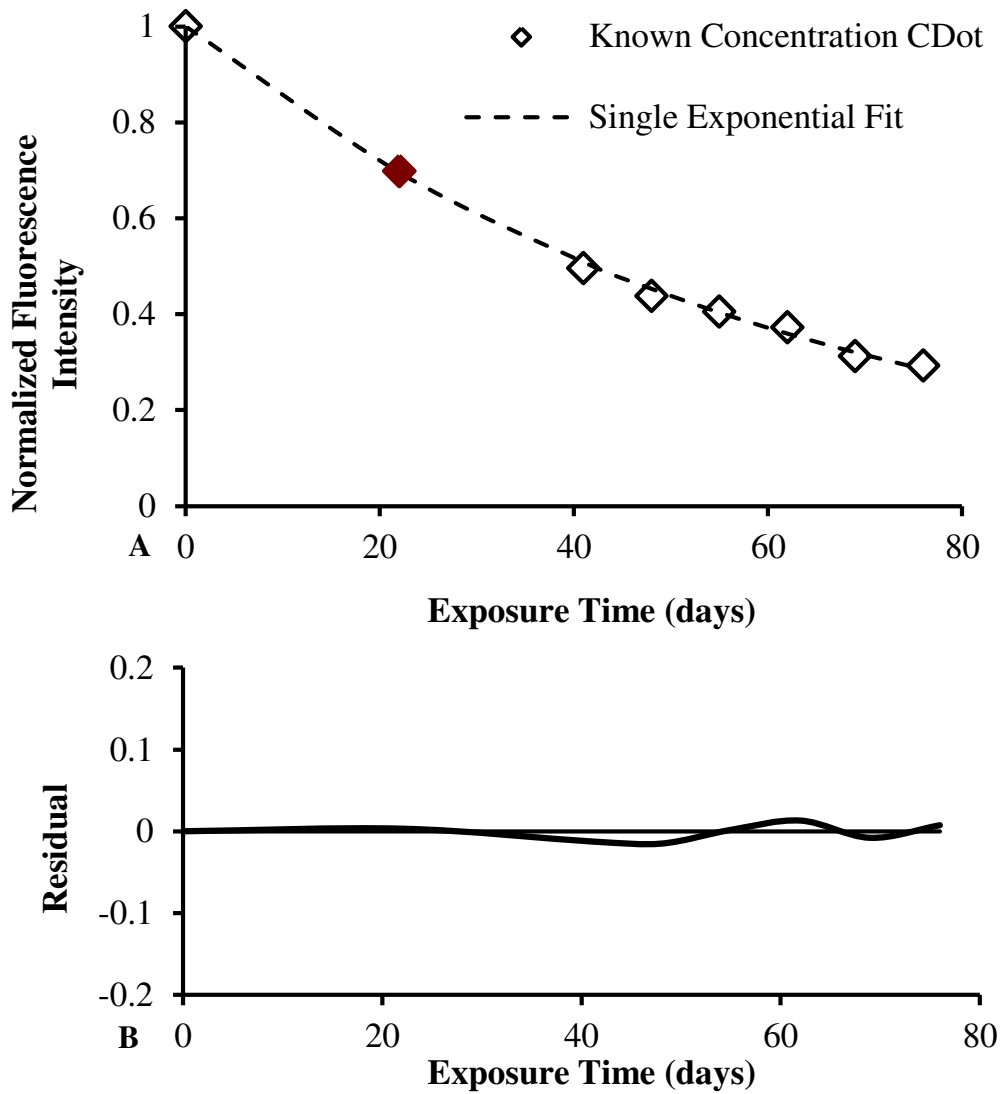


Figure 6.S2: a) CDot photobleaching profile under room condition lighting exposure. Hollow diamonds is the fluorescence intensities of an 85 ppm field sample. Dashed line is the fitting of a single exponential function with a decay rate of 0.0165 per day and the plateauing constant determined from the previous experiment. Red solid diamond is a corrected value on the sample after room condition light exposure of 21 days.

Table 6.S1: Correcting factors for different well pairs.

Experiment Number	well pair	Injection Rate (L/Min)	Exposure Time (Days)	Correcting Factor	Test Type
1	404-304	3.99	21	1.41	Slug
2	404-304	4.68	22	1.44	Step
3	404-104	4.16	18	1.35	Slug
4	404-104	7.42	18	1.35	Slug
5	304-104	4.07	20	1.39	Slug
6	204-104	3.99	20	1.39	Slug

Tracer Modeling

Steady flow between wells into which fluid is being injected into a uniform crack of width b at a rate Q_i [m³/s] can be described as:

$$\begin{aligned} \hat{x} & \left(v_x + \sum_{i=1}^n \frac{Q_i}{2\pi b} \frac{(x - x_i)}{[(x - x_i)^2 + (y - y_i)^2]} \right) + \\ \hat{y} & \left(v_y + \sum_{i=1}^n \frac{Q_i}{2\pi b} \frac{(y - y_i)}{[(x - x_i)^2 + (y - y_i)^2]} \right) \end{aligned} \quad 6.SB1$$

Here \bar{v} is the true average velocity of the fluid in the crack, v_x and v_y are the eastward and northward natural flow of fluid in the crack. Streamline are determined by starting near the injection well and stepping incrementally toward the production well, calculating the flow velocity at each point using eq. 6.SB1. The methods are described in Javandel et al.²⁰.

The tracer concentration is calculated from the advection diffusion equation¹³ as a function of time relative to the piston-flow arrival of tracer in a streamline at t_0 .

$$C/C_0(t) = \frac{1}{2} \left(1 - \operatorname{erf} \frac{1 - t/t_0}{\sqrt{4P_D t/t_0}} \right); \quad P_D = \frac{D^* + \alpha_L \bar{v}}{l \bar{v}} \quad 6.SB2$$

Here t is time (positive or negative) relative to the piston-flow arrival of tracer at t_0 (so elapsed time since the start of tracer injection is $t_0 + t$). D^* is the aqueous diffusion constant in m²/s, α_L is the longitudinal dispersion in m, l is the length of the streamline from injection to recovery well, and \bar{v} is the average velocity of flow along the streamline.

The tracer recovery curve is obtained by summing the tracer concentration of all streamlines using eq. 6.SB2

References

1. Baker, S. N., & Baker, G. A. (2010). Luminescent carbon nanodots: emergent nanolights. *Angewandte Chemie International Edition*, 49(38), 6726-6744.
2. Bales, R. C., Hinkle, S. R., Kroeger, T. W., Stocking, K., & Gerba, C. P. (1991). Bacteriophage adsorption during transport through porous media: Chemical perturbations and reversibility. *Environmental Science & Technology*, 25(12), 2088-2095.
3. Becker, M. W., Reimus, P. W., & Vilks, P. (1999). Transport and Attenuation of Carboxylate-Modified Latex Microspheres in Fractured Rock Laboratory and Field Tracer Tests. *Groundwater*, 37(3), 387-395.
4. Becker, M. W., Remmen, K., Reimus, P. W., & Tsolias, G. P. (2013). Investigating well connectivity using ionic tracers. In *Proceedings, Thirty-Eighth Workshop on Geothermal Reservoir Engineering, Stanford: Stanford University*.
5. Becker, M. W., & Tsolias, G. P. (2010). Comparing flux-averaged and resident concentration in a fractured bedrock using ground penetrating radar. *Water Resources Research*, 46(9).
6. Bhattacharjee, S., Ryan, J. N., & Elimelech, M. (2002). Virus transport in physically and geochemically heterogeneous subsurface porous media. *Journal of contaminant hydrology*, 57(3), 161-187.

7. Castagna, M., Becker, M. W., & Bellin, A. (2011). Joint estimation of transmissivity and storativity in a bedrock fracture. *Water Resources Research*, 47(9).
8. Cathles, L., Spedden, H., & Malouf, E. (1974). A tracer technique to measure the diffusional accessibility of matrix block mineralization. *Am. Inst. Mining, 103rd Annu. Meet.*
9. Davis, J. A., & Fox, P. M. (2009). Redox and Sorption Reactions of Iodine and Cesium during Transport through Aquifer Sediments. US Nuclear Regulatory Commission, Office of Nuclear Regulatory Research.
10. Dean, C., Reimus, P., & Newell, D. (2012). Evaluation of a cation exchanging tracer to interrogate fracture surface area in EGS systems. In *Proceedings of the 37th Workshop on Geothermal Reservoir Engineering*.
11. Fontes, D. E., Mills, A. L., Hornberger, G. M., & Herman, J. S. (1991). Physical and chemical factors influencing transport of microorganisms through porous media. *Applied and Environmental Microbiology*, 57(9), 2473-2481.
12. Franzi, D. A., Rayburn, J. A., Yansa, C. H., & Knuepfer, P. N. K. (2002). Late Wisconsinan lacustrine and marine history of the Champlain Lowland and its paleoclimate implications. In *Joint meeting of the New England Intercollegiate Geological Conference (94th Annual Meeting) and New York Geological Society (74th Annual Meeting)* (p. A5).

13. Freeze, R. A., & Cherry, J. A. (1979). *Groundwater*, 1979. Prentice-Hall, New Jersey.
14. Guiltinan, E. J., & Becker, M. (2010, May). Using harmonic hydraulic tests to estimate fractured bedrock properties and predict local heterogeneity. In *Abstracts with Programs-Geological Society of America* (Vol. 42, No. 4, p. 110).
15. Harvey, R. W. (1997). Microorganisms as tracers in groundwater injection and recovery experiments: a review. *FEMS Microbiology Reviews*, 20(3-4), 461-472.
16. Harvey, R. W., Kinner, N. E., MacDonald, D., Metge, D. W., & Bunn, A. (1993). Role of physical heterogeneity in the interpretation of small-scale laboratory and field observations of bacteria, microbial-sized microsphere, and bromide transport through aquifer sediments. *Water Resources Research*, 29(8), 2713-2721.
17. Hawkins, A. J., (2013). *Measurement of the spatial distribution of heat exchange in a geothermal analog bedrock site using fiber-optic distributed temperature sensing*. (Unpublished Thesis). California State University Long Beach.
18. Hawkins, A. J., & Becker, M. W. (2012). Measurement of the Spatial Distribution of Heat Exchange in a Geothermal Analog Bedrock Site Using Fiber Optic Distributed Temperature Sensing. In *Proceedings Thirty-Seventh Workshop on Geothermal Reservoir Engineering, Stanford, California, January*.

19. Kanel, S. R., Nepal, D., Manning, B., & Choi, H. (2007). Transport of surface-modified iron nanoparticle in porous media and application to arsenic (III) remediation. *Journal of Nanoparticle Research*, 9(5), 725-735.
20. Javandel, I., Doughty, C., & Tsang, C. F. (1984). *Groundwater transport: handbook of mathematical models* (Vol. 10, pp. 1-228). American Geophysical Union.
21. Kanj, M. Y., Funk, J. J., & Al-Yousif, Z. (2009, January). Nanofluid coreflood experiments in the ARAB-D. In *SPE Saudi Arabia Section Technical Symposium*. Society of Petroleum Engineers.
22. Kanj, M. Y., Rashid, M., & Giannelis, E. (2011, January). Industry First Field Trial of Reservoir Nanoagents. In *SPE Middle East Oil and Gas Show and Conference*. Society of Petroleum Engineers.
23. Käss, W., Behrens, H., & Hötzl, H. (1998). *Tracing technique in geohydrology*(p. 581). Rotterdam: Balkema.
24. Krysmann, M. J., Kelarakis, A., Dallas, P., & Giannelis, E. P. (2011). Formation mechanism of carbogenic nanoparticles with dual photoluminescence emission. *Journal of the American Chemical Society*, 134(2), 747-750.
25. Li, Y. V., Cathles, L. M., & Archer, L. A. (2014). Nanoparticle tracers in calcium carbonate porous media. *Journal of Nanoparticle Research*, 16(8), 1-14.

26. McKay, L. D., Cherry, J. A., Bales, R. C., Yahya, M. T., & Gerba, C. P. (1993). A field example of bacteriophage as tracers of fracture flow. *Environmental science & technology*, 27(6), 1075-1079.
27. Murphy, E. M., & Ginn, T. R. (2000). Modeling microbial processes in porous media. *Hydrogeology Journal*, 8(1), 142-158.
28. Petosa, A. R., Jaisi, D. P., Quevedo, I. R., Elimelech, M., & Tufenkji, N. (2010). Aggregation and deposition of engineered nanomaterials in aquatic environments: role of physicochemical interactions. *Environmental science & technology*, 44(17), 6532-6549.
29. Ray, S. C., Saha, A., Jana, N. R., & Sarkar, R. (2009). Fluorescent carbon nanoparticles: synthesis, characterization, and bioimaging application. *The Journal of Physical Chemistry C*, 113(43), 18546-18551.
30. Rayburn, J. A., K Knuepfer, P. L., & Franzi, D. A. (2005). A series of large, Late Wisconsinan meltwater floods through the Champlain and Hudson Valleys, New York State, USA. *Quaternary Science Reviews*, 24(22), 2410-2419.
31. Redman, J. A., Walker, S. L., & Elimelech, M. (2004). Bacterial adhesion and transport in porous media: Role of the secondary energy minimum. *Environmental science & technology*, 38(6), 1777-1785.

32. Remmen, K. D., (2013). *A Reactive Tracer Method for the Measurement of Specific Surface Area in EGS Reservoirs*. (Unpublished master thesis). California State University Long Beach.
33. Rodriguez Pin, E., Roberts, M., Yu, H., Huh, C., & Bryant, S. L. (2009, January). Enhanced migration of surface-treated nanoparticles in sedimentary rocks. In *SPE Annual Technical Conference and Exhibition*. Society of Petroleum Engineers.
34. Subramanian, S. K., Li, Y., & Cathles, L. M. (2013). Assessing preferential flow by simultaneously injecting nanoparticle and chemical tracers. *Water Resources Research*, 49(1), 29-42.
35. Talley, J., Baker, G. S., Becker, M. W., & Beyrle, N. (2005). Four dimensional mapping of tracer channelization in subhorizontal bedrock fractures using surface ground penetrating radar. *Geophysical research letters*, 32(4).
36. Tsolfias, G. P., & Becker, M. W. (2008). Ground-penetrating-radar response to fracture-fluid salinity: Why lower frequencies are favorable for resolving salinity changes. *Geophysics*, 73(5), J25-J30.
37. Williams, J. H., Reynolds, R. J., Franzi, D. A., Romanowicz, E. A., & Paillet, F. L. (2010). Hydrogeology of the Potsdam sandstone in northern New York. *Canadian Water Resources Journal*, 35(4), 399-416.

38. Yang, S. T., Wang, X., Wang, H., Lu, F., Luo, P. G., Cao, L., ... & Sun, Y. P. (2009). Carbon dots as nontoxic and high-performance fluorescence imaging agents. *The Journal of Physical Chemistry C*, 113(42), 18110-18114.
39. Yang, S. T., Cao, L., Luo, P. G., Lu, F., Wang, X., Wang, H., ... & Sun, Y. P. (2009). Carbon dots for optical imaging in vivo. *Journal of the American Chemical Society*, 131(32), 11308-11309.